Investigation of Soil-Structure Interaction for Low-Carbon Design of Open Caisson Shafts

Alexander W. Swallow

St Catherine's College

Department of Engineering Science



A thesis submitted for the degree of

Doctor of Philosophy

Hilary 2025

Abstract

Growing urban populations and climate change are increasing demands on water and wastewater systems worldwide, necessitating new underground infrastructure. However, constructing such infrastructure leads to significant carbon emissions. This research aims to reduce these emissions through innovations in open caisson shaft construction, a critical component of microtunnelling (MT) and other underground projects. The thesis begins with an embodied carbon (EC) analysis of three UK MT projects. The remainder of this thesis focuses on soil-structure interaction during open caisson construction, where the shaft sinks under its own self-weight. Bentonite lubrication is used to minimise soil-structure friction during sinking, after which grout is injected to replace the bentonite, and a concrete base is built. At this stage, flotation (uplift) resistance relies on soil-structure friction and the caisson's self-weight. Due to the prior use of bentonite, no methods exist to calculate friction during uplift, leading to total reliance on self-weight, resulting in material overuse and excess EC.

Laboratory testing is used to simulate caisson sinking, grout injection, and frictional uplift resistance. The results show that grout injection can produce an uneven distribution of grout due to viscous fingering (VF). To investigate this behaviour, subsequent experiments use a novel apparatus to isolate and observe the grout injection process. Finally, a numerical study in PLAXIS 2D, using adaptive remeshing, evaluates under-reaming in sands as an alternative uplift resistance strategy.

The EC analysis of MT provides insights into five areas: (1) the contribution of materials and construction phases to EC; (2) the sensitivity of EC to steel production methods; (3) the impact of on-site emissions; (4) a comparison of MT with open-cut pipeline construction; and (5) the benefits of reducing the number of shafts. Insights into the mechanisms governing frictional uplift resistance inform the derivation of a friction factor for design use in coarse-grained sands. Grout injection experiments are used to validate a predictive VF-based model to improve grout distribution on-site. The numerical study on under-reaming elucidates the influence of key factors on uplift capacity, such as anchor geometry, caisson depth, soil relative density, soil state dependence, and soil stiffness. A chart to aid design of under-reamed caissons is developed. Calculations show that the research enables substantial material and EC savings.

Acknowledgements

First and foremost, I would like to extend a thank you to my supervisor, Dr Brian Sheil. In 2018, following a friend's advice that Brian was a "sound supervisor", I volunteered to design the foundations of a bridge as part of a third-year undergraduate group design project. Little did I know this would mark the beginning of a six-year journey into the world of geotechnics and underground construction. Six years, one Master's project, and one DPhil later, I can confidently echo and extend that friend's claim. Brian has been an outstanding supervisor, offering invaluable guidance throughout my DPhil. His unwavering commitment to promptly organising meetings and providing rapid, detailed feedback on written work is unrivalled. His affable nature and infectious enthusiasm have enriched my experience immensely. I would especially like to thank him for enabling my enjoyable and rewarding year in Cambridge, which was a highlight of this journey.

I am grateful to the Department of Engineering Science at Oxford for supporting this research through the studentship funding. I would also like to express my appreciation to St Catherine's College for their generous award of the Wilfrid Knapp Scholarship. My thanks also go to the Department of Engineering in Cambridge for enabling my extended visit. Additionally, I would like to thank Professor Byron Byrne for ensuring everything ran smoothly on the Oxford end following Brian's departure. My thanks also go to Professor Barbara Rossi and Dr Vincenzo Nardelli for their valuable assessment and review of my work throughout the course of my degree.

Thanks also go to Ward and Burke Construction. Firstly, for the opportunity to work with them prior to the DPhil, which inspired and informed much of my research. Secondly, for their significant contribution in providing data for my embodied carbon work, with special thanks to Bryn Phillips for his invaluable assistance in that area. Finally, I am grateful for the input that helped guide the direction of my research, particularly from Ronan Royston and Laura Willis.

In Oxford, a special thanks goes to Daniel McNamara for his assistance in the lab, for maintaining my sanity, and his excellent company during our academic trip to Vietnam. A massive thank you is also extended to Jack Templeman for teaching me how to navigate the

relevant apparatus, for introducing me to the workings of a civil engineering laboratory more broadly, and for his collaboration on the experimental papers. I am also grateful to Clive Baker for his invaluable technical expertise in the lab and for many enjoyable chats. Thanks also go to Alison May for her helpful assistance with procurement.

In Cambridge, thank you first and foremost to Susannah Watson, whose hard work made a substantial contribution to this project. I would like to thank Neil Houghton for his design assistance, as well as Richard Boothroyd and his workshop colleagues. My appreciation also extends to Chris Burling, Harry Druiff, and all the other Civil Engineering technicians in Cambridge.

Beyond my academic work, I would like to extend my heartfelt thanks to many people for their friendship over the past few years. In Oxford, thank you to my fellow students in Civil Engineering for all the good times. Thank you to The Lunch Boys for brightening up the day to day. A special mention goes to the incredible people I met during my time at Exeter College - Sophie Davis, Thales Zanetti Ferreira, David Rytz, and Martin Wafula - thank you for all the support and memorable times spent together. In Cambridge, thank you to my housemates and partners in crime, Sophie Oldroyd and Alexandrine Royer - summer 2024 will always be one of my favourites. Outside of Oxbridge, a big shout-out to the WG, the AFG, and the Shropshire gang. All of you contributed to this DPhil being a chapter of my life I'll look back on very fondly. Finally, and most significantly, I am hugely grateful to all my family. Thank you for providing such a solid foundation and for always being there.

Contents

1 Introduction **16**

1.1 Background . . . 16

1.2 Caisson Soil-Structure Interaction . . . 18

1.3 Problem Statement . . . 19

1.4 Research Dissemination . . . 20

1.5 Thesis Structure . . . 22

2 Literature Review **24**

2.1 Introduction . . . 24

2.2 Embodied Carbon . . . 24

2.2.1 Underground Infrastructure . . . 24

2.2.2 Buried Pipeline Construction . . . 25

2.3 Caissons . . . 26

2.3.1 Construction Sequence . . . 26

2.3.2 Geotechnical Design . . . 29

2.3.3 Case Studies . . . 31

2.4 Analogous Construction Methods . . . 32

2.4.1 Alternative Shaft Construction Methods . . . 32

2.4.2 Piles . . . 32

2.4.3 Plate Anchors . . . 34

2.5 Underpinning Mechanics . . . 35

2.5.1 Bentonite Lubricants . . . 35

2.5.2 Annulus Support and Lubrication . . . 35

2.5.3 Viscous Fingering . . . 38

2.6 Summary . . . 40

3 Embodied Carbon Analysis of Microtunnelling Using Recent Case Histories 41

3.1 Introduction . . . 41

3.2 Scope of Analysis . . . 41

3.3 Methodology . . . 44
3.4 Case Study 1 . . . 49
3.5 Case Study 2 . . . 52
3.6 Case Study 3 . . . 54
3.7 Emissions Breakdown . . . 57
3.7.1 A1-A3 (Off-Site Production) . . . 57
3.7.2 A4 (Transport to Site) . . . 59
3.7.3 A5 (On-Site Activities) . . . 59
3.8 Summary . . . 60

4 Laboratory Testing of Caisson-Soil Uplift Friction in Sand 62
4.1 Introduction . . . 62
4.2 Laboratory Apparatus . . . 62
4.3 Experimental Methodology . . . 65
4.3.1 Sand Sample . . . 65
4.3.2 Lubrication and Grouting . . . 65
4.3.3 Testing Programme . . . 66
4.4 Modelling Assumptions and Scaling . . . 70
4.5 Experimental Results . . . 72
4.5.1 Frictional Resistance in Uplift . . . 72
4.5.2 Visual Observations . . . 73
4.5.3 Grout Injection Behaviour . . . 75
4.5.4 Failure Mechanism . . . 77
4.6 Limitations . . . 77
4.7 Summary . . . 78

5 Laboratory Testing on Grout Injection into Bentonite-Filled Annuli 80
5.1 Introduction . . . 80
5.2 Laboratory Apparatus . . . 80
5.3 Experimental Methodology . . . 83
5.3.1 Bentonite Slurry and Grout Preparation . . . 83

5.3.2 Rheological Testing . . . 83
5.3.3 Main Test Procedure . . . 84
5.3.4 Image Processing . . . 84
5.3.5 Testing Programme . . . 85
5.4 Modelling Assumptions: Boundary Conditions . . . 86
5.5 Rheological Test Results . . . 86
5.6 Grout Injection Test Results . . . 88
5.6.1 Grout Progression . . . 88
5.6.2 Ellipticity Results . . . 91
5.7 Summary . . . 93

6 Numerical Modelling of Under-Reamed Caissons in Sands 94
6.1 Introduction . . . 94
6.2 Problem Definition . . . 94
6.3 Finite-Element Analyses . . . 95
6.3.1 Finite-Element Model . . . 95
6.3.2 Material Models . . . 96
6.3.3 Adaptive Remeshing in PLAXIS 2D . . . 98
6.3.4 Finite-Element Calculation Stages . . . 101
6.4 Validation of Numerical Methods . . . 102
6.5 Flat Anchors (ULS) . . . 104
6.5.1 Overview . . . 104
6.5.2 ULS Results: Influence of the Associated Flow Assumption . . . 105
6.5.3 ULS Results: Influence of Soil State Dependence and Stiffness . . . 105
6.5.4 Suitability of ULS Analyses in Practice . . . 108
6.6 Inclined Anchors (SLS) . . . 110
6.6.1 Overview . . . 110
6.6.2 SLS Results: Flat Anchors . . . 110
6.6.3 SLS Results: Inclined Anchors . . . 111
6.7 Limitations . . . 114
6.8 Summary . . . 115

7 Applications and Discussion **117**

7.1 Introduction . . . 117

7.2 Grout Injection Design Model . . . 117

7.2.1 Problem Definition . . . 117

7.2.2 Model Derivation . . . 118

7.2.3 Model Validation . . . 120

7.2.4 Limitations . . . 122

7.3 Comparison of Grout Injection Results . . . 123

7.4 Implications for Grout Injection On-Site . . . 123

7.4.1 Injection Flow Rate . . . 123

7.4.2 Bentonite Slurry and Grout Mix Design . . . 124

7.4.3 Caisson Construction Details . . . 124

7.5 Caisson-Soil Uplift Friction in Sand . . . 125

7.5.1 Derivation of an Interface Friction Factor (α) . . . 125

7.5.2 Experimental Comparisons to Bored Pile Construction . . . 129

7.5.3 Application of Existing Bored Pile Research to Caisson Uplift Design . . . 132

7.6 Design of Under-Reamed Caissons in Sand . . . 133

7.7 Reducing Embodied Carbon . . . 134

7.7.1 Microtunnelling vs Open-Cut Pipeline Installation . . . 134

7.7.2 Minimising Shafts in Microtunnelling . . . 136

7.7.3 Construction Materials . . . 138

7.7.4 Caisson Material Savings . . . 141

7.8 Summary . . . 142

8 Conclusions **143**

8.1 Introduction . . . 143

8.2 Key Contributions . . . 143

8.2.1 Problem 1: Limited Literature on the EC of MT . . . 143

8.2.2 Problem 2: No Design Methods for Caisson Skin Friction Resisting Uplift 144

8.2.3 Problem 3: Uncertainty Surrounding the Grout Injection Process . . . 146

8.2.4 Problem 4: No Design Method for Under-Reamed Caissons in Sands . . . 147

8.3 Recommendations for Future Research 148
8.3.1 Embodied Carbon Analysis 148
8.3.2 Structural Design 149
8.3.3 Caisson Uplift Friction 149
8.3.4 Grout Injection 150
8.3.5 Annulus Mechanics 151
8.3.6 Under-Reamed Caissons 152
8.4 Concluding Remarks 152

A Tabulated Embodied Carbon Results **154**

Notation

AR	Adaptive remeshing
BE(A)	Best estimate (area)
Caisson	Cast in-situ open caisson shaft
CO_2e	Carbon dioxide equivalent
CS1, CS2, CS3	Case study 1, case study 2, case study 3
EC(F)	Embodied carbon (factor)
EE	Embodied energy
EP	Elasto-plastic
FEA	Finite element analysis
GGBS	Ground granulated blast-furnace slag
GIL	Grout injection location
HP	Hypoplastic
ICE	Inventory of Carbon and Energy
ID	Internal diameter
LB(A)	Lower bound (area)
LCA	Life-cycle analysis
LS1; LS2 ...	Launch shaft, case study 1; launch shaft, case study 2 ...
MT	Microtunnelling
OCI	Open-cut installation
OD	Outer diameter
PCCP	Prestressed Concrete Cylinder Pipe
PGS	Post-grouting stoppage
PSS	Post-sinking stoppage
RC	Reinforced concrete
RS1A; RS2B ...	Reception shaft A, case study 1; reception shaft B, case study 2 ...

SCMs	Secondary cementitious materials
SLS	Serviceability limit state
SSI	Soil-structure interaction
T1A; T2B ...	Tunnel A, case study 1; Tunnel B, case study 2 ...
TBM	Tunnel boring machine
TM	Trenchless method
TP(s), TP1, TP2 ...	Test piece(s), test piece 1, test piece 2 ...
ULS	Ultimate limit state
VF	Viscous fingering

A_n	Area of n^{th} element
B	Buoyant uplift force
b	Anchor width
b_a	Annulus depth
b_c	Thickness of Hele-Shaw cell
c_{inter}	Interface cohesion
c'_{ref}	Cohesion (elasto-plastic material model)
D	Anchor diameter
$D_{max,sqr,n}$	Maximum D_n within given remeshing square
D_n	Shear strain factor
D_R	Soil relative density
$\bar{D}$	Mean value of D_n over N elements.
d_i	Transportation distance associated with i^{th} material/process
d_{10}, d_{30}, d_{50}, d_{60}	Soil effective particle sizes
e_{c0}	Critical state void ratio (Hypoplastic material model)
e_{d0}	Minimum void ratio (Hypoplastic material model)
e_{i0}	Maximum void ratio (Hypoplastic material model)
e_{max}	Measured maximum void ratio

e_{min}	Measured minimum void ratio
E	Ellipticity
E'_{ref}	Young's modulus (elasto-plastic material model)
EC_i	Embodied carbon associated with the i^{th} material/process
ECF_i	Embodied carbon factor associated with the i^{th} material/process
E_{oed}	Oedometric stiffness
E_{oed}^{ref}	Oedometric stiffness measured at p_{ref}
F_c	Local coarseness factor
F_v	Uplift resistance from under-reaming
G_s	Soil particle specific gravity
h_s	Granular hardness (Hypoplastic material model)
H	Caisson overall depth
i	Iteration number
I_{d0}	Initial relative density
k	Permeability
K	Flow consistency coefficient (Sisko model)
K_0	Coefficient of lateral earth pressure
K_b	Bentonite flow consistency coefficient (Sisko model)
K_{gr}	Grout flow consistency coefficient (Sisko model)
K_s	Sinking coefficient
K_u	Uplift coefficient
l_{e0}	Target element dimension
$l_{e0,sqr}$	Local target element dimension (for given remeshing square)
L_{major}	Ellipse major axis length
L_{minor}	Ellipse minor axis length
$\dot{m}$	Mass flow rate
m_i	Mass associated with i^{th} material/process
n	Flow behaviour index (Sisko model)

n_b	Bentonite flow behaviour index (Sisko model)
n_{gr}	Grout flow behaviour index (Sisko model)
n_{HP}	Pressure sensitivity exponent (Hypoplastic material model)
N	Total number of elements in domain
N_g	Anchor dimensionless uplift factor
$N_{g,\beta=0}$	Flat anchor ($\beta = 0$) dimensionless uplift factor
p	Pressure
p'	Confining effective stress
p_b	Pressure of bentonite
p_{gr}	Pressure of grout
p_{ref}	Reference stress level
q	Volumetric flow rate per unit depth
Q	Volumetric flow rate
R	Grout profile radial coordinate
R_b	Bearing resistance during sinking
S	Stability parameter
S_μ	Stability parameter; viscosity controlled component
S_ρ	Stability parameter; density controlled component
t_b	Caisson base thickness
t_w	Caisson wall thickness
T	Overall length of test
T_s	Sinking skin friction
T_u	Uplift skin friction
U	Grout injection velocity
UD_{power}	Oedometric stiffness exponent
W	Self-weight of the caisson

α	Interface roughness factor
α_{HP}	Peak strength exponent (Hypoplastic material model)
α_w	Caisson wall interface roughness (numerical modelling input)
β	Anchor taper angle
β_{HP}	Stiffness exponent (Hypoplastic material model)
γ	Shear strain
γ_{max}	Max shear strain
$\gamma_{max,n}$	Max shear strain in n^{th} element
γ'	Soil effective unit weight
γ_d	Soil dry unit weight
$\gamma_{d,max}$	Soil maximum dry unit weight
$\gamma_{d,min}$	Soil minimum dry unit weight
$\dot{\gamma}$	Shear rate
δ	Interface friction angle
δ_c	Total upwards caisson displacement
θ	Grout profile angular coordinate
μ	Viscosity
μ_b	Bentonite viscosity
μ_{gr}	Grout viscosity
μ_∞	Viscosity at infinite shear rate (Sisko model)
$\mu_{\infty,b}$	Bentonite viscosity at infinite shear rate (Sisko model)
$\mu_{\infty,gr}$	Grout viscosity at infinite shear rate (Sisko model)
ν	Poisson's ratio
ϕ	Soil internal friction angle
ϕ_c	Soil critical state friction angle
ϕ_{inter}	Interface friction angle (numerical modelling input)
ψ	Soil dilatancy angle
ψ_{inter}	Interface dilatancy angle

ρ	Density
ρ_b	Bentonite density
ρ_{gr}	Grout density
σ_n	Normal stress
σ'_n	Effective normal stress
σ'_t	Tensile strength (elasto-plastic material model)
σ'_v	Vertical effective stress
τ	Shear stress (also referred to as skin friction)

1 Introduction

1.1 Background

Carbon emissions related to manufacturing, transportation, construction, and end-of-life phases of buildings and infrastructure account for around 11% of all global carbon emissions (WorldGBC, 2019). These emissions, commonly referred to as embodied carbon (EC), threaten to consume a large part of our remaining carbon budget. Whilst driving down EC is necessary, the need for new infrastructure is growing. For the first time, more than half the world's population was living in cities in 2017 (3.4 billion); this figure is expected to rise to 68% (6.7 billion) by 2050 (United Nations, 2018). This, combined with the effects of climate change and the need to protect the environment has placed unprecedented pressures on water and wastewater systems worldwide. New buried infrastructure offers the most, if not only, viable solution to meet these growing infrastructure demands in urban environments, whilst minimising environmental impacts (Sterling et al., 2012).

In the UK, about a fifth of potable water is wasted through leakage and current renewal rates for sewers are 0.2% per year, giving an implied service life of 500 years (NIC, 2017). In 2020, there were over 400,000 sewage discharge events into rivers, lakes and the sea. The UK government has set a target to reduce the number of annual discharges to 80,000 by 2050 (DEFRA, 2023). This will need to be achieved through a combination of three main strategies: (1) expansion of sewer networks, (2) increased capacity of water treatment facilities, and (3) increased storage to capture excess wastewater during storm events. Construction of cast in-situ open caisson shafts (henceforth referred to as caissons for brevity) and microtunnelling (MT) will be important activities for achieving these goals and key contributors to EC.

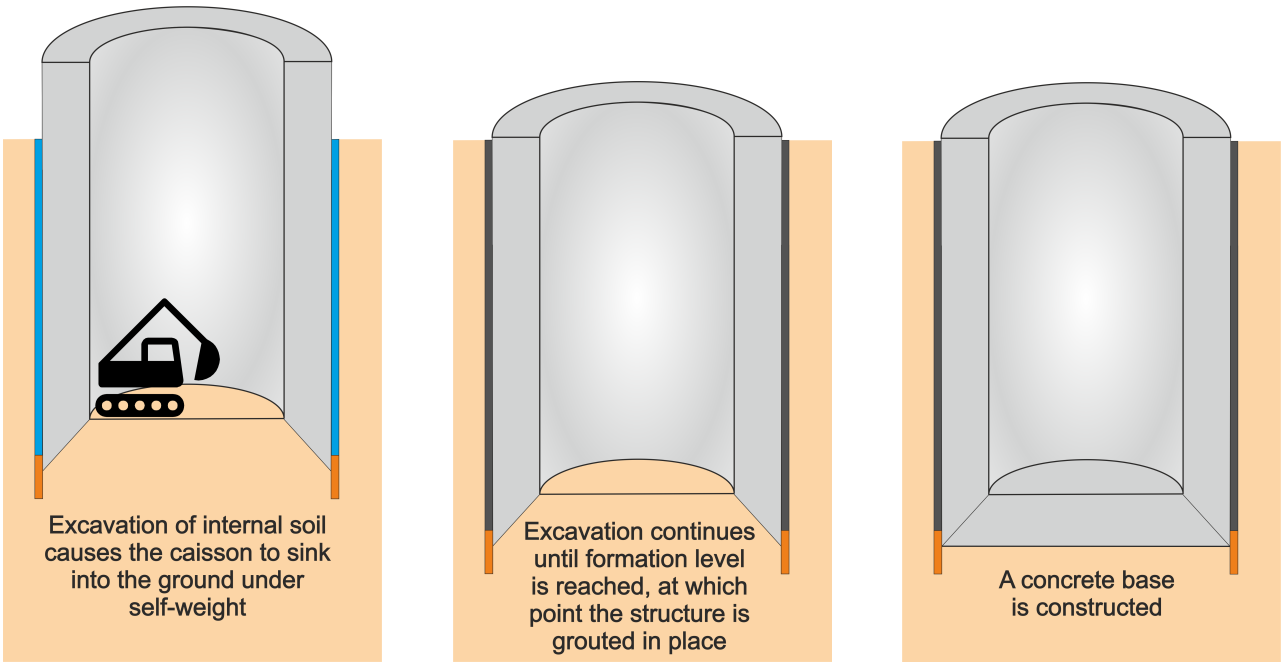
MT is an increasingly popular trenchless method (TM) of installing buried utility tunnels, offering an alternative to traditional open-cut installation (OCI). In MT, soil excavation is undertaken by a tunnel boring machine (TBM), typically commencing from within a launch shaft, and terminating in a reception shaft (Phillips, 2023). Caissons are often used to construct the launch and reception shafts for MT, as well as being commonly used for underground tanks and pumping stations. Two example caissons can be seen in Figure 1.1.



(a) (b)

Figure 1.1: Examples of open-dug in-situ caisson shafts by Ward & Burke Construction: (a) a 32m diameter caisson during construction in Blackpool, UK (Royston, 2022b); and (b) a completed 14m diameter caisson used as a microtunnelling (MT) launch shaft in Turku, Finland.

The construction procedure for caissons, summarised in the schematics in Figure 1.2, involves constructing reinforced concrete (RC) walls at ground level, before allowing the entire structure to sink under its self-weight, aided by excavation of soil from within the structure (Figure 1.2a). To achieve greater shaft depths, the height (and therefore weight) of the walls can be increased by adding new concrete pours, along with continued internal excavation. Once the desired shaft depth is achieved (formation level; Figure 1.2b), the structure is grouted in position to prevent further movement, before a concrete base is cast (Figure 1.2c).



(a) (b) (c)

Figure 1.2: Simplified schematics showing key stages of caisson construction.

1.2 Caisson Soil-Structure Interaction

The forces acting on a caisson during construction are depicted in Figure 1.3. The sinking stage of caisson construction (Figure 1.3a) relies on a balance between sinking forces and resistance arising from soil-structure interaction (SSI). The total sinking force is determined by the structure's self-weight (W) and buoyancy (B) if the caisson is constructed below the water table. To enable sinking, the downward force must exceed the upward resistance from SSI, which consists of bearing stresses at the base of the caisson (R_b) and frictional stresses (T_s) on the exterior caisson wall. Bearing stresses are reduced by using a tapered cutting face at the base of the walls, whilst frictional stresses are reduced by using a steel cutting shoe to form an annulus, which is subsequently filled with a lubricating fluid, most commonly a bentonite slurry (see Figure 1.3a).

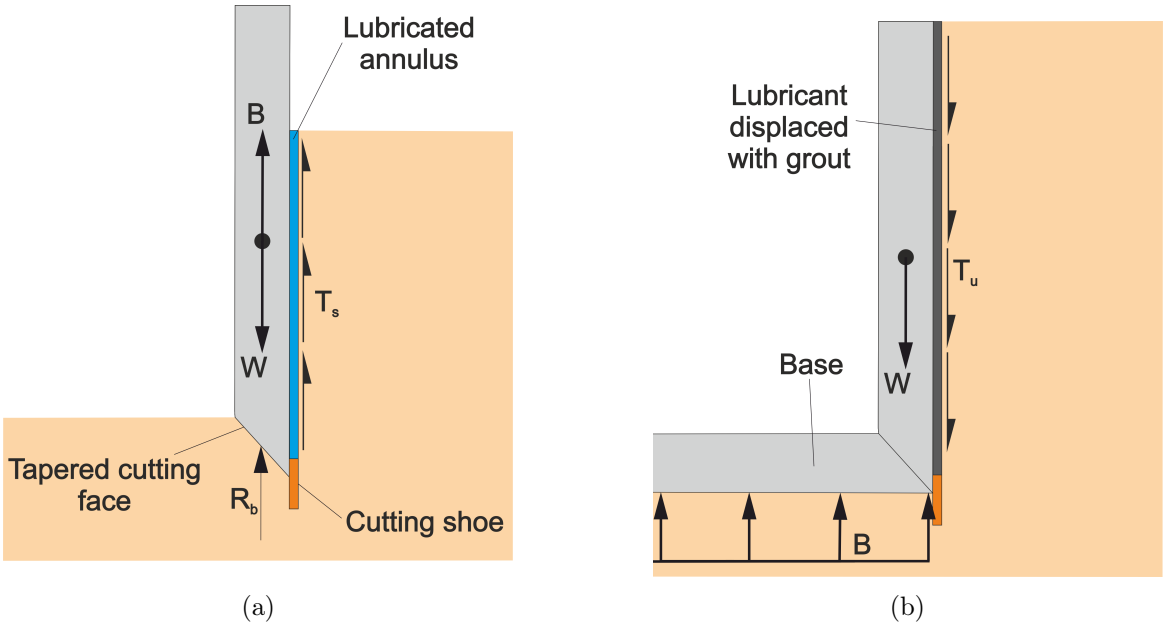


Figure 1.3: Schematic cross sections showing key construction features and the main forces acting on the caisson: (a) during sinking (W = weight of caisson, R_b = end bearing resistance, B = buoyancy, and T_s = sinking skin friction); and (b) after base construction (T_u = uplift skin friction).

Following base construction, if the shaft is constructed beneath the water table, SSI design is driven by the requirement to resist an upward buoyancy force (B; Figure 1.3b). Flotation, also referred to as uplift, can be resisted in two primary ways: (1) by the self-weight of the shaft (W), and (2) by skin friction on the exterior of the shaft walls (T_u). Recent research has focused on the sinking stage of construction, exploring both bearing resistance (Royston, 2018;

Chavda et al., 2020; Chavda & Dodagoudar, 2021; Chavda & Dodagoudar, 2022a; Chavda & Dodagoudar, 2022b; Chavda et al., 2023; Royston et al., 2022a; Sheil & Templeman, 2023; Templeman et al., 2023) and skin friction (Royston, 2018; Royston et al., 2022b; Templeman, 2022). In contrast, there is a dearth of literature considering the uplift behaviour of caissons.

1.3 Problem Statement

This thesis addresses the following shortcomings in current research:

Problem 1: Limited literature on the EC of MT

With MT and caisson construction both set to play essential roles in tackling growing demands on our utility infrastructure, the need to minimise the EC related to their construction is critical. Benchmarking the EC of current projects is a critical first step in identifying the construction activities that are the largest EC contributors and how the reduction of EC can be achieved. Despite this, the literature quantifying EC in the area is limited.

Problem 2: No design methods for caisson skin friction resisting uplift

Due to the lack of appropriate design methods, skin friction resisting uplift (T_u) is routinely assumed to be zero in practice (Allenby et al., 2009; Cui et al., 2020). Resistance is therefore provided entirely by the self-weight of the structure (W), leading to excessive material use at substantial financial and EC cost.

Problem 3: Uncertainty surrounding the grout injection process

Another key barrier preventing reliance on T_u is uncertainty surrounding the injection of grout into the annulus. On-site experience suggests a uniform spread of grout in the annulus may not always be achieved. In practice, this is undesirable as it may lead to poor engagement of friction in uplift.

Problem 4: No design method for under-reamed caissons in sands

An additional tool for resisting uplift is the use of ground anchors. One method of installation is under-reaming, as proposed by Sheil et al. (2024). Through enlargement of the caisson base, this process effectively creates a continuous ground anchor around the perimeter

of the caisson, generating additional force to resist uplift (Figure 1.4). Sheil et al. (2024) developed a closed-form design method for calculating uplift resistance on under-reamed caissons in undrained soil conditions. However, no equivalent design method exists for drained conditions.

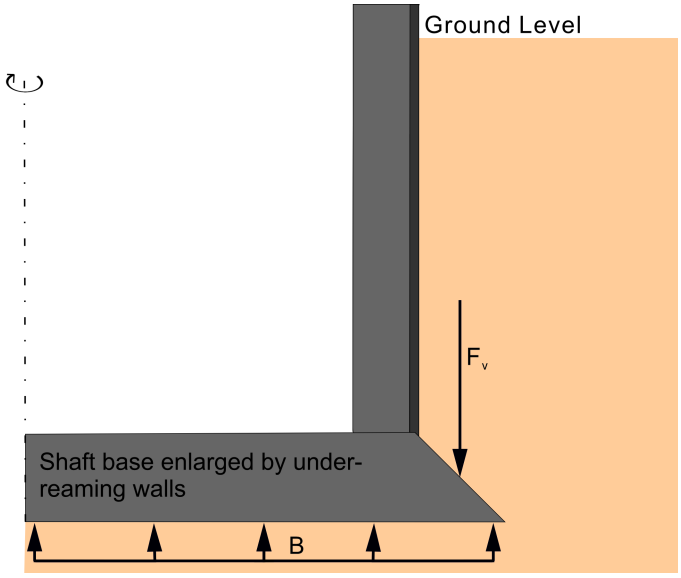


Figure 1.4: A cross section of an under-reamed caisson, demonstrating additional resistance (F_v) against uplift caused by buoyancy (B).

1.4 Research Dissemination

The research undertaken during this DPhil has contributed to five journal publications, one conference paper, and two magazine articles:

Journal Paper 1: Swallow, A. W., and Sheil, B. B. (2023). *"Embodied Carbon Analysis of Microtunneling Using Recent Case Histories."* Journal of Geotechnical and Geoenvironmental Engineering, 149(10).

Journal Paper 2: Swallow A. W., Templeman J. O., Phillips B. M., and Sheil B. B. *"Laboratory testing of open caisson skin friction in resistance to uplift in sands."* Submitted.

Journal Paper 3: Swallow A. W., Watson S. L., and Sheil B. B. *"Predicting and Ensuring Uniform Grout Injection During Open Caisson Construction."* Géotechnique Letters. Accepted.

Journal Paper 4: Swallow A. W., and Sheil B. B. (2025). *"Uplift Resistance of Under-Reamed Open Caisson Shafts in Sands."* Tunnelling and Underground Space Technology. 163.

Journal Paper 5: Templeman J. O., Swallow A. W., Phillips B. M., and Sheil B. B. *"Laboratory Testing of Open Caisson Sinking Friction in Sand."* Tunnelling and Underground Space Technology. 165.

Conference Paper: Swallow A. W., Templeman J. O., Phillips B. M., and Sheil B. B. (2024). *"Laboratory Testing of Open-Dug Caisson Skin Friction During Sinking in Sands."* In Proc. 5th International Conference on Geotechnics for Sustainable Infrastructure Development. 905-917. Hanoi, Vietnam.

Magazine Article 1: Swallow A.W., and Sheil, B.B. (November 2024). *"Embodied Carbon of Microtunnelling."* Tunnels and Tunnelling International Magazine.

Magazine Article 2: Swallow A.W., and Sheil, B.B. (publication expected late 2025). *"Cooling Prize Paper: Grout Injection in Open Caisson Shaft Construction."* Ground Engineering Magazine.

Papers 1-4 represent the majority of the work undertaken for this research and form the basis of the technical chapters in this thesis. The author carried out all the research, analysis and manuscript preparation for Papers 1, 2, and 4; the remaining authors reviewed, edited and/or supervised. The work undertaken for Paper 3 was carried out in collaboration with S.L. Watson, a fourth-year undergraduate at the University of Cambridge. The author of this thesis conceptualised and supervised the project, as well as undertaking the experiments. Analysis and manuscript preparation were also undertaken by the author.

The work for Paper 5 was conducted in collaboration with J.O. Templeman. The author of this thesis contributed to both the experimental work and the writing. As first author, Templeman included the results in his thesis (Templeman, 2022), and they are therefore not reproduced here. These findings were also presented by the author at the 5th International Conference on Geotechnics for Sustainable Infrastructure Development in Hanoi, Vietnam, where the author received a "Young Scientist Award" for submitting one of the top 20 papers presented by a researcher under 35. The author was also awarded the 56th Cooling Prize by the British Geotechnical Association for the poster and presentation entitled *"Grout Injection in Open Caisson Shaft Construction"*.

1.5 Thesis Structure

Figure 1.5 and Table 1.1 provide an overview of the project workflow and the thesis structure. Following the literature review (**Chapter 2**), ***Problem 1*** is addressed in **Chapter 3**, which presents the results from the EC analysis of three recent UK MT projects. Insights from this analysis, combined with industry input, guided the subsequent direction of the project. A critical issue identified was over-reliance on self-weight to resist uplift forces in caisson construction, presenting a significant opportunity to minimise EC. Specifically, the lack of design methods for uplift friction and for under-reamed caissons in sands emerged as a primary focus (***Problems 2 and 4***). These challenges are tackled in **Chapters 4 & 6** through laboratory testing and numerical modelling, respectively. The results of **Chapter 4** confirm industry concerns that a uniform spread of grout in the annulus may not always be achieved (***Problem***

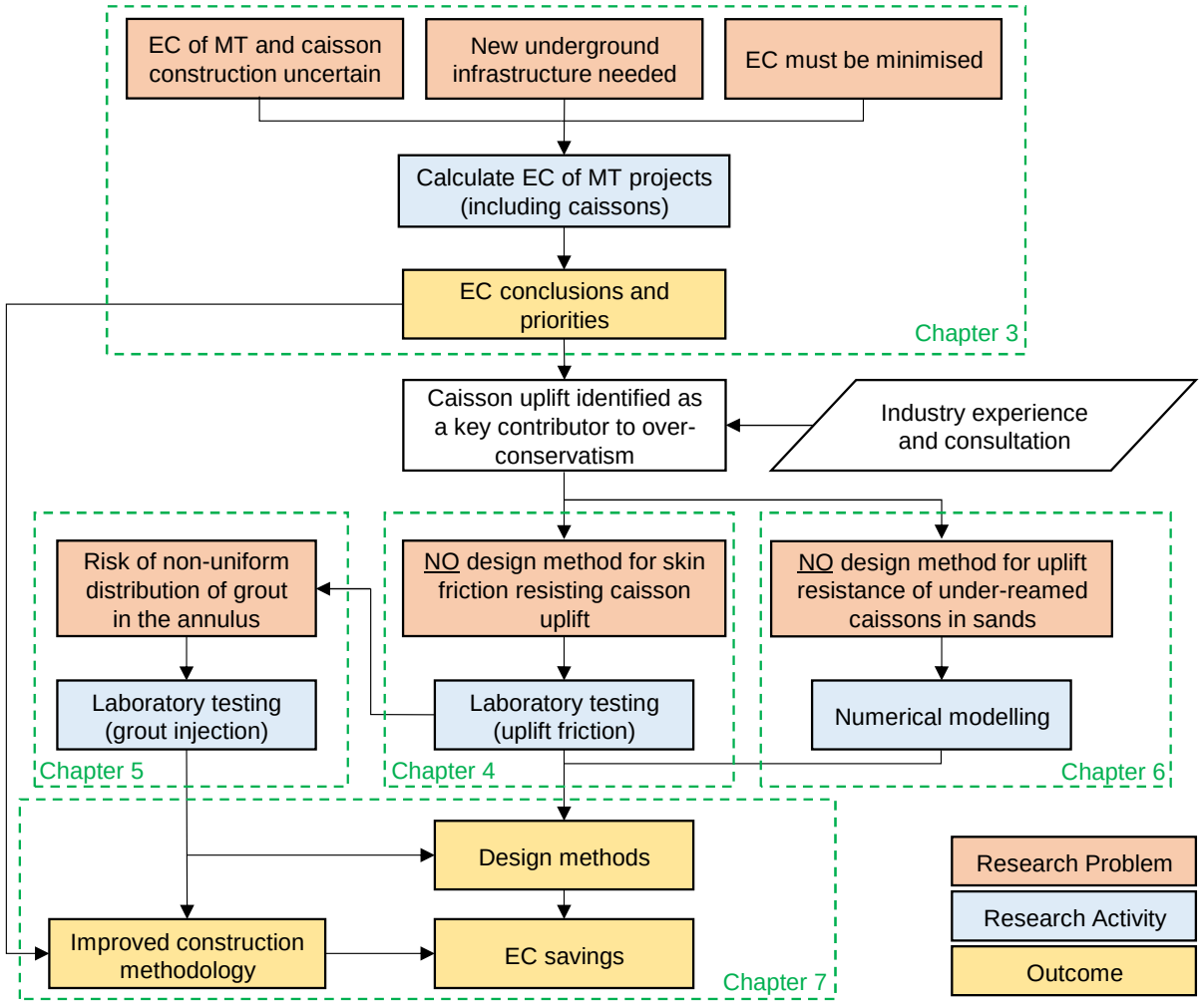


Figure 1.5: A flowchart illustrating the project's evolution, delineating the research problems addressed, the activities undertaken, and the outcomes.

3). To address this, **Chapter 5** presents additional laboratory testing designed to isolate and evaluate the grout injection process. Finally, **Chapter 7** critically discusses the application of the findings from the preceding chapters. This includes the development of design methods and recommendations for improved construction practices. A realistic design case is also considered to demonstrate the potential for substantial material and EC savings enabled by the research.

Table 1.1: Outline of the eight constituent chapters of this thesis, alongside the associated research problems and publications for each chapter.

No.	**Chapter Title**	**Research Problem**	**Associated Paper**
1	Introduction	-	-
2	Literature Review	-	-
3	Embodied Carbon Analysis of Microtunnelling Using Recent Case Histories	1	1
4	Laboratory Testing of Caisson-Soil Uplift Friction in Sand	2	2
5	Laboratory Testing on Grout Injection into Bentonite-Filled Annuli	3	3
6	Numerical Modelling of Under-Reamed Caissons in Sands	4	4
7	Applications and Discussion	1-4	1-4
8	Conclusions	-	-

2 Literature Review

2.1 Introduction

The literature review comprises four sections. Firstly, research addressing the EC of the built environment is explored, with a particular focus on underground infrastructure and buried pipelines, which are the two most relevant areas for MT. Secondly, the construction and design of caissons is explored, and a summary of published case studies is presented. Thirdly, comparisons are drawn to analogous construction methods for caissons, including alternative methods of shaft construction, piles, and plate anchors. Piles and plate anchors are considered due to their specific relevance to uplift friction and under-reamed caissons, respectively. Finally, the underpinning mechanics of key aspects of caisson construction are examined. This includes the behaviour of bentonite lubricants and an introduction to viscous fingering (VF), a phenomenon relevant to the grout injection process.

2.2 Embodied Carbon

2.2.1 Underground Infrastructure

Whilst minimising EC is crucial across all construction sectors, the literature reveals a significant focus on buildings. Akbarnezhad & Xiao (2017) identified 156 papers on this subject, providing a comprehensive review of EC estimation and minimisation for buildings. In contrast, research on infrastructure, both above and below ground, is considerably more limited (Jackson & Brander, 2019). Olugbenga et al. (2019) presented a literature review on life-cycle analysis (LCA) of rail infrastructure, highlighting that a lack of consistent system boundaries and methodology have led to difficulty in drawing comparisons and conclusions on EC in rail infrastructure. Thirteen out of the twenty-two identified studies included analysis on tunnelled sections of track (National Rail, 2009; Paris & de Silva, 2010; Chang & Kendall, 2011; Westin & Kågeson, 2012; Morita et al., 2011; Miyoshi & Givoni, 2014; Yue et al., 2015; Hanson et al., 2016; Li et al., 2018; International Union of Railways, 2016; Dimoula et al., 2016; Bueno et al., 2017; Saxe et al., 2017). None of these studies present the calculations for the tunnelled sections in detail. More recently, Huang et al. (2023) carried out a parametric exploration of

design parameters on the EC of prefabricated underground rail stations.

LCAs have also been applied to several drill and blast road tunnels (e.g. Huang et al., 2014; Xu et al., 2019; Huang et al., 2020; Rodríguez & Pérez, 2021). In all cases, materials were shown to dominate carbon emissions. For example, Rodríguez & Pérez (2021) found carbon emissions from materials, namely concrete used for shotcreting, accounted for 80% of overall carbon emissions. Studying carbon emissions of a tunnel constructed with a slurry shield TBM, Li et al. (2018) showed 93% of emissions were related to the materials.

2.2.2 Buried Pipeline Construction

Kaushal et al. (2020) conducted a comprehensive review of studies examining air pollution and greenhouse gas emissions associated with buried pipeline construction methods. Most studies focus on construction operations (i.e. neglecting emissions from manufacturing structural materials) and demonstrate that TMs generally result in fewer emissions than OCI. For example, Rehan & Knight (2007) showed that reductions in additional emissions due to traffic management can range between 78% and 100% under different trenchless schemes. Ariaratnam & Sihabuddin (2009) demonstrated that trenchless pipe replacement could reduce emissions by 80% compared to OCI, whilst Ariaratnam et al. (2013) showed that three TMs (pilot tube MT, horizontal directional drilling, and vacuum MT) reduce airborne emissions compared to OCI by 31.7%, 42.7% and 48.4%, respectively. Compared with OCI, Monfared (2018) found that auger boring and horizontal directional drilling can lead to a reduction in emissions of 86.4% and 95.6%, respectively. Kaushal & Najafi (2020) calculated that cured-in-place pipe renewal can reduce environmental effects by 68%.

A more limited number of studies have considered the EC associated with both pipe manufacturing and the construction process. These studies consistently indicate that pipe manufacturing dominates emissions related to construction. Piratla et al. (2012) considered carbon emissions from the manufacture, transportation, installation, and usage (as a pumped water supply) for four alternative pipe materials installed using horizontal directional drilling. Considering pipeline materials in the context of OCI, Khan & Tee (2015) quantified carbon emissions for steel, ductile iron and PVC pipes, whilst Chilana et al. (2016) considered steel pipes and prestressed concrete cylinder pipes (PCCP), showing manufacturing accounts for more than

90% of CO_2 emissions. Kyung et al. (2017) considered a case study of a sewage system with a range of pipe types, with careful consideration given to emissions over the entire lifetime of the sewer. Alsadi & Matthews (2020) evaluated various pipeline materials and installation methods for rehabilitating ageing sewage pipelines. Their study revealed the advantages of pipe bursting, a trenchless repair technique that involves inserting a new pipe into the existing pipe and expanding it to displace the old pipe, compared to OCI.

Studies that have focused explicitly on MT are limited. Lu et al. (2020) provided a comparison of carbon footprints relating to construction operations (i.e. neglecting pipe manufacture) of a range of TMs (including MT), and OCI. MT was shown to have the lowest carbon footprint for the installation of pipes with a diameter greater than 400 mm. Matar et al. (2019), using embodied energy (EE) instead of EC, documented the environmental impacts of a case study pipeline involving both OCI and MT. Those authors concluded that the final design, chosen for its lower cost and ease of installation, was environmentally suboptimal. EE refers to the total energy consumed to construct the pipeline. Whilst energy costs and EC are related, they are not directly equivalent, largely because of modern lower-carbon power generation (De Wolf et al., 2017). Consequently, EE is considered an outdated metric. For example, the most recent version of the Inventory of Carbon and Energy (ICE) Database (Jones and Hammond, 2019), a widely used database in the UK, no longer provides EE values, noting EC is a more useful indicator for modern analysis.

2.3 Caissons

2.3.1 Construction Sequence

Caissons can be sunk using excavators located inside the caisson (dry conditions) or by excavating soil with a clamshell bucket from ground level (wet conditions). Figure 2.1 illustrates both techniques in action during a recent project in Ireland (Willis at al., 2023). Figure 2.2 presents a schematic illustrating some common caisson construction features for dry excavation: a sheet pile wall, a guide collar, dewatering wells, and lubricant injection pipelines cast into the caisson wall. These features reflect recent practice in the UK and Ireland (e.g. Royston et al., 2022b; Willis et al., 2023). Construction methodology may vary depending on site conditions and/or contractor preference.



(a) (b)

Figure 2.1: Photographs taken during construction of a caisson by Ward & Burke Construction in Arklow, Ireland showing: (a) dry excavation; and (b) wet excavation.

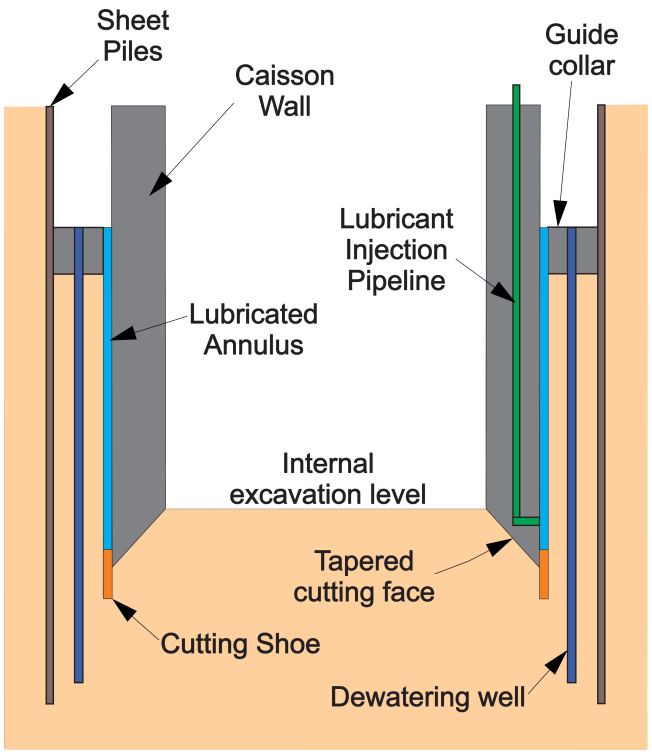


Figure 2.2: A schematic cross section of a typical caisson mid-construction showing common construction details for a caisson excavated in dry conditions.

A typical construction sequence, assuming dry excavation, is outlined below (Royston, 2018):

1. A sheet pile wall is installed around the perimeter of the final caisson location. This prevents direct loading on the caisson from on-site equipment and minimises groundwater flow into the shaft. In areas with high permeability strata overlying low permeability strata, the sheet piles should ideally be driven to penetrate the low permeability strata

to fully intercept groundwater flow. To further reduce the risk of groundwater inflow, dewatering wells are often installed around the caisson, between the caisson wall and the sheet pile wall (see Figure 2.2). This combined approach facilitates excavation in dry conditions. Installation of sheet piles has also been demonstrated to effectively reduce settlement around the caisson during sinking (Song & Sheil, 2023).

2. The sheet pile wall forms a circular cofferdam, which is excavated to a predetermined formation level, where caisson construction will begin. The lower formation depth often allows caisson construction to be commenced on stronger ground, helping maintain verticality in the early stages of construction.
3. The tapered cutting face is formed, the steel cutting shoe is placed, and the lubrication feed system is fixed (see Figure 2.3). The cutting shoe creates an 'overcut', which in turn forms the annulus. The annulus is filled with a lubricant fluid, acting to stabilise the ground and reduce friction on the walls. Lubrication ports are typically positioned at regular intervals around the caisson's perimeter, near the bottom of the annulus. Additional ports may also be installed higher up the caisson wall to deliver lubricant at various depths and provide redundancy in case of blockages (Royston, 2018).

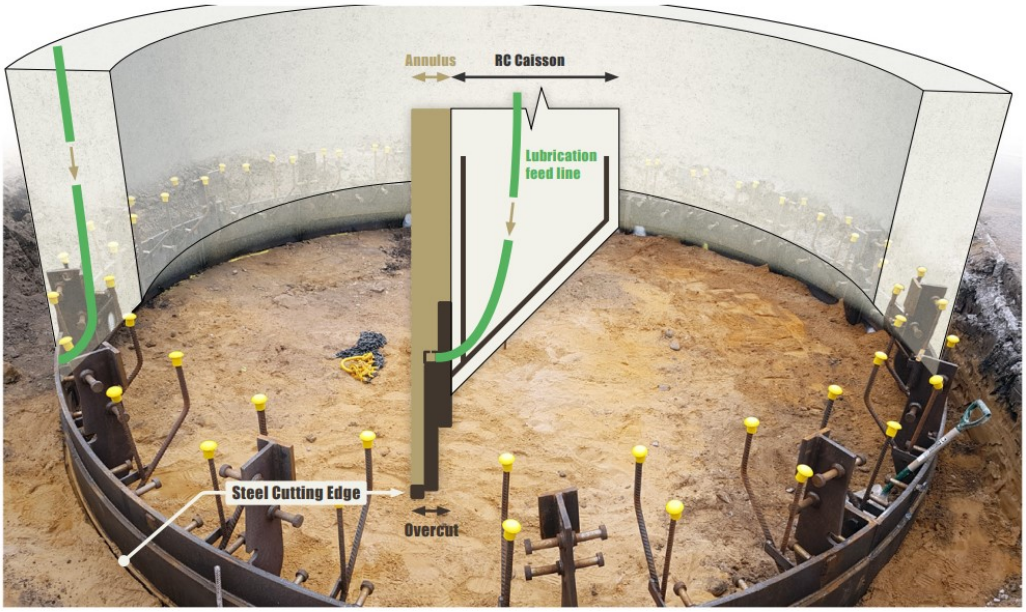


Figure 2.3: An example of a prefabricated steel cutting shoe used by Ward & Burke Construction Ltd, with schematics of the RC caisson and lubrication system superimposed.

4. Steel reinforcement is fixed, and the first wall section is cast.
5. The guide collar (see Figure 2.2), designed to assist in maintaining the verticality of the

caisson during sinking, is constructed around its perimeter, leaving a 30 to 50 mm gap. The caisson walls are then built up to a predetermined height, which may be the full final height for smaller caissons or an intermediate height for larger caissons.

6. Sinking of the caisson commences by excavating and pumping lubricant into the annulus.
7. Sinking continues, and additional wall sections are cast concurrently as necessary until formation level is reached. Once the desired depth is reached, cementitious grout is typically injected via the same pipelines to displace the lubricant in the annulus (Figure 1.3b), promoting an increase in skin friction, helping resist further movement of the caisson.
8. A RC base is constructed, completing the underground space.

2.3.2 Geotechnical Design

Caisson sinking relies on an equilibrium between the self-weight and the resistance resulting from SSI (see Figure 1.3a). This balance can be considered in terms of a sinking coefficient, K_s (Yao et al., 2014):

$$K_s = \frac{W - B}{T_s + R_b} \tag{2.1}$$

On one hand, it is undesirable for the caisson to be excessively heavy, leading to uncontrollable or excessive movements. This risk was addressed by Zhangru et al. (2021), who developed an early warning system for caisson movements, with automated alerts if sinking rates exceeded a pre-defined threshold. However, underestimating the resisting forces (T_s and R_b) is the more acute construction risk. Safiullah (2005) and Abdrabbo & Gaaver (2012) both recall case studies where caissons had insufficient mass to overcome the resisting forces, in one case resulting in a 31-month construction delay. In accordance with such high risk, Nonveiller (1987) recommends $K_s > 2$.

Considering Equation 2.1, to control the sinking process, design is initially driven by three key considerations:

1. Controlling R_b through tailored design of the tapered cutting face and cutting shoe (e.g. Royston et al., 2022a; Sheil & Templeman, 2023; Templeman et al., 2023).

2. Minimising T_s, which requires effective design of both the lubricating fluid and the delivery system.

3. Selection of an appropriate wall thickness, which controls W.

Considerable limitations remain surrounding design for caisson sinking. In particular, considerable uncertainty surrounds the minimisation of T_s during sinking, especially in sands (Royston et al., 2022b). Despite valuable recent contributions (Royston, 2018; Royston et al., 2022b; Templeman, 2022), no experimentally verified procedure to predict T_s exists, so design often relies on crude, overly conservative estimates of friction (e.g. Terzaghi & Peck, 1967; Tomlinson, 2001; Puller, 2003; Cui et al., 2020). As a result, caissons are often designed to be excessively heavy to mitigate risk.

Once sinking is complete, grout has been pumped into the annulus and the base has been cast, design is driven by the requirement to resist upwards buoyancy of the caisson (Figure 1.3b). In this case, safety can be considered in terms of an uplift coefficient:

$$K_u = \frac{W + T_u}{B} \tag{2.2}$$

where T_u represents the skin friction in uplift, which is distinct from T_s due to the introduction of grout into the annulus. In this case a value of $K_u > 1$ is required (in practice, to account for a factor of safety, a minimum value greater than $K_u = 1$ may be preferred). Similar to the sinking phase, there are no established design methods to quantify T_u, meaning it is routinely neglected in anti-flotation calculations (Allenby et al., 2009; Cui et al., 2020), resulting in over-reliance on W. In the author's experience, the combined weight of the walls and the minimum base thickness required for structural integrity is often insufficient to resist uplift on its own. This frequently necessitates extra base thickness to increase W, resulting in excessive material use at substantial financial and environmental cost.

Another option for resisting uplift involves under-reaming the walls of the shaft post-sinking to create an enlarged base (Figure 1.4). However, industry uptake of this approach is limited at present. Recently, Sheil et al. (2024) introduced a design method for under-reamed caissons in undrained soil. In contrast, there are no studies considering drained conditions. Uplift can also be resisted by reacting off adjoining structures such as tunnels. However, the potential

resistance is typically limited, and concerns about damaging these structures often restrict the use of this approach (Sheil et al., 2024).

2.3.3 Case Studies

Table 2.1 summarises documented case studies, highlighting the wide range of diameters and depths achievable through caisson construction. The studies primarily focus on the sinking stage, with limited attention to subsequent grout injection and base construction.

Table 2.1: Open caisson case studies documented in the literature.

Reference	ID **(m)**	H **(m)**	t_w **(m)**	t_b **(m)**	**Lubrication**	**Ground Conditions**
Ter-Galustov et al. (1966)	15.4	14.1	0.3	-	Clay-based mud	Dense loams
Chandler et al. (1984)	9.8-10.4	91-103	1.8-2.4	-	Bentonite slurry	Silty sands and gravels
Nonveiller (1987)	27	60	1.5	-	Bentonite slurry	Stiff over-consolidated clay
Fischer et al. (2004)	18.3	22.9	0.9	1.8	Bentonite slurry	Stiff silty clay overlying soft clay
Abdrabbo & Gaaver (2012)	20	33.3	1.6	9	-	Weak limestone overlying dense sand overlying sandy silt/silty clay
Khasawneh et al. (2017)	41.5	38.1	2.3	-	Bentonite slurry	Clay overlying silt overlying sand
Royston (2018)	11	20	1	-	Polymer fluid	Soft clay overlying mudstone
Royston (2018)	25	15	1	-	Bentonite and polymer mix	Soft peat overlying medium density sand
Royston et al. (2022b)	32	20	1.25	1.5	Bentonite and polymer mix	Dense sand overlying stiff clay
Willis et al. (2023)	19	19	1.6	-	Bentonite slurry	Marine sand overlying gravel and clay

ID = internal diameter, H = overall depth, t_w = wall thickness, t_b = base thickness. Parameters either stated in the reference or inferred from figures. '-' indicates where information was not available.

Only three of the studies in Table 2.1 detail base thicknesses. One of these employed a 9 m base thickness (Abdrabbo & Gaaver, 2012). It is likely this was designed to provide sufficient weight to resist uplift, demonstrating the potential for excessive material use due to current design practices.

2.4 Analogous Construction Methods

2.4.1 Alternative Shaft Construction Methods

Beyond caissons, segmental shaft construction, where pre-cast segments are bolted together, is another common method for creating vertical underground spaces (e.g. New & Bowers, 1994; McNamara et al., 2008; Allenby et al., 2009; Newman & Wong, 2011; Faustin et al., 2018; Lai et al., 2022). Segmental shafts can be constructed in two ways: (i) through underpinning, where segments are inserted beneath an existing structure as excavation progresses (e.g. Faustin et al., 2018; Figure 2.4a); or (ii) through jacked sinking, where new segments are attached at the top of the shaft wall whilst the structure is forced into the ground using hydraulic rams (e.g. Newman & Wong, 2011; Figure 2.4b). Jacked sinking shares significant similarities with caisson construction, including the use of lubricating fluids and grout injection into the annulus at the end of sinking (Allenby et al., 2009). Other common shaft construction methods include bored secant piles (e.g. Lindquist & Jameson, 2011; Figure 2.4c) and diaphragm walls (e.g. D'Alessio & Taylor, 2016; Figure 2.4d). Similarities between these methods and caissons allow for comparisons to caisson uplift behaviour, which is discussed in Section 2.4.2.

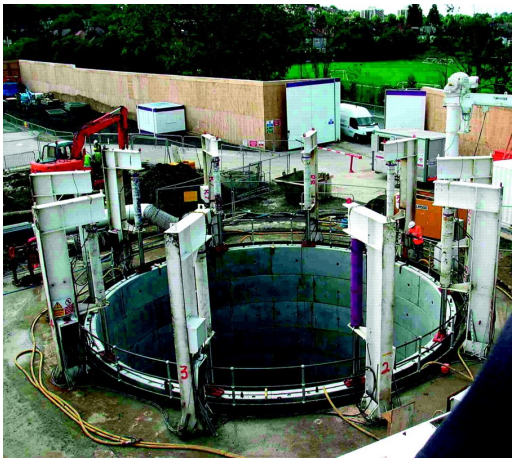
2.4.2 Piles

Research and design methods for displacement piles can offer insights into caisson interface SSI. Friction during caisson sinking can be compared to friction during displacement pile installation (e.g. White & Lehane, 2004), whilst caisson uplift resistance is somewhat analogous to displacement piles under tension loading (e.g. Lehane et al., 2020). However, significant differences limit the applicability of these methods to caissons. Notably, caissons are typically an order of magnitude larger in diameter than displacement piles, and the use of a lubricated annulus fundamentally distinguishes the construction processes.

Closer comparisons can be drawn to bored pile and diaphragm wall construction, during



(a)



(b)



(c)



(d)

Figure 2.4: Photographs taken during shaft construction using different methodologies: (a) segmental underpinning (Faustin et al., 2018); (b) segmental jacked sinking (Newman & Wong, 2011); (c) secant piles (Lindquist & Jameson, 2011); (d) diaphragm walls (D'Alessio & Taylor, 2016).

which bentonite slurry is commonly used as a support fluid to stabilise the surrounding soil during excavation. Upon completion of excavation, reinforcing steel is placed, and concrete is poured using the tremie method. Geotechnical design subsequently relies on the mobilisation of friction at the concrete-soil interface, which has previously been exposed to the support fluid. This interaction is analogous to skin friction at the grout-soil interface following caisson construction. Studies such as Lam et al. (2014) and Verst et al. (2022) have improved understanding of friction on bored piles following soil exposure to support fluids; however, the applicability of these results to caisson uplift remains highly uncertain.

Bored piles can also be under-reamed to increase tensile capacity (e.g. Harris & Madabhushi, 2015; Rahman & Sengupta, 2017; Kumar et al., 2021). Whilst comparisons can be drawn

to under-reamed caissons (Figure 1.4), the significantly larger diameter of caissons results in different uplift capacities.

2.4.3 Plate Anchors

Under-reaming caissons to resist uplift is analogous to using annular plate anchors. Extensive research has been conducted on embedded plate anchors in both clays (e.g. Merifield et al., 2001; Merifield et al., 2003; Merifield et al., 2005; Song et al., 2008; Wang et al., 2010) and sands (e.g. Merifield & Sloan, 2006; Merifield et al., 2006; Giampa et al., 2019; Roy et al., 2021; Roy et al., 2022). Key differences between under-reamed caissons and plate anchors are illustrated in Figure 2.5. Whilst plate anchor research has primarily focused on offshore applications with loading perpendicular to the plane of the plate, under-reamed caissons experience vertical loading regardless of the orientation of the under-ream element. SSI with the caisson wall further differentiates design, limiting the applicability of existing plate anchor design methods to under-reamed caissons.

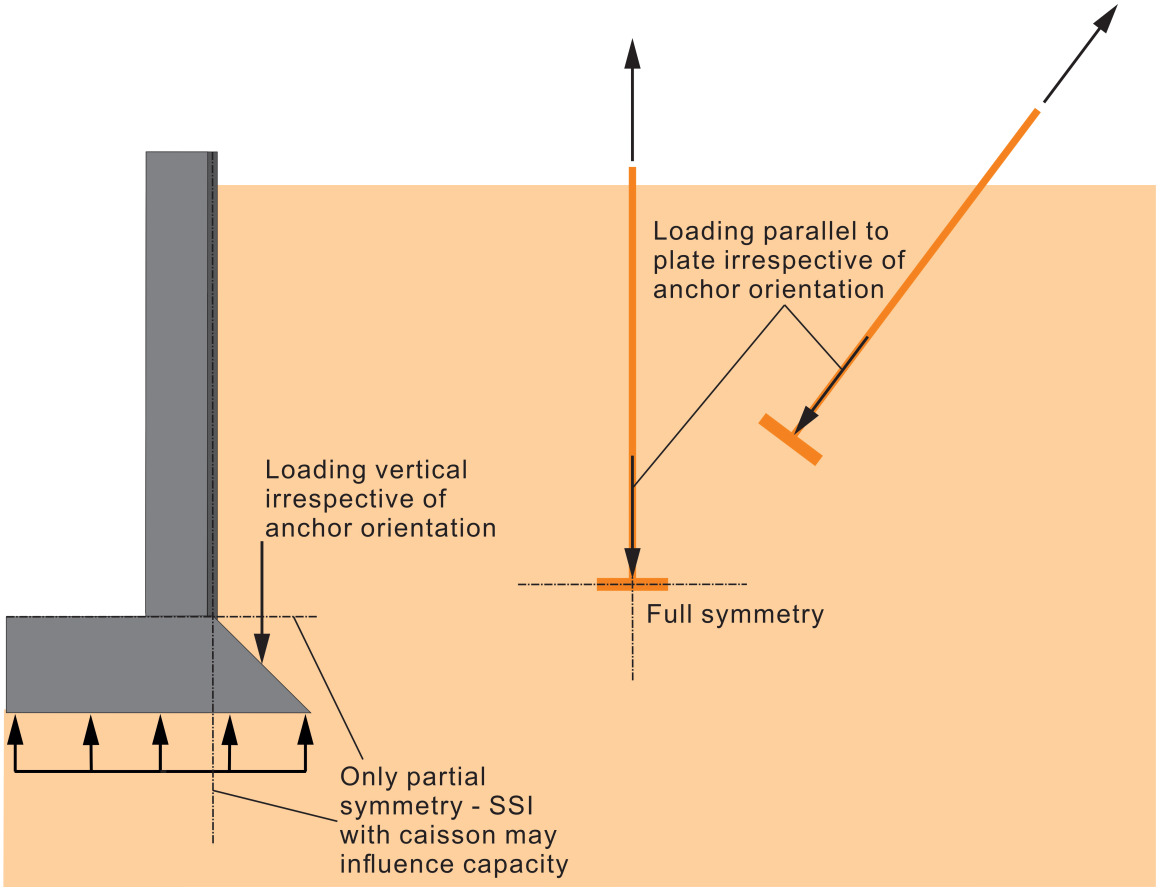


Figure 2.5: A schematic comparison of an under-reamed caisson and plate anchors, demonstrating key differences which influence uplift capacity.

2.5 Underpinning Mechanics

2.5.1 Bentonite Lubricants

Bentonite is a montmorillonite-based clay composed of plate-like mineral sheets. Bentonite slurries comprise a mixture of dry bentonite and water, mixed thoroughly at a high shear rate until the clay particles are completely dispersed. The mixture is then left to stand until the clay is hydrated in the solution (Milligan, 2000). Bentonite slurries are highly non-Newtonian fluids, exhibiting shear-thinning behaviour (Li et al., 2016). A wide range of rheological models are available for modelling the behaviour of bentonite. Li et al. (2016) considered eight of these models and concluded that the Sisko model most accurately captured the behaviour of bentonite. The Sisko model is defined by:

$$\tau = \mu_\infty \dot{\gamma} + K\dot{\gamma}^n \tag{2.3}$$

where τ is shear stress, $\dot{\gamma}$ is the shear rate, μ_∞ is the viscosity at an infinite shear rate, K is the flow consistency coefficient and n is the flow behaviour index (Sisko, 1958). The curve-fitting parameters (μ_∞, K, and n) can be determined using appropriate rheological testing.

Bentonite slurries are thixotropic, transitioning from a high-viscosity gel state at rest to a more fluid state with lower viscosity when agitated or sheared. When left to rest again, bentonite reassumes its gel-like properties. Thixotropic behaviour can be demonstrated through cyclic rheological testing. Ren et al. (2021) conducted such testing on bentonite, effectively illustrating thixotropy with a high initial shear stress for the first loop of cyclic shear loading, which was absent in subsequent loops (Figure 2.6). This high initial shear stress is referred to as the yield stress. Rheological models, including the Sisko model (Equation 2.3), typically neglect time-dependent effects such as thixotropy (Phillips, 2023).

2.5.2 Annulus Support and Lubrication

Bentonite lubricants reduce friction by exerting hydrostatic pressure on the surrounding soil, maintaining an annular gap between the structure and soil (Figure 2.7), similar to lubrication in pipe-jacked tunnelling (Templeman, 2022). Thus, interface shearing is designed to occur at the structure-bentonite interface, not a structure-soil interface, leading to substantially lower

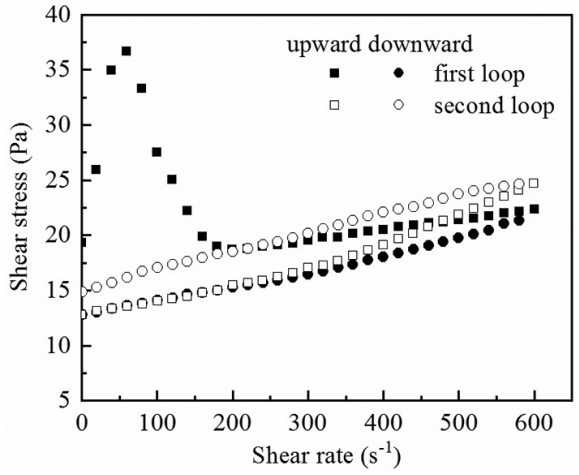


Figure 2.6: Cyclic loading of bentonite slurry, demonstrating an initial increase in shear stress due to thixotropy (Ren et al., 2021).

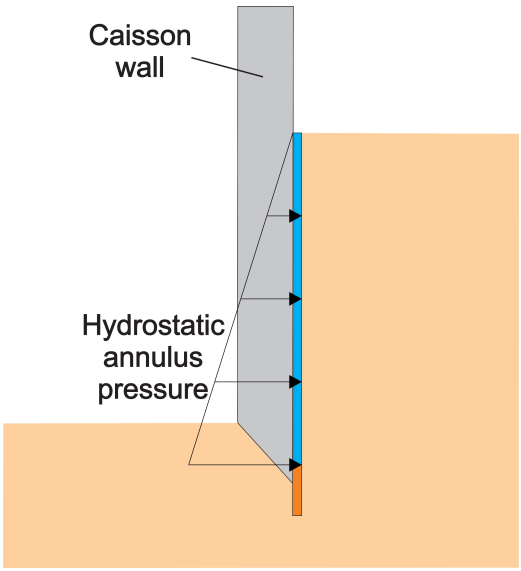


Figure 2.7: A schematic cross section of a caisson demonstrating hydrostatic pressure exerted on the surrounding soil by bentonite slurry in the annulus.

resistance. Maintaining the annular gap depends on restricting the loss of support fluid into the surrounding soil. This is achieved through the formation of a low permeability filter cake, which can occur in three modes: (a) in the annulus at the soil boundary (external filter cake); (b) within the soil structure (internal filter cake); or (c) a combination of external and internal (Min et al., 2013; Figure 2.8). The prevailing mode is primarily driven by the permeability, and hence the particle size distribution, of the soil (Min et al., 2013; Xu & Bezuijen, 2019). Praetorius & Schößer (2017) predict filter cake formation based on the soil's 10% particle size fraction (d_{10}). Those authors state mode (a) is expected for soils with a $d_{10} < 1$ mm, whereas mode (b) is anticipated for larger particles. Mode (c) is therefore likely to occur as a transitional behaviour around $d_{10} \approx 1$ mm. Soils with a d_{10} greater than 6 mm are unlikely to form any

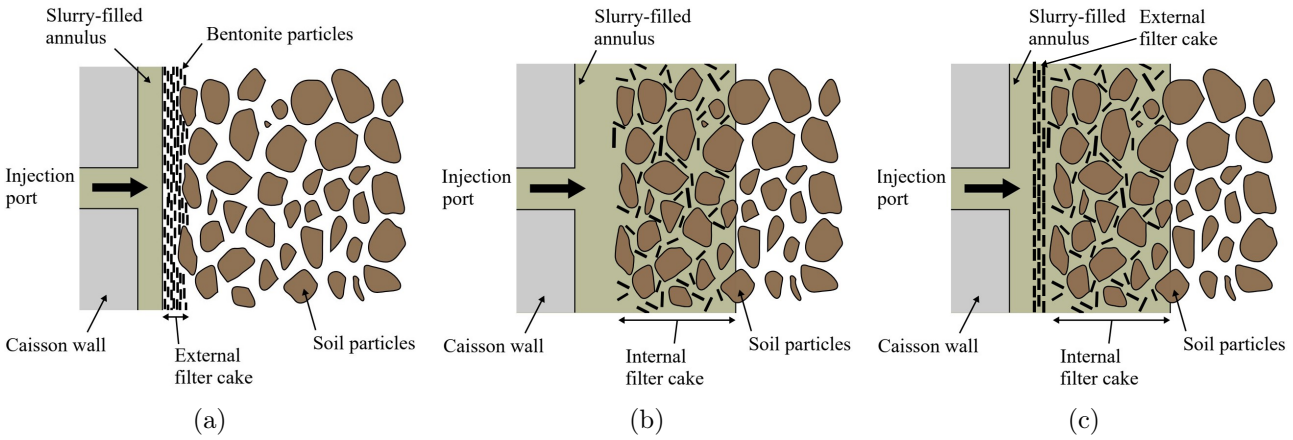


Figure 2.8: Modes of bentonite filter cake formation, adapted from Templeman (2022): (a) external filter cake; (b) internal filter cake; and (c) combined filter cake (internal and external).

filter cake (Praetorius & Schößer, 2017).

Bentonite slurry in the annulus loses water to the surrounding soil with time, increasing the viscosity of the bentonite. This can occur due to consolidation of the bentonite or filtration of water into the surrounding soil with minimal excess pore pressure dissipation (Phillips, 2023). Given the typical 2-3 month timeframe for caisson sinking (e.g. Royston, 2018; Royston et al., 2022b; Willis et al., 2023), there is ample opportunity for consolidation and/or filtration to occur. Whilst studies have been carried out to measure the water loss under such conditions (e.g. Min et al., 2013; Phillips, 2023), there are no established methods for predicting bentonite viscosity as a function of time in the annulus.

Polymer-based support fluids are an increasingly popular alternative to bentonite. Unlike bentonite, polymer fluids do not form a filter cake. Instead, the long chain-like polymer molecules exert frictional drag on the soil particles so that seepage is limited by the viscosity of the fluid, allowing a high pressure gradient to be maintained (McNamara et al., 2024). Polymer fluids have been shown to be effective at stabilising bored pile excavations in granular soils (e.g. Lam & Jefferis, 2016), however, examples of their use for lubrication are limited (see Table 2.1). Use of polymers is an ongoing area of research and further investigation of polymer support fluids is required to increase uptake in industry (Lam & Jefferis, 2017). Polymer additives may also be incorporated into bentonite slurries to tailor properties such as viscosity and reduce fluid loss to the surrounding soil (Praetorius & Schößer, 2017; Templeman, 2022).

2.5.3 Viscous Fingering

Currently, there is concern in industry that the lubricant in the annulus may not be uniformly displaced during grout injection, which may result in insufficient grout coverage to develop reliable friction. A possible cause of non-uniform displacement is Saffman-Taylor instability, also known as VF, which results from the injection of a less viscous fluid into a more viscous fluid. Under these circumstances, the displacement front between the two fluids is unstable and can lead to the less viscous fluid forming finger-like or branched patterns within the more viscous fluid (see Figure 2.9). In contrast, when a more viscous fluid is injected into a less viscous fluid the displacement is stable and uniform (Saffman & Taylor, 1958).

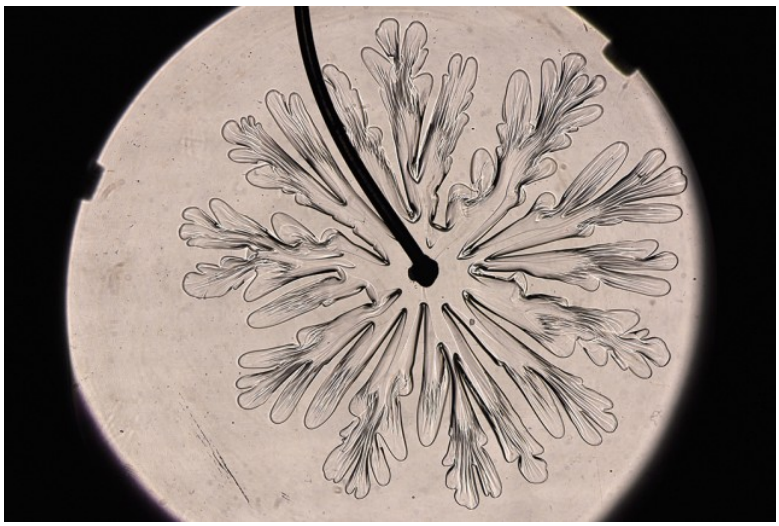


Figure 2.9: *Schlieren Imaging of Viscous Fingering and Buoyancy Driven Convection* by Simone Stewart. Entrant to the Art of Science Competition 2017[1]. The image presents an example of VF, showing the resulting pattern following the injection of a less viscous fluid (water) into a more viscous fluid (glycerol).

Hill (1952) was the first to identify the phenomenon of VF, studying the flow of water into sugar solutions during sugar production. This work was followed by the seminal papers of Saffman & Taylor (1958) and Chuoke et al. (1959), which presented controlled experiments and derived the underpinning theoretical mathematics of VF. Since then, the field has been extensively studied, both theoretically and experimentally, resulting in numerous critical reviews (e.g. Saffman, 1986; Bensimon et al., 1986; Homsy, 1987; Tanveer, 2000; Pinilla et al., 2021).

The majority of experimental work on VF has been conducted using a Hele-Shaw cell, which consists of two parallel glass sheets creating a thin void for fluid containment. VF

[1](https://art-csep.cnsi.ucsb.edu/gallery/schlieren-imaging-viscous-fingering-and-buoyancy-driven-convection)

can be simulated by filling the void with a more viscous fluid before injecting a less viscous fluid through an opening in one of the glass sheets (see Figure 2.10). One-dimensional flow in direction x, assuming gravity is collinear with the displacement direction, in a Hele-Shaw cell is governed by the following equation (Homsy, 1987):

$$\frac{dp}{dx} = -\frac{12\mu U}{b_c^2} + \rho g \tag{2.4}$$

where p = pressure, μ = viscosity, U = injection velocity, b_c = thickness of cell, and ρ = density. Flow in porous media is governed by Darcy's law (Darcy, 1856), which in isotropic porous media may be written:

$$\frac{dp}{dx} = -\frac{\mu U}{k} + \rho g \tag{2.5}$$

where k = permeability. Comparing Equations 2.4 and 2.5, the flow in a Hele-Shaw cell therefore satisfies Darcy's law with an equivalent permeability of $k = {b_c}^2/12$. This equivalence enables the study of VF in a Hele-Shaw cell to be directly applied to VF in porous media, which is the primary focus of most practical applications in the literature. In particular, the extraction of oil and gas is the most extensively studied area within this context (Pinilla et al., 2021). Other modern applications include the operation of fuel cells (e.g. Lee et al., 2019; Mortazavi et al., 2020), and subsurface carbon dioxide sequestration (e.g. Pau et al., 2010; Wang et al., 2013). Whilst extensively studied by applied mathematicians, physicists, and geologists alike, VF applications within construction remain limited, and no studies have explored the influence of VF on grout injection into a bentonite-filled annulus.

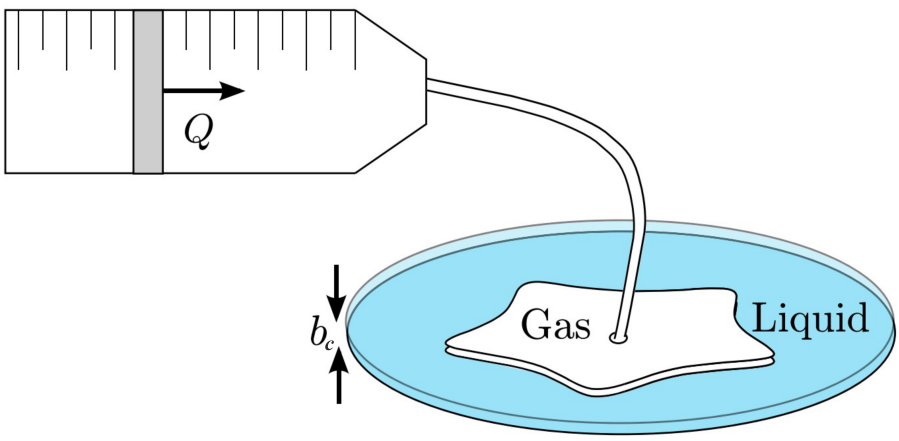


Figure 2.10: A schematic diagram by Cuttle et al. (2023) of a Hele-Shaw cell, consisting of two parallel plates with a uniform gap, b_c. The configuration enables a gas to be injected at a constant volumetric rate Q into a liquid, simulating VF.

2.6 Summary

The literature on EC largely focuses on buildings, with underground infrastructure receiving less attention. Within this domain, there is considerable research on road and rail tunnels, as well as various pipeline construction methods. However, studies specifically addressing microtunnelling and caisson construction are extremely limited. In the few cases where these construction processes are considered, key contributors to emissions, such as materials, are often overlooked, or outdated metrics, such as EE, are used.

Considering caissons, shortcomings in the literature often lead to excessive structural weight due to design considerations in both sinking and uplift. The weight of the caisson walls is primarily driven by sinking requirements. As a result, to resist uplift, weight is typically increased by constructing a thicker base. Relying on friction for uplift resistance offers the potential to reduce base thickness, thereby conserving materials and lowering EC. Whilst under-reaming provides an alternative means of uplift resistance, its application remains limited due to a lack of research, particularly in drained soil conditions. Overall, most existing research on caissons focuses on the sinking process, whilst uplift behaviour remains significantly understudied.

Although parallels exist between caissons and other construction methods such as segmental shafts, bored piles, and diaphragm walls, the direct applicability of literature on these methods to caissons is uncertain. Similarly, whilst plate anchor research provides insights into under-reaming, significant differences in geometry restrict its applicability to caisson design.

During sinking, bentonite lubricants play a critical role by reducing friction and maintaining an annular gap between the caisson and surrounding soil. This gap is stabilised through the formation of a filter cake that prevents fluid loss. Following sinking, cementitious grout is injected into the bentonite-filled annulus to re-establish friction with the surrounding soil. However, significant uncertainty exists regarding both the grout injection process and the extent to which friction is effectively re-engaged.

A key concern during grout injection is the potential for VF, which occurs when a less viscous fluid is injected into a more viscous fluid, leading to non-uniform spread of grout. Despite VF being extensively studied in other fields, its impact on caisson construction remains unexplored. The gaps in knowledge identified in this literature review informed the research problems outlined in Section 1.3, which provide the motivation for this study.

3 Embodied Carbon Analysis of Microtunnelling Using Recent Case Histories

3.1 Introduction

A critical review of the literature on the EC of buried pipelines was presented in Section 2.2.2, revealing previous research on TMs has largely overlooked the influence of pipe manufacture, a key contributor to EC. Studies that do consider pipe manufacture have focused on OCI and/or employed EE, which is now considered an outdated metric. To the author's knowledge, the literature contains no examples of an EC analysis of MT from material manufacture through to tunnel completion and including temporary works (shafts).

This chapter addresses these shortfalls and enhances understanding of carbon emissions related to MT by: (a) providing a methodology and well-defined system boundaries for calculating the EC of MT projects from material manufacture through to practical completion; (b) clearly presenting the EC of distinct project elements (i.e. tunnels and shafts); (c) developing a bespoke database of MT projects using three recent UK case histories as exemplars; and (d) identifying the most carbon-intensive construction processes and stages. This research was carried out using data provided by Ward & Burke Construction Ltd.

3.2 Scope of Analysis

The system boundary for the present study is considered in terms of modules A-D set out in BS EN 15798:2011 (BSI, 2011; see Figure 3.1). Buried utilities constructed using MT are highly unlikely to be deconstructed at end of life due to accessibility issues. Hence, the influence of modules C and D (end of life and beyond) is relatively insignificant and therefore not considered here. The final applications of microtunnels can be varied, with uses including gravity sewers, hydrostatically pressurised pipelines, pumped pressurised pipelines, or carriers for other utilities. As such, the EC for module B can vary significantly from project to project.

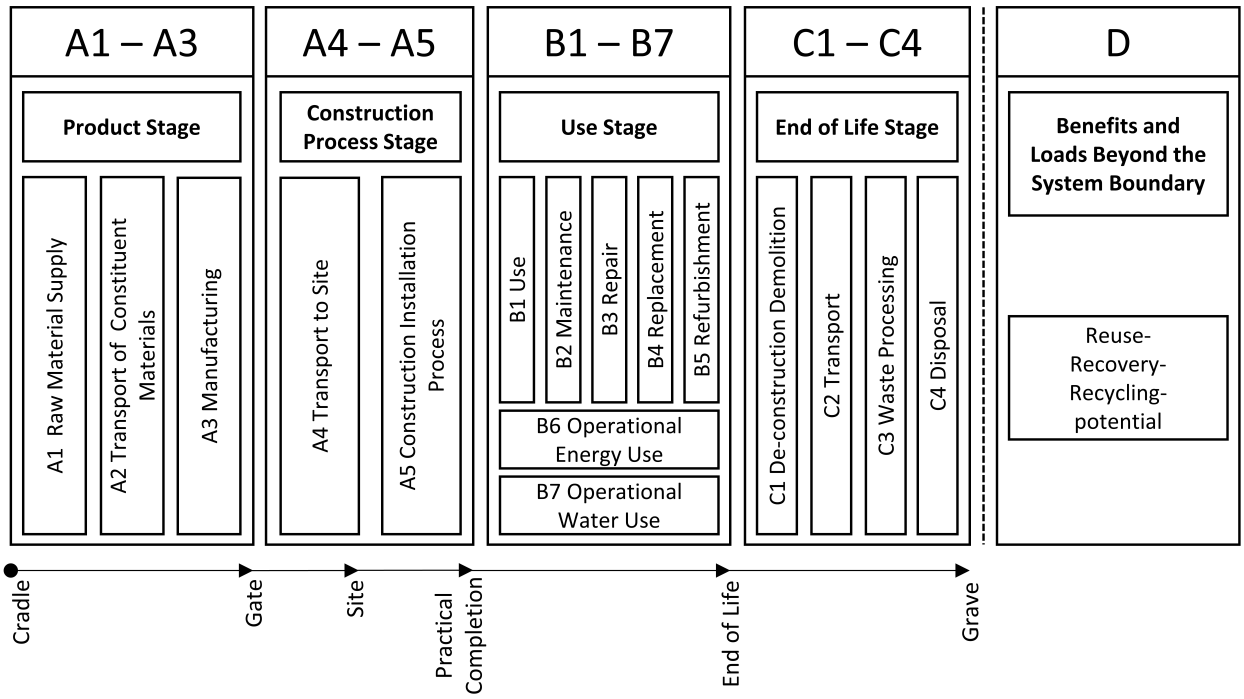


Figure 3.1: Life cycle modules (adapted from BSI, 2011).

To mitigate these differences and provide a fair basis for comparison, the scope of this study excludes module B.

The activities considered are restricted to those involved in the core high-carbon processes of MT, namely the construction of the launch shaft, the reception shaft and the tunnel itself (see Figure 3.2). There are significant variations between projects in application-dependent additional works, including installation of utilities, connections to existing services, construction of connecting/access structures and manholes, backfilling, and reinstatement of land. Restricting analysis to these core processes further enables fair comparison of projects.

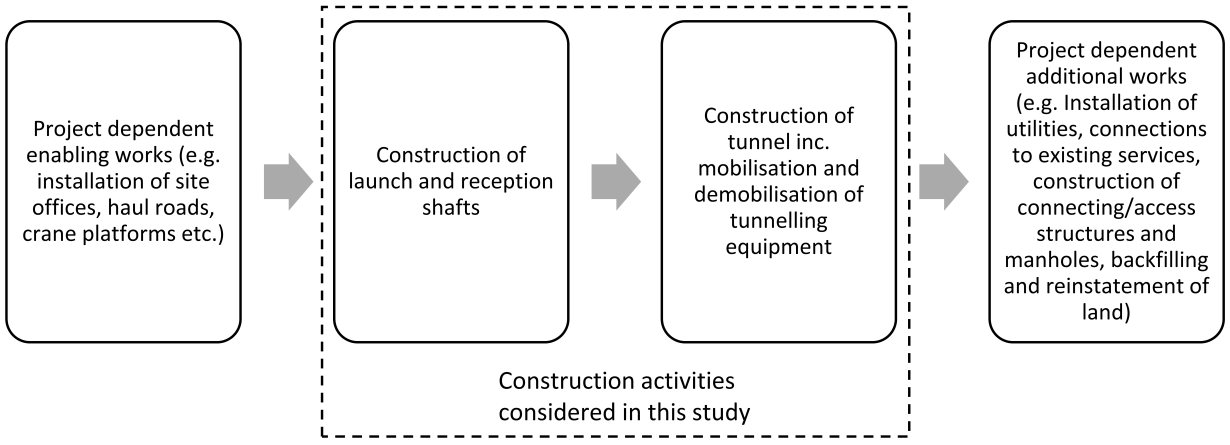


Figure 3.2: A typical timeline of a MT project including the scope of activities considered in this study.

The three case studies considered in this chapter involve precast RC pipes and open caissons for the launch and reception of the TBM. Therefore, the materials and processes considered in this study are tailored to suit these methods of construction. As presented in Figure 3.3, three primary construction materials are considered in modules A1-A3: (1) concrete, which can be broken down into its constituents based on the mix design; (2) reinforcing steel; and (3) components fabricated from steel plate, such as the 'tailskin' on jacking pipes and the 'cutting shoe' on caisson shafts. The tailskin is located at the rear of a jacking pipe and is used to guide and seal the trailing pipe (Phillips, 2023). The cutting shoe aids caisson sinking as described in Section 2.3.1. Three manufacturing facilities are required for the supply of materials and components: the concrete batching plant for the cast in-situ shafts, the precast factory for the pipes, and the fabrication yard for the cutting shoe. Consequently, three further sources of emissions are considered within A1-A3 in Figure 3.3: (a) delivery of constituent materials to the manufacturing facilities; (b) operations of the manufacturing facilities; and (c) waste resulting from the processes at the manufacturing facilities. Three contributors to emissions are considered in A4-A5: (i) delivery of all materials to site; (ii) emissions due to operation of machinery on-site; (iii) material waste on-site, including transport of waste away from the site and the processing of waste at disposal.

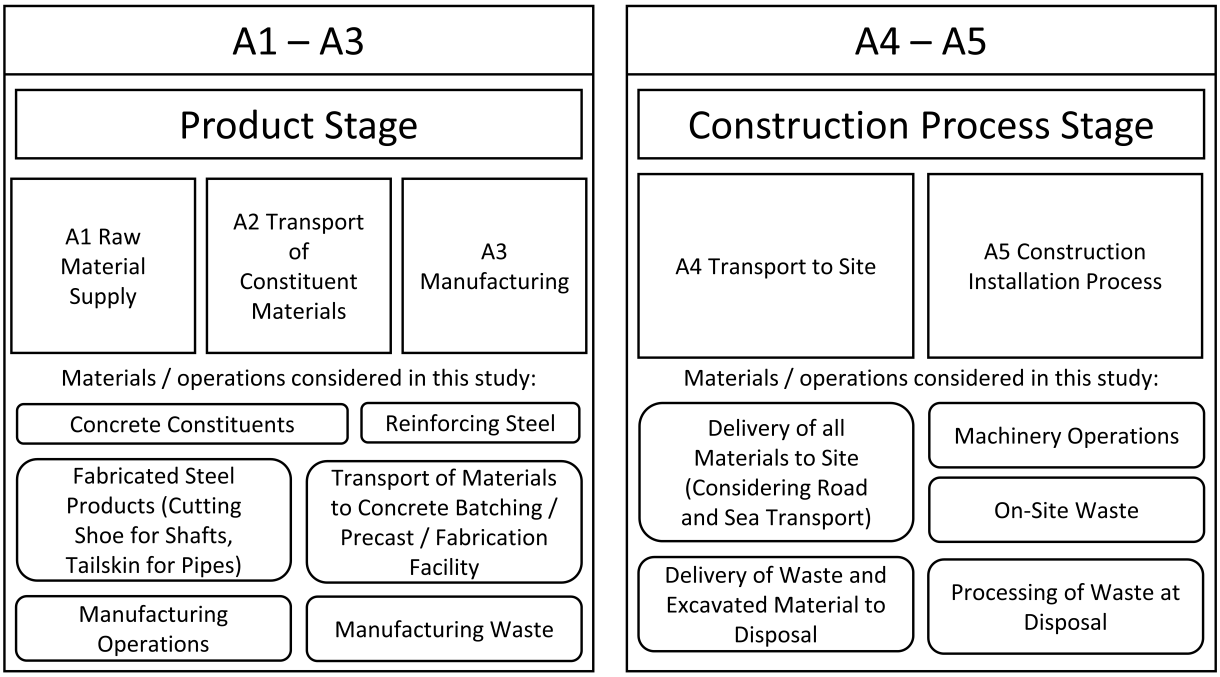


Figure 3.3: The materials and operations considered in this study and their associated life cycle modules as defined in BS EN 15978:2011.

3.3 Methodology

Material-related EC is calculated based on the mass of the materials and the corresponding embodied carbon factor (ECF) as follows (IStructE, 2020):

$$EC_i\,(\mathrm{kgCO_2e}) = m_i\,(\mathrm{kg}) \times ECF_i\,(\mathrm{kgCO_2e/kg}) \tag{3.1}$$

where m denotes mass and i denotes the relevant value for the i^{th} material/process. For transportation-related EC, the following expression is used in lieu of Equation 3.1:

$$EC_i\,(\mathrm{kgCO_2e}) = m_i\,(\mathrm{kg}) \times d_i\,(\mathrm{km}) \times ECF_i\,(\mathrm{kgCO_2e/kg/km}) \tag{3.2}$$

where d_i is the transportation distance for the i^{th} material. The unit used for EC is $\mathrm{kgCO_2e}$, where 'e' represents 'equivalent'. This study uses the same definition of $\mathrm{CO_2e}$ as Jones & Hammond (2019), which normalises the global warming potential of other greenhouse gases relative to the impact of one unit of $\mathrm{CO_2}$.

For Equations 3.1 and 3.2, three key sets of inputs are required for the EC calculations: (a) the mass of materials, (b) the distances transported, and (c) the relevant ECFs. Inputs considered as either 'fixed' or 'variable' for this study are presented in Table 3.1 and Table 3.2, respectively. In Table 3.1, input F1 is considered for all materials requiring processing before delivery to site. This distance is used to account for the delivery of concrete constituent materials to the concrete batching plant; delivery of concrete constituent materials and reinforcing

Table 3.1: Fixed inputs required to carry out analysis, associated units, and source of value.

Label	**Input**	**Value**	**Unit**	**Source**
F1	Delivery distance constituent materials to manufacturing facility/plant	50	km	Table 2.5 in IStructE (2020). Assumed same for all manufacturing facilities
F2	Mixing Waste Batching Concrete	1	%	ICE Cement, Mortar and Concrete Model (Jones & Hammond, 2019)
F3	On Site Waste	5	%	Table 2.6 in IStructE (2020)
F4	Delivery Distance Site to Disposal	50	km	Table 2.5 IStructE (2020)

steel to the precast plant; and the delivery of steel plate to the fabrication plant. Input F2 assumes an additional 1% of concrete constituent materials are required to account for wastage during processing, input F3 assumes 5% additional steel reinforcement and concrete are required to account for wastage on-site, and input F4 accounts for the removal of this waste away from site.

Table 3.2: Variable inputs required to carry out analysis, associated units, and source for finding the required information. GGBS = Ground Granulated Blast-furnace Slag.

Label	**Input**	**Unit**	**Source**
V1	Cement (CEMI)	kg/m^3	From concrete mix design
V2	GGBS	kg/m^3	"
V3	Limestone	kg/m^3	"
V4	Water/Cement Ratio	-	"
V5	(Super)Plasticiser	kg/m^3	"
V6	Aggregates	kg/m^3	"
V7	Steel Plate Fabrication	kg/m^3	From pipe design/shaft design
V8	Precast or In-Situ?	N/A	Pipes precast, shafts poured in-situ
V9	Reinforcing Steel	kg/m^3	From pipe design/shaft design
V10	Total Concrete Volume	m^3	Total volume of concrete in tunnel/shaft from design
V11	Volume Excavated Material	m^3	Total volume of soil removed to construct shaft/tunnel – from tunnel/shaft design
V12	Excavated Material Unit Mass	kg/m^3	Unit mass of soil excavated to construct shaft/tunnel – from tunnel/shaft design
V13	Delivery Distance to Site (Distance by Road)	km	Weighted average for materials considered if distances known – information from contractor. If distances unknown, 50 km assumed (Table 2.5 in IStructE, 2020)
V14	Delivery Distance to Site (Distance by Sea)	km	Weighted average for materials considered if distances known - information from contractor. If distances unknown, 0 km assumed
V15	Diesel Volume	l	Total volume of diesel used during construction of tunnel/shaft – information from contractor

In Table 3.2, inputs V1–V12 are used to define quantities of materials and are hence derived from the structural design obtained from the contractor. Delivery distances (inputs V13 and V14), considering both road and sea transport, are based on information provided by the contractor or typical distances in the absence of specific information. Diesel use (V15) is also based on information from the contractor and is an expedient indicator of emissions produced by on-site machinery as all machinery for the present case studies is either diesel-powered or electric, but in turn powered using diesel generators e.g. TBMs.

Table 3.3 shows the ECFs used for all calculations in this study. It is important that the adopted ECFs are current. It is therefore suggested that future studies follow the sources used in this study to check for updated values. Temporally, the values in Table 3.3 were chosen considering the present case studies were constructed between 2019 and 2021. The ECFs used are tailored for typical UK construction materials, except for steel products, where the specific location of production was considered. Six of the material ECFs are taken from the ICE Database (Jones & Hammond, 2019), which is a reliable open-access resource for the EC of construction materials in the UK (Hojjati et al., 2018). For the reinforcing steel, an Environmental Product Declaration was available online from the supplier (MEGASA, 2019), providing an ECF specific to the present case studies. Mill certificates obtained from the contractor indicated the steel plate was made in Korea in a basic oxygen furnace. Thus, the world average value was used (Jones & Hammond, 2019). The reinforcing steel was produced in Portugal, using an electric arc furnace with 92% recycled content (MEGASA, 2019), leading to a significantly lower ECF (0.655 $kgCO_2e/kg$) compared to the steel plate (2.46 $kgCO_2e/kg$), which was produced in a basic oxygen furnace. Transport and diesel ECFs are taken from UK Government Greenhouse Gas Conversion Factors (DEFRA, 2021). Two approaches are used for considering manufacturing facility operational carbon. For operations at the concrete batching plants and precast plants, ECF values are taken from independent industry bodies for UK-based concrete suppliers (MPA, 2020; MPA Precast, 2020). Both values are increased by 20%, as recommended by Jones & Hammond (2019), to convert $kgCO_2$ to $kgCO_2e$, accounting for other greenhouse gases and aligning the units with other ECFs used in this study. For fabricated steel, no equivalent values are available in the published literature. However, Gervasio & Dimova (2018) noted cutting and welding of steel plates accounts for 10% of the whole-life

CO_2 emissions. Therefore, fabrication operational carbon is obtained by increasing the ECF given in the ICE Database by 10%. The same waste processing ECF is assumed for all materials and all forms of disposal.

Table 3.3: Embodied Carbon Factors (ECFs) used to carry out the analysis.

Material/ Process	**ECF**	**Unit**	**Source**
Cement (CEMI)	9.12 x 10^{-1}	$kgCO_2e/kg$	ICE Database (Jones & Hammond, 2019)
GGBS	4.16 x 10^{-2}	$kgCO_2e/kg$	"
Limestone	1.58 x 10^{-2}	$kgCO_2e/kg$	"
Water	1.49 x 10^{-4}	$kgCO_2e/kg$	DEFRA (2021)
Plasticiser	1.88 x 10^{0}	$kgCO_2e/kg$	ICE Database (Jones & Hammond, 2019)
Aggregates	7.47 x 10^{-3}	$kgCO_2e/kg$	"
Transport (road)	1.06 x 10^{-4}	$kgCO_2e/kg/km$	All HGV - Average laden HGV (DEFRA, 2021)
Transport (sea)	5.17 x 10^{-5}	$kgCO_2e/kg/km$	Roll-on-Roll-off Ferry Average (DEFRA, 2021)
Batching plant operations	6.00 x 10^{-4}	$kgCO_2/kg$	MPA (2020). Value shown uplifted by 20% in analysis to convert to CO_2e (Jones & Hammond, 2019)
Precast plant operations	9.79 x 10^{-3}	$kgCO_2/kg$	MPA Precast (2020). Value shown uplifted by 20% in analysis to convert to CO_2e (Jones & Hammond, 2019)
Reinforcing steel	6.55 x 10^{-1}	$kgCO_2e/kg$	MEGASA (2019)
Steel plate fabrication	2.46 x 10^{0}	$kgCO_2e/kg$	ICE Database (Jones & Hammond, 2019). Value shown increased by 10% in analysis to account for fabrication (Gervasio & Dimova 2018)
Diesel	3.14 x 10^{0}	$kgCO_2e/litre$	DEFRA (2021). Value shown is the sum of the well-to-tank and fuel conversion factors
Waste processing	1.30 x 10^{-2}	$kgCO_2e/kg$	Eq. (2.8) in IStructE (2020)

Python programming (version 3.8) was used to integrate the inputs summarised in Table 3.1-3.3 with Equations 3.1 and 3.2 for efficient calculation and to maximise the possibility of industry adoption. The workflow of the code is shown in Figure 3.4, with supplementary information provided in Table 3.4.

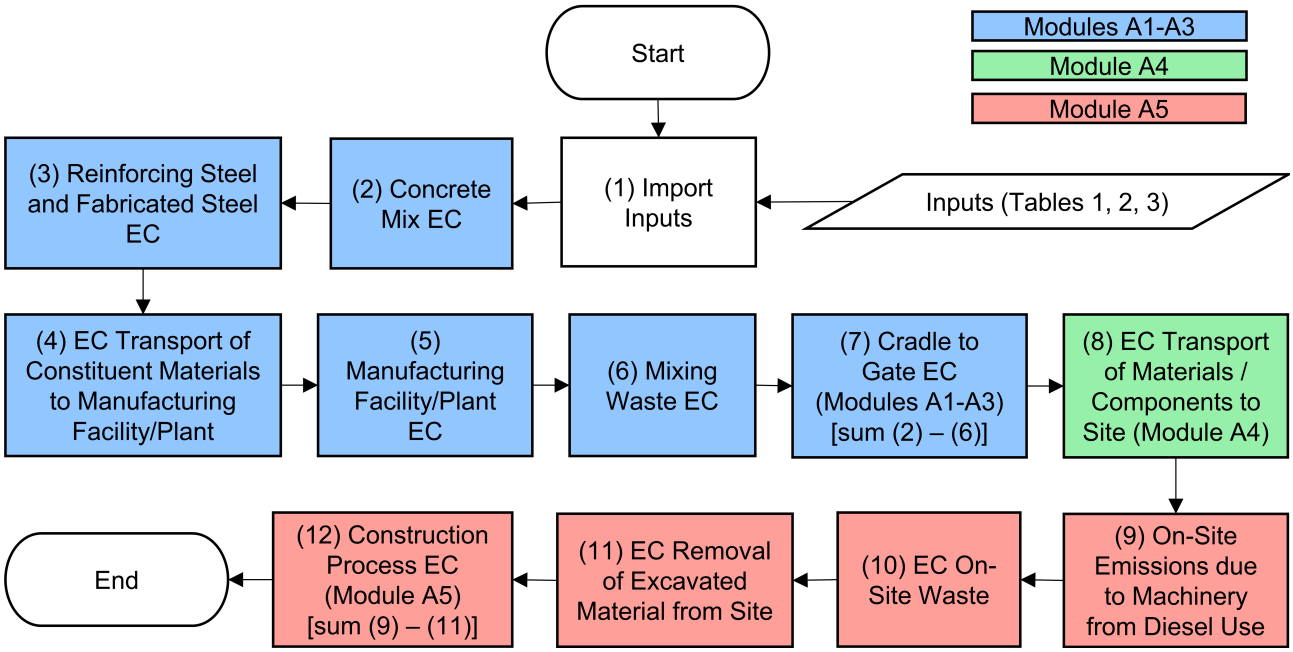


Figure 3.4: Calculation steps implemented in Python to analyse the EC of the case studies presented in this chapter. See Table 3.4 for supplementary information.

Table 3.4: Supplementary information for EC calculation steps in Figure 3.4.

Calculation Step	**Caveat(s)**
(4)	1. Exclude water 2. If in-situ: exclude reinforcement 3. If precast: include reinforcement
(5)	1. If in-situ: 'Batching Plant Operations' ECF and exclude reinforcing steel mass 2. If precast: 'Precast Plant Operations' ECF
(6)	1. Assume zero reinforcement waste. On site reinforcement waste for in-situ considered later 2. Exclude 'Steel Plate Fabrication' mass - waste accounted for in ECF
(10)	1. If in-situ: consider A1-A3 EC of additional material, delivery of additional material to site and away from site to disposal, and processing of waste at disposal 2. If precast: assume zero

3.4 Case Study 1

Case study 1 (CS1) is a network of tunnels in the UK constructed in soft clay to divert existing gravity sewers to enable the construction of a new road junction. The final design consisted of three 1.2 m internal diameter (ID), 1.49 m outer diameter (OD) tunnels with lengths of 168, 48 and 144 m (see Figure 3.5). All three tunnels originate from a 6 m ID launch shaft and terminate at three 4 m ID reception shafts. Due to the tunnel gradients, all shafts had slightly different depths and the cover to the tunnels at shaft locations varies between 2.23 and 3.36 m. The depth of shaft bases varies depending on the shaft diameter.

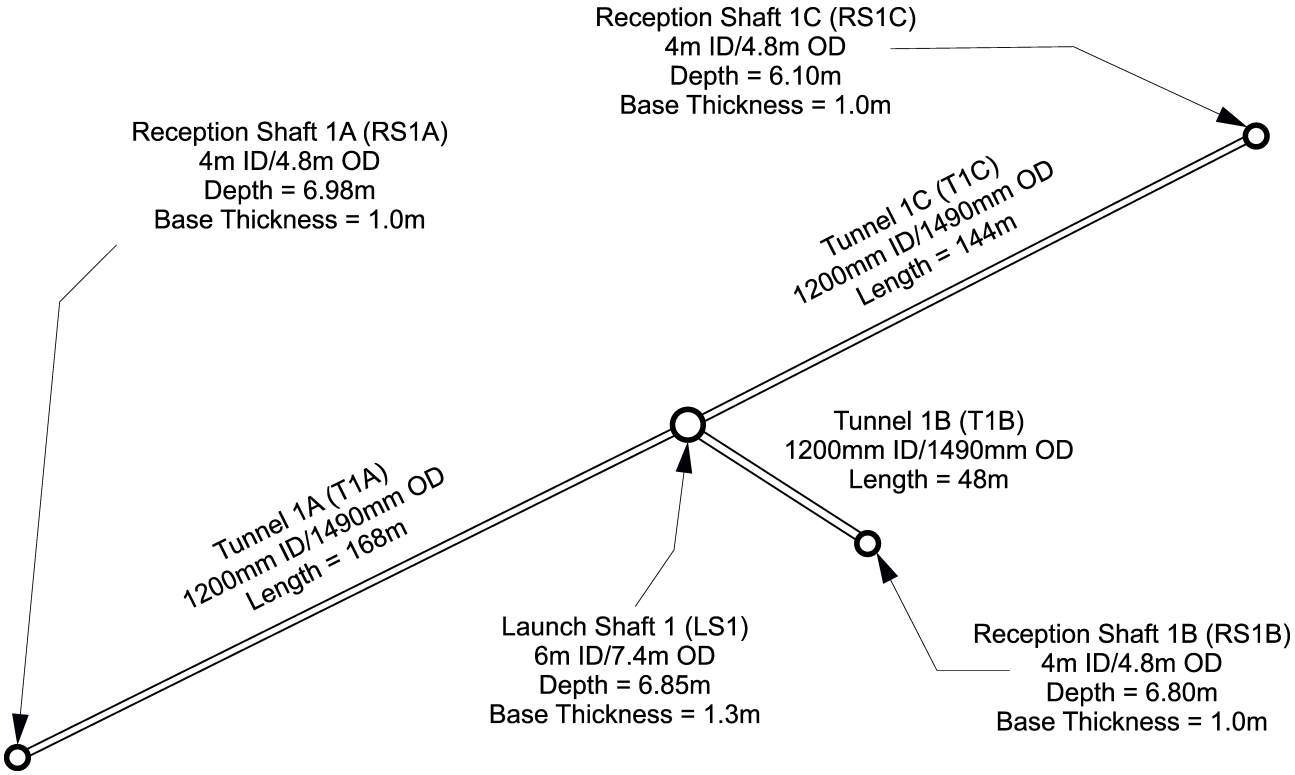


Figure 3.5: Case study 1 (CS1) site showing shaft and tunnel details. 'Depth' refers to total depth i.e., top of shaft to formation level. 'Base Thickness' refers to total base thickness including unreinforced plug and reinforced structural base.

Fixed inputs for analysis are presented in Table 3.5. The delivery distance for tunnel pipe sections is known, whilst the delivery distance for the in-situ concrete for shafts is unknown and hence assumed as 50 km. Table 3.6 presents the variable inputs determined for each tunnel and shaft in CS1.

Figure 3.6 presents the EC for each tunnel and shaft, categorised by modules A1–A5 (a full breakdown of results can be found in Appendix A). The overall magnitude of EC for the project is significant, with the total EC for the three tunnels and four shafts totalling 378

Table 3.5: Case study 1 & 2 fixed inputs for tunnels and shafts. Input sources detailed in Table 3.2.

Input	Unit	Tunnels	Shafts
Cement (CEMI)	kg/m^3	400	193
GGBS	kg/m^3	0	197
Limestone	kg/m^3	207	0
Water/Cement Ratio	-	0.355	0.45
(Super)Plasticiser	kg/m^3	3.25	2.1
Aggregates	kg/m^3	1586	1810
Precast or In-Situ?	N/A	Precast	In-Situ
Delivery Distance to Site (by Road)	km	520	50
Delivery Distance to Site (by Sea)	km	110	0
Excavated Material Unit Mass	kg/m^3	1700	1700

Table 3.6: Case study 1 variable inputs for tunnels and shafts. Input sources detailed in Table 3.2.

Input	Unit	T1A	T1B	T1C	LS1	RS1A	RS1B	RS1C
Steel Plate Fabrication	kg/m^3	61.7	61.7	61.7	24.1	42.1	42.9	46.5
Reinforcing Steel	kg/m^3	153.5	153.5	153.5	89.9	46.2	49.0	49.2
Total Concrete Volume	m^3	102.9	29.4	88.2	137.7	51.1	50.2	46.3
Diesel Volume	l	5380	3552	6189	2260	1400	1400	900
Volume Excavated Material	kg/m^3	293	84	251	295	126	123	110

tCO_2e. Based on an average value of 3 tCO_2e per car per year (IStructE, 2020), this equates to running approximately 129 petrol cars over a period of one year. Modules A1-A3, involving the production of materials and components, dominate emissions, accounting for 67.7% of the total EC.

For this project, the EC associated with tunnelling is notably greater than that associated with shaft construction (by a factor of 1.8). However, the total volume of concrete used for the tunnels (221 m^3) is lower than that for the shafts (285 m^3). The higher tunnel EC, despite a lower concrete volume, is due to a combination of the high reinforcing steel density required to

resist jacking forces and surface loading on the pipes, and the use of a higher concrete grade and hence notably greater cement content (C50/60 instead of C35/45 for the shafts - see Table 3.5).

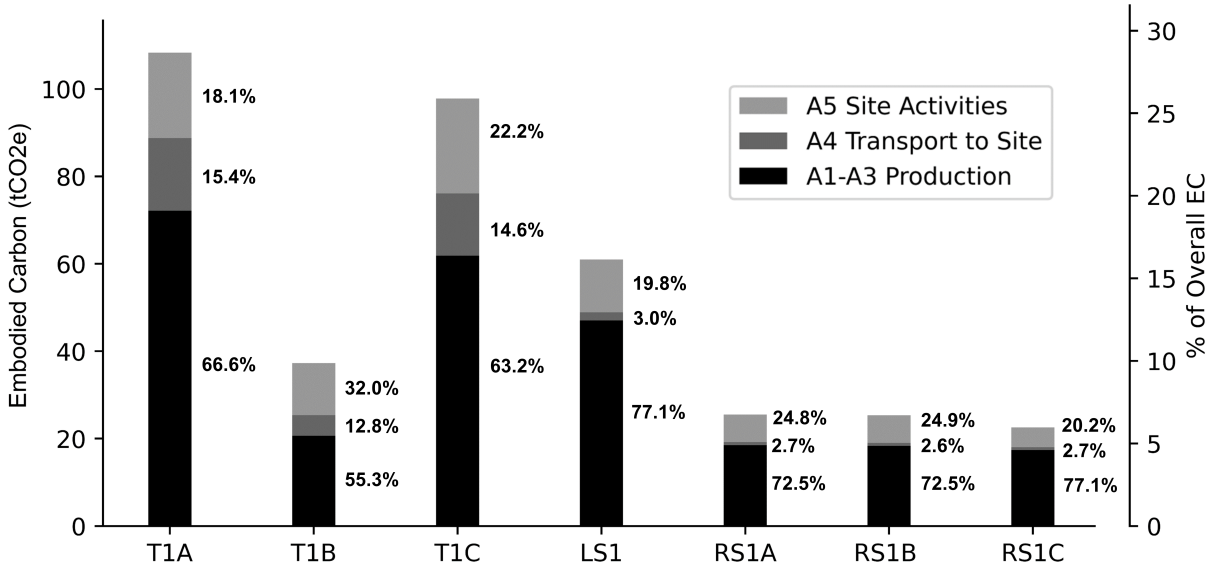


Figure 3.6: EC of tunnels and shafts in CS1 plotted in terms of modules A1-A5. The secondary axis denotes the percentage contribution to the overall EC of the case study, whilst percentage labels on each bar denote the relative contribution of each module to the EC of the relevant structure.

3.5 Case Study 2

Case study 2 (CS2) is also a network of tunnels in the UK constructed in soft clay to divert a section of an existing sewer network. The final design involved two tunnels and three shafts as shown in Figure 3.7. Both tunnels originate from a 7 m ID launch shaft, with the 1.2 m ID tunnel terminating at a 4 m ID reception shaft and the 1.5 m ID tunnel terminating at a 5 m ID reception shaft. The cover to the tunnels varies between 1.74 and 2.15 m. Fixed inputs for analysis are the same as those adopted for CS1 as presented in Table 3.5. The variable inputs for each tunnel and shaft are presented in Table 3.7.

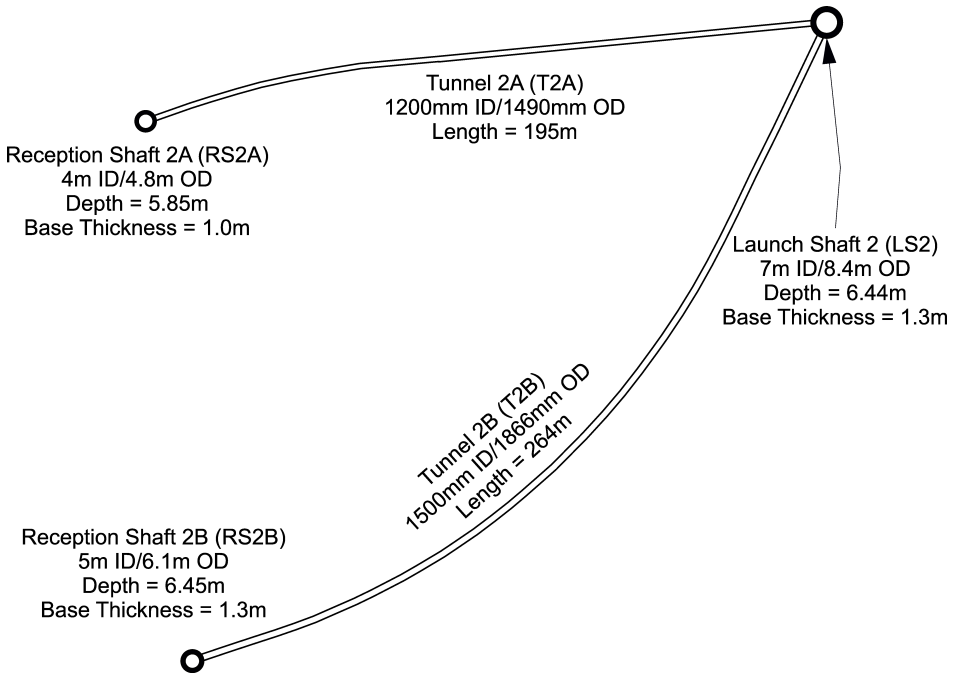


Figure 3.7: Case study 2 (CS2) site showing shaft and tunnel details. 'Depth' refers to total depth i.e., top of shaft to formation level. 'Base Thickness' refers to total base thickness including unreinforced plug and reinforced structural base.

Table 3.7: Case study 2 variable inputs for tunnels and shafts. Input sources detailed in Table 3.2.

Input	Unit	T2A	T2B	LS2	RS1A	RS1B
Steel Plate Fabrication	kg/m^3	61.7	36.7	23.6	48.0	31.3
Reinforcing Steel	kg/m^3	153.5	145.6	147.4	55.3	42.6
Total Concrete Volume	m^3	119.5	255.4	159.1	44.9	87.3
Diesel Volume	l	7562	8547	1600	923	1318
Volume Excavated Material	kg/m^3	340	722	357	106	188

The EC calculated for each tunnel and shaft is plotted in Figure 3.8 (full breakdown in Appendix A). The overall magnitude of EC for this project is 498 tCO_2e. The trends in Figure 3.8 are similar to those observed for CS1. Modules A1-A3 account for 70.4% of all emissions and the tunnels make a greater contribution to the EC than the shafts, this time by a factor of 2.74. T2B, which has the largest diameter and is the longest tunnel considered in this chapter, has the lowest relative contribution from A5 emissions (19.3%) of any of the tunnels studied. The size of reception shafts is typically driven by the diameter of the pipe and hence the space required for removal of the TBM. As a result, RS2A, which has a lower diameter, has approximately 40% lower EC than RS2B, demonstrating the value of optimising the design of shafts independently.

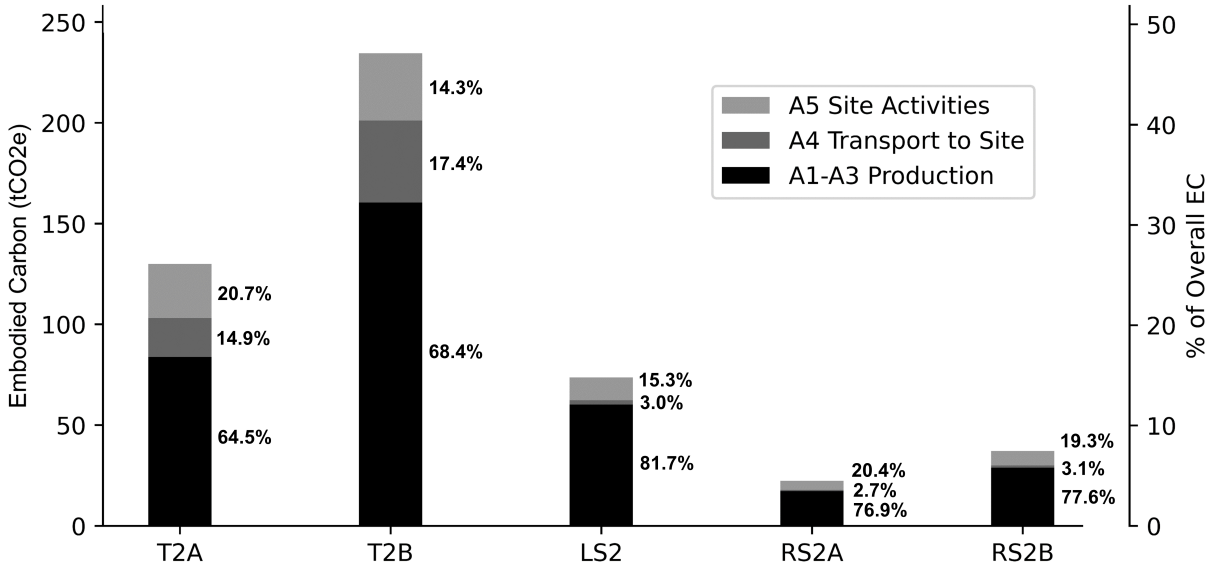


Figure 3.8: EC of tunnels and shafts in CS2 plotted in terms of modules A1-A5. The secondary axis denotes the percentage contribution to the overall EC of the case study, whilst percentage labels on each bar denote the relative contribution of each module to the EC of the relevant structure.

3.6 Case Study 3

Case study 3 (CS3) considers a tunnel in the UK constructed in medium-dense to dense gravel, used to carry a pipeline beneath a railway (Figure 3.9). The tunnel constructed is 1.2 m ID, 1.49 m OD, and 51 m in length. Both the launch and reception shafts have an ID of 5 m, with cover to the tunnel of 6.06 m at the launch shaft and 5.51 m at the reception shaft.

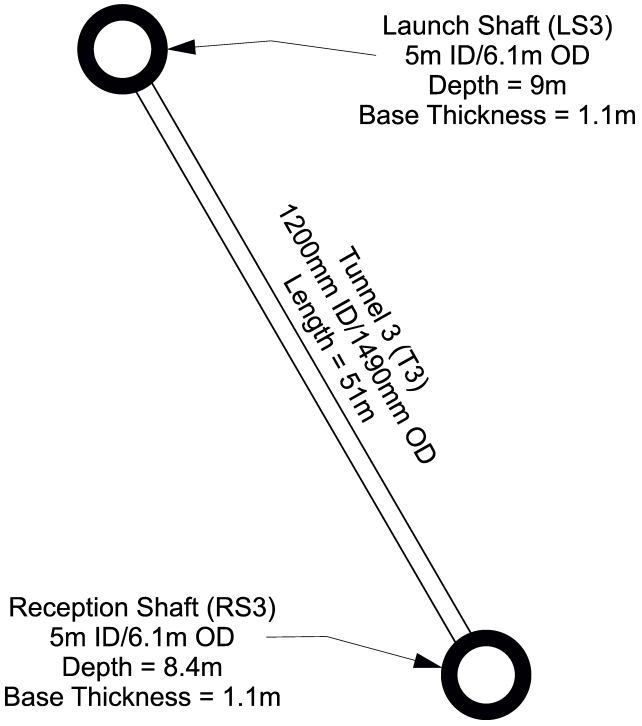


Figure 3.9: Case study 3 (CS3) site showing shaft and tunnel details. 'Depth' refers to total depth i.e., top of shaft to formation level. 'Base Thickness' refers to total base thickness, which in this case is entirely unreinforced.

Fixed inputs are provided in Table 3.8. The shaft designs specified C32/40 concrete for the reinforced walls, and C50/60 for unreinforced bases, resulting in different inputs for the walls and bases of the shafts. The delivery distance for tunnel pipe sections is known, whilst the delivery distance for the in-situ concrete for shafts is unknown and hence assumed to be 50 km. Table 3.9 contains the variable inputs, with the shaft walls and bases again considered separately.

Table 3.8: Case study 3 fixed inputs for tunnels and shafts. Input sources detailed in Table 3.2.

Input	Unit	Tunnels	Shaft Walls	Shaft Bases
Cement (CEMI)	kg/m^3	400	173	248
GGBS	kg/m^3	0	177	252
Limestone	kg/m^3	207	0	0
Water/Cement Ratio	-	0.355	0.42	0.40
(Super)Plasticiser	kg/m^3	3.25	1.8	3.1
Aggregates	kg/m^3	1586	1844	1657
Precast or In-Situ?	N/A	Precast	In-Situ	In-Situ
Delivery Distance to Site (by Road)	km	460	50	50
Delivery Distance to Site (by Sea)	km	60	0	0
Excavated Material Unit Mass	kg/m^3	2100	2100	2100

Table 3.9: Case study 3 variable inputs for tunnels and shafts. Input sources detailed in Table 3.2.

Input	Unit	Tunnel	LS Walls	LS Base	RS Walls	RS Base
Steel Plate Fabrication	kg/m^3	43.7	31.7	0	33.8	0
Reinforcing Steel	kg/m^3	144.9	24.8	0	26.4	0
Total Concrete Volume	m^3	31.2	86.3	21.6	81.0	21.6
Diesel Volume	l	5258	2000		2500	
Volume Excavated Material	kg/m^3	88.9	263.0		246.8	

The EC calculated for the tunnel and shafts is plotted in Figure 3.10 (full breakdown in Appendix A). The overall magnitude of EC for the project is 130 tCO_2e. Although A1-A3 dominate the emissions (63.6% of total), the contribution is lower than in CS1 and CS2. This is attributed to the high A5 emissions associated with the tunnel, which represent a much higher proportion of overall EC than observed for the tunnels in CS1 and CS2 (31.1% for CS3, 16.7% for CS2, and 21.8% for CS1). This is probably because tunnelling operations in the medium-dense to dense gravel of CS3 are more energy-intensive than in the soft clay of CS1 and CS2. In this case, the shafts make a greater contribution to the overall EC (67.7%) compared to the

tunnel because: (a) the ratio of shafts to tunnels is greater than in CS1 and CS2; (b) the shafts are deeper (8.4 and 9 m); and (c) the tunnel in CS3 is shorter (51 m).

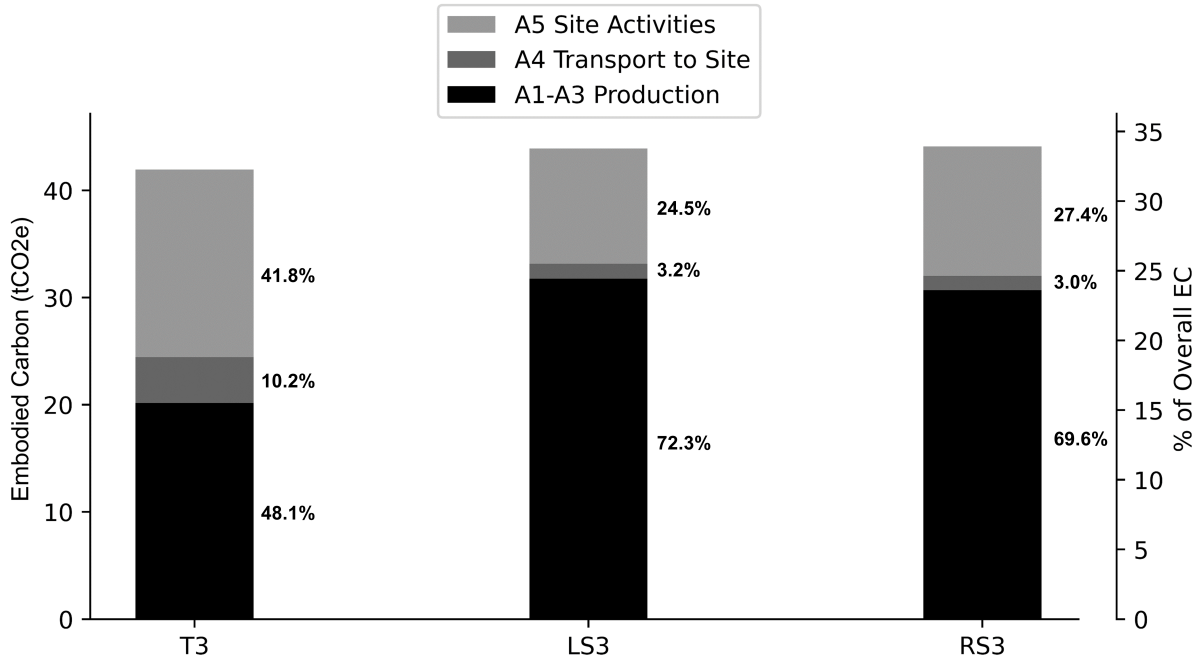


Figure 3.10: EC of tunnels and shafts in CS3 plotted in terms of modules A1-A5. The secondary axis denotes the percentage contribution to the overall EC of the case study, whilst percentage labels on each bar denote the relative contribution of each module to the EC of the relevant structure.

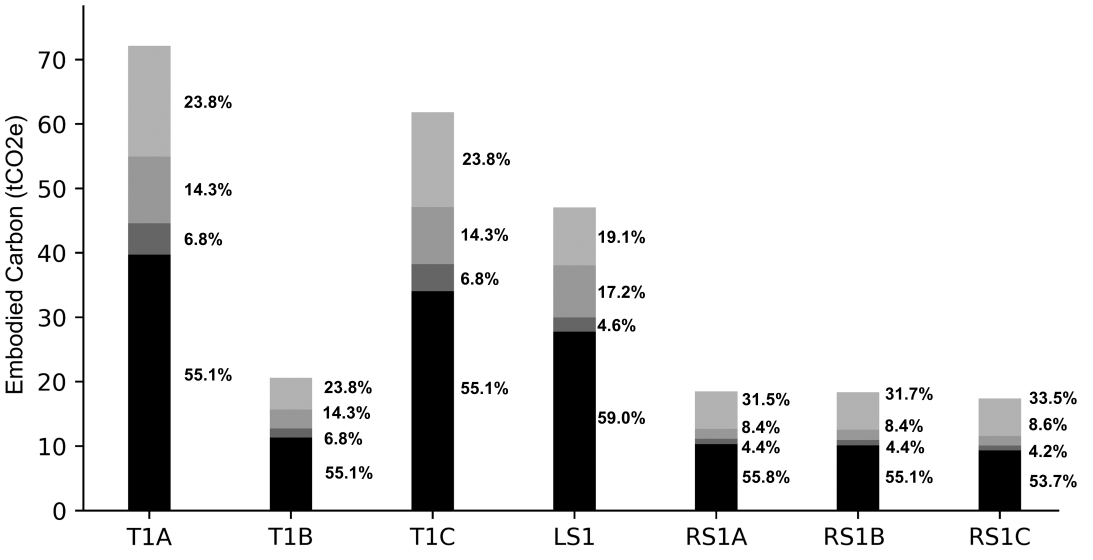
To accommodate jacking equipment and jacking forces exerted on the shaft, launch shafts often have a larger diameter, thicker walls, and typically higher steel reinforcement density than reception shafts. However, in CS3, near-identical shafts were used due to on-site constraints, leading to nearly equal contributions to overall EC. Comparing these results to CS1 and CS2, where distinctive shaft designs were used for launch and reception shafts, underlines the value of optimising the design of shafts independently.

3.7 Emissions Breakdown

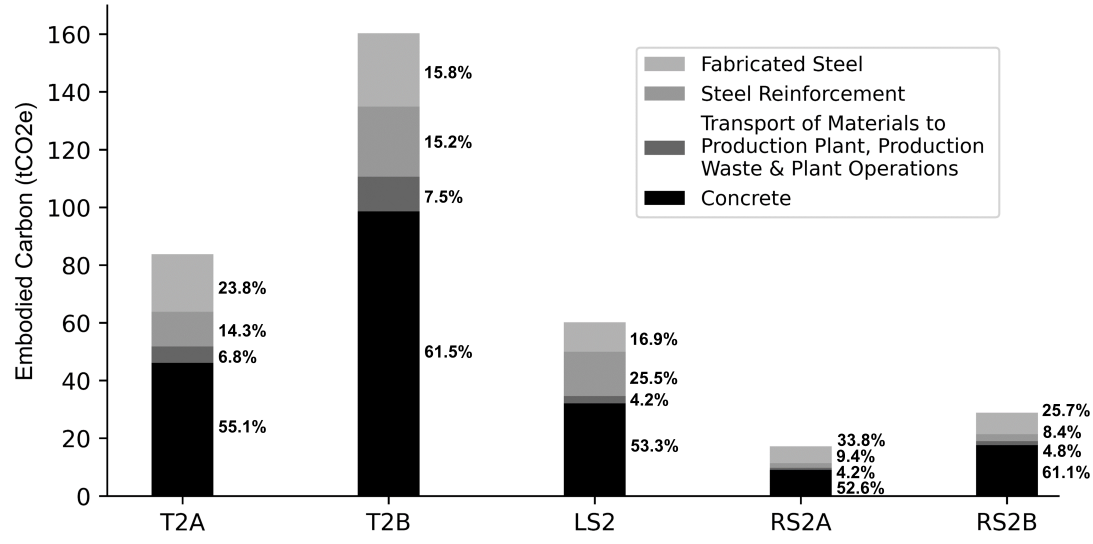
3.7.1 A1-A3 (Off-Site Production)

Across all three case studies, modules A1-A3 account for 68.5% of the total EC and have been replotted in Figure 3.11, this time broken down into the constituent materials and processes. The biggest contributor to A1-A3 EC in all three case studies is concrete. Concrete accounts for 55.8% of A1-A3 EC in CS1, 58.1% in CS2, and 64.9% in CS3. Concrete EC is especially high in CS3 due to the shafts, which have high cement content for the unreinforced shaft bases and relatively low reinforcement in the walls (see Tables 3.8 and 3.9), which reduces the contribution of steel reinforcement. The high EC contribution of concrete underlines the need to (a) eliminate overly conservative design and reduce material use, and (b) develop and adopt low EC concrete technology.

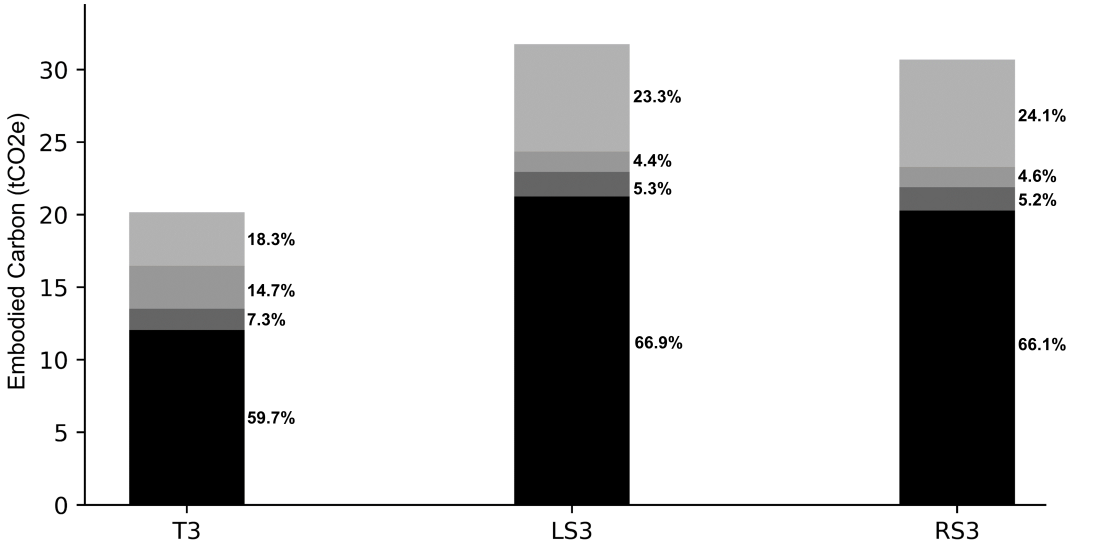
Figure 3.11 also shows, albeit to a lesser extent than concrete, fabricated steel components make a significant contribution to A1-A3 EC (24.7% for CS1, 19.6% for CS2, and 18.5% for CS3). The relative contribution is especially high for the small diameter (ID = 4 m) reception shafts in CS1 and CS2, where the mass of fabricated steel per unit volume of concrete is significantly greater (see Tables 3.6 and 3.7). CS2 provides a comparison of two different pipe designs: T2A (ID = 1.2 m) and T2B (ID = 1.5 m). Fabricated steel makes a lower contribution for T2B (15.8%) than T2A (23.8%). This is due to each pipe being 4 m in length, rather than 3 m in length, leading to a reduction in the number of tailskins required per m length of tunnel. This benefit may however be partially offset by the need for a larger diameter launch shaft to accommodate the longer pipe lengths.



(a)



(b)



(c)

Figure 3.11: EC from modules A1-A3 for tunnels and shafts, subdivided into constituent materials and processes for (a) CS1, (b) CS2, & (c) CS3. Percentage labels on each bar denote the relative contribution of each constituent material/process to the A1-A3 EC of the relevant structure.

3.7.2 A4 (Transport to Site)

A4 emissions for shafts are all relatively low, with the maximum contribution to overall emissions (3.2%) observed for the launch shaft in CS3 (Figure 3.10). This is due to the materials used for in-situ concrete being typically sourced locally and the delivery distance hence assumed to be 50 km in all cases. A4 emissions for the tunnels are much higher (e.g. T2B, where A4 contributes 17.4% to overall emissions; Figure 3.8). This is due to much greater delivery distances from the precast factory (see Tables 3.5 and 3.8), thus highlighting the potential impact of establishing local suppliers.

3.7.3 A5 (On-Site Activities)

For the three case studies considered, A5 emissions were proportionally larger for shorter tunnel drives. By way of example, Figure 3.12 plots A5 emissions, normalised by total tunnel volume, against tunnel length. A5 accounts for 32.0% and 14.3% of total EC for the shortest (T1B) and longest (T2B) tunnels respectively. This is because emissions related to tunnelling mobilisation and demobilisation are insensitive to drive length, increasing the relative contribution of A5 emissions for shorter drives. Figure 3.12 also suggests larger diameter pipes have lower A5 emissions per unit volume tunnel constructed and that tunnelling is more energy-intensive in medium-dense to dense gravels (CS3) compared to soft clay (CS1 and CS2). It is also noteworthy that machinery use accounts for 77.4% of A5 tunnelling emissions. At present, TBMs are typically powered using on-site diesel generators. Based on the net calorific value of diesel (0.256 $kgCO_2e/kWh$), the well-to-tank factor for diesel (0.061 $kgCO_2e/kWh$), and assuming 100% generator efficiency, the ECF for electricity generated on-site is 0.317 $kgCO_2e/kWh$ (DEFRA, 2022). At the time of writing, the average ECF for mains electricity in the UK is 0.194 $kgCO_2e/kWh$ (DEFRA, 2022). As such, using mains electricity instead of generators could reduce TBM emissions by at least 39%. Actual savings would be higher, given the conservative assumption of 100% generator efficiency. Furthermore, as the ECF for mains electricity is set to decrease year on year, future savings will be even greater.

Similar trends are evident for the shafts, with larger structures showing the lowest relative A5 emissions. For example, the smallest contribution (15.3%) was calculated for the shaft with the greatest ID (LS2; Figure 3.8). This relationship is likely due to a combination of three factors:

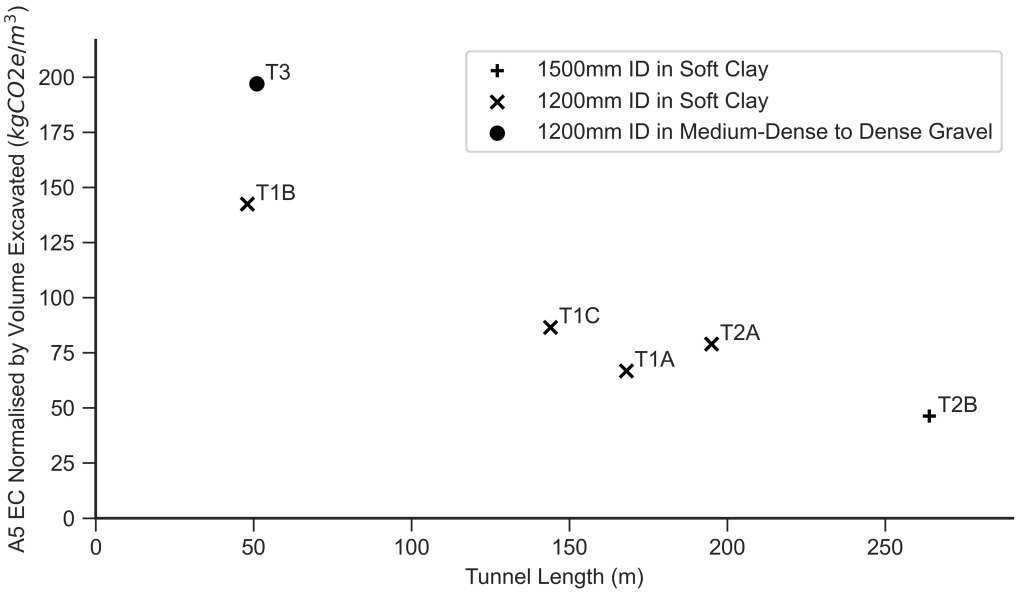


Figure 3.12: A5 emissions for the tunnels normalised by the volume of material excavated.

(1) the burden-shifting effect of mobilisation and demobilisation being an approximately fixed EC cost, thereby increasing the relative contribution for smaller shafts; (2) variations in the density of reinforcing steel in the shafts; and (3) ground conditions.

3.8 Summary

In this chapter, a methodology to analyse the EC of core MT processes was presented. To identify the EC associated with modern MT, a project database was developed in collaboration with industry partners. By way of example, the proposed methodology was applied to three exemplar UK case histories which had high-quality project records to explore the influence of construction stages/processes. The framework developed was bespoke for the three projects considered and focused specifically on open caisson shaft construction. Application of the methodology to other projects may require further development. At present, extrapolating the data presented to analyse the EC of other projects would be inexpedient.

Emissions across all three projects amounted to 1,005 tCO_2e. The contributions of both tunnels and shafts to the overall emissions are substantial. Production of materials and components (Modules A1-A3) was shown to account for 68.5% of EC across the three projects, with the majority of these emissions coming from concrete production. Steel reinforcement and fabricated steel components made up a smaller, but still significant contribution to A1-A3 EC.

Given the dominance of A1–A3 emissions, particularly from concrete, a key area for future

research should be the potential impact of advancements in material technology. Additionally, improvements in design methods for jacking pipes and shafts could facilitate reductions in material usage and, consequently, EC. A4 emissions (delivery of materials to site) were significant where delivery distances were greater, particularly for the pre-cast pipes, highlighting the importance of using local suppliers where possible. Site activities (Module A5) account for 20.5% of total emissions across the three projects. Ground conditions were shown to have a significant influence on A5 EC for the tunnels. Shorter tunnels exhibited much higher emissions per metre tunnelled, due to the greater influence of the fixed EC cost of mobilising and demobilising tunnelling operations.

4 Laboratory Testing of Caisson-Soil Uplift Friction in Sand

4.1 Introduction

Currently, no dedicated method exists for calculating friction in resistance to uplift due to the use of bentonite during the sinking phase of caisson construction. As such, friction is routinely neglected in anti-flotation calculations. This gap in the literature results in total reliance on the self-weight of the structure in practice, leading to excessive material use. Allowance of even modest frictional resistances could contribute a significant uplift resistance force, especially for large-diameter and/or deep caissons. This chapter addresses this shortcoming by presenting results from an apparatus designed to simulate: (i) caisson sinking, (ii) grout injection, and (iii) the resulting friction during uplift. Quantitative results are obtained by measuring friction, whilst qualitative observations offer insights into grout behaviour during injection and failure mechanisms during uplift. The experiments in this chapter were undertaken in the geotechnical laboratory at the University of Oxford.

4.2 Laboratory Apparatus

Figure 4.1 presents pertinent features of the apparatus used in this chapter (developed by Templeman, 2022; Phillips, 2023). The apparatus simulates SSI that develops on the outside of a caisson during sinking and uplift by pulling modular test pieces (TPs), each with a concrete face, through a sand-filled tank. In each test, sinking is first simulated by pulling the TPs downwards through the tank, whilst simultaneously injecting lubricant at the interface through the integrated ports. The TPs are successively cycled around the system to allow modelling of large-deformation shearing, as observed during caisson sinking. The interface represents a reduced-scale plane-strain approximation of a caisson in the field, allowing for interface mechanics to be isolated and studied in detail. Whilst the lubricated interface created in the laboratory represents plane strain conditions, 'annulus' is the term used on-site and in the literature. As such, 'annulus' is also used in this chapter when discussing the present results.

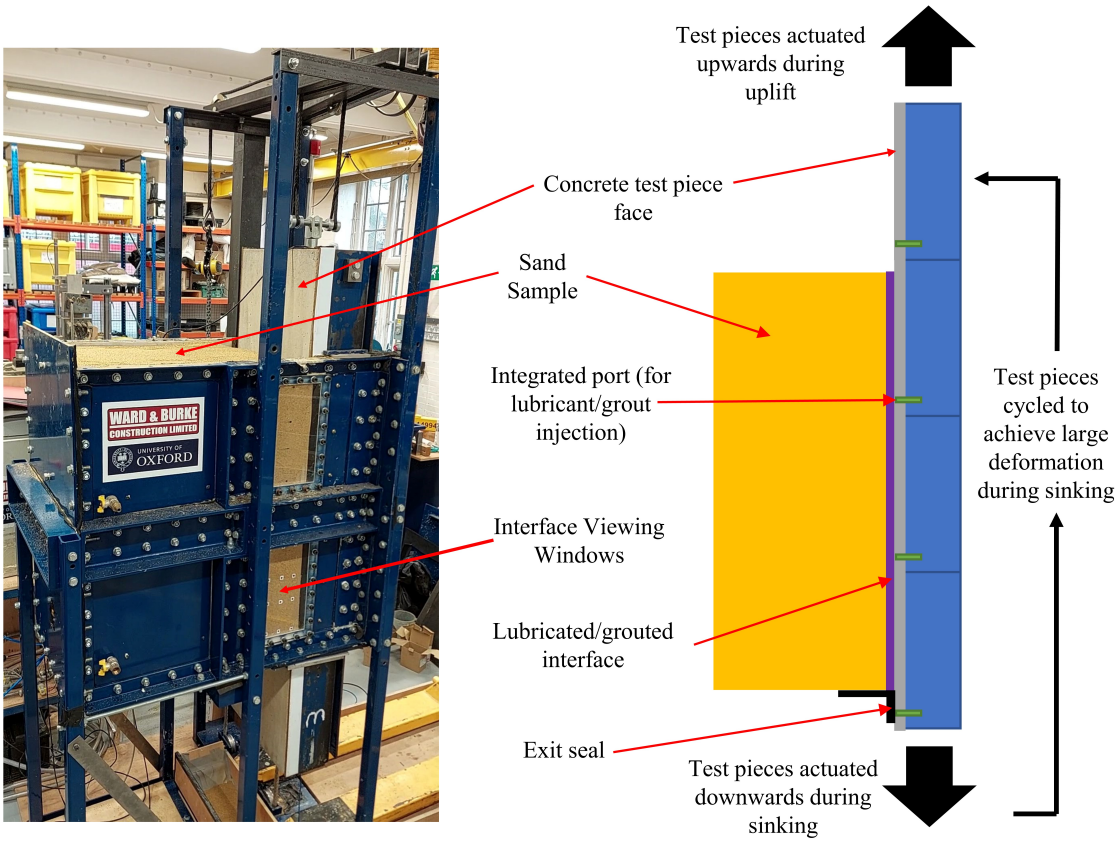


Figure 4.1: A photograph of the testing apparatus, alongside a simplified schematic of the testing apparatus (section view).

Once the sinking cycles are completed, grout is then injected into the annulus through the same ports used for lubrication injection, as is common in the field. After a prescribed rest period to allow the grout to harden, the direction of actuation is reversed, pulling the TPs upwards to simulate flotation. No cycling is required in this case, since only small deformations are required to simulate uplift behaviour in the field.

Figure 4.2 shows the test chamber, which creates a 1000 × 750 × 500 mm cuboid for containing the sand samples during testing. This creates a large interface (1000 mm long, 500 mm wide), minimising boundary effects from the tank edges. The tank includes a bespoke exit seal to minimise the loss of sand and lubricant where the TPs pass out of the tank.

The translation of TPs through the tank during sinking is achieved using a linear translating screw actuator (see Figure 4.2) attached to ropes in tension to form a continuous loop (see Figure 4.3a). Ratchet hoists are included in the rope loop to enable pre-tensioning of the system. During sinking, the bottom rope pulls the TPs through the tank and the top rope acts as a counterbalance to prevent any sudden slipping. During uplift, the bottom rope is removed,

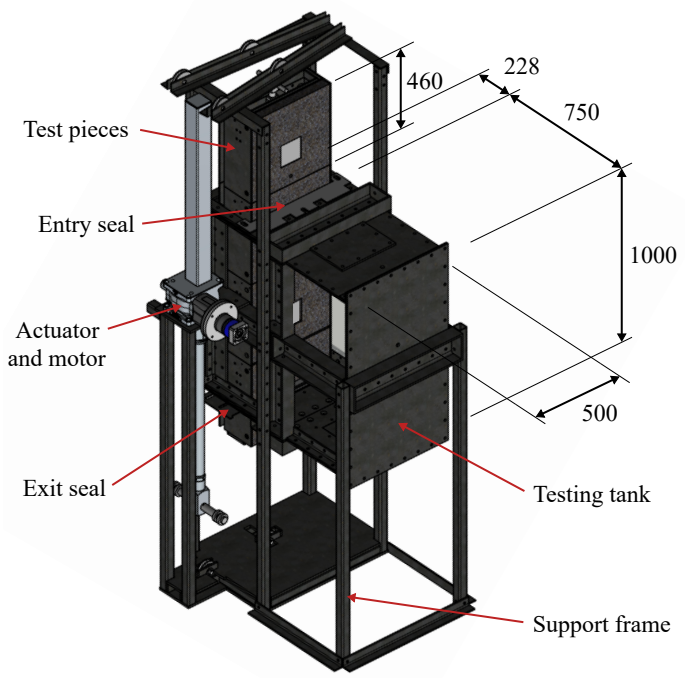


Figure 4.2: An isometric view of the testing apparatus (tank side panels and ropes not shown). Measurements are for one test piece (TP) and internal dimensions of testing tank (in mm). From Templeman (2022).

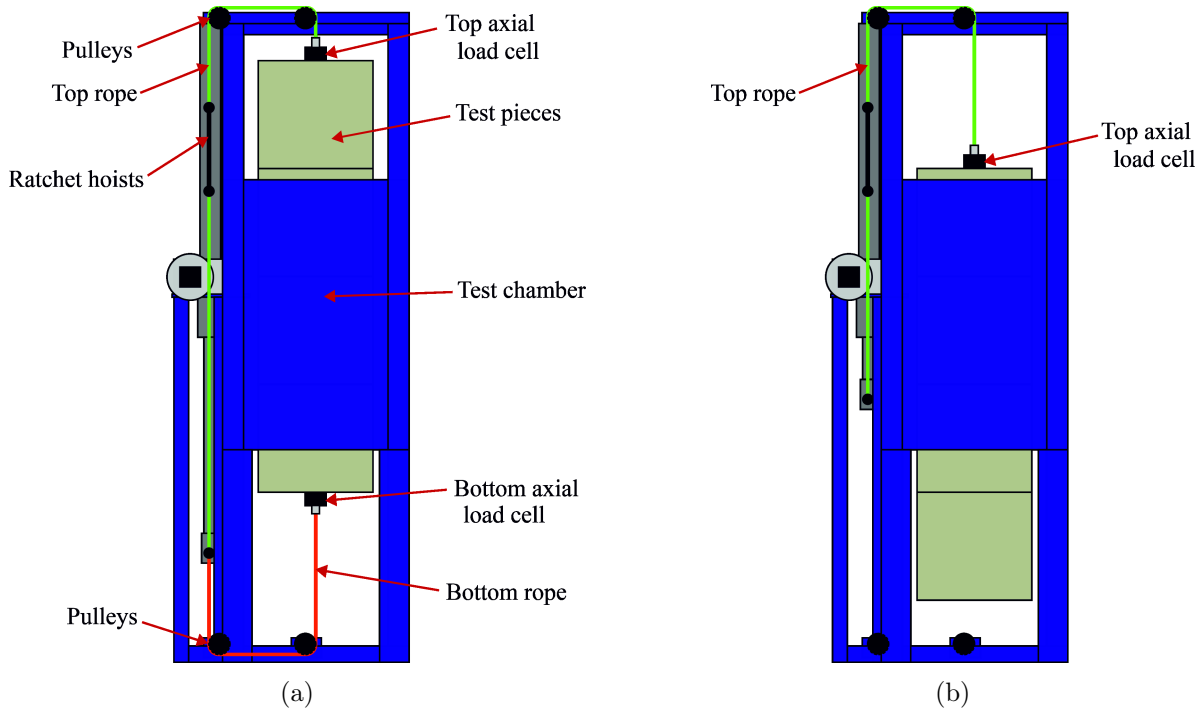


Figure 4.3: Schematics of the test apparatus actuation system set-up: (a) during sinking; and (b) during uplift. Adapted from Templeman (2022).

and the TPs are pulled upwards using the top rope only (Figure 4.3b). Axial load cells are installed at both ends of the rope loop, allowing actuation forces to be measured. A 50 kN

S-type tension/compression load cell (Force Logic FSB-5T) is used at the bottom of the TP train, whilst a 10 kN S-type tension/compression load cell (Applied Measurements DBBSM-1000kg) is used at the top. The displacement of the TPs during actuation is measured using an 800 mm long Temposonics® G-Series non-contact linear position sensor.

4.3 Experimental Methodology

4.3.1 Sand Sample

14/25 Leighton Buzzard sand was used for the present tests. Although there is a wide range of literature on the properties of Leighton Buzzard sand, key batch-specific parameters were obtained using standard characterisation tests and are presented in Table 4.1 (Templeman, 2022). The effective particle sizes were determined from sieve testing carried out in accordance with BSI (2016), classifying the sand as 'coarse' (ISO, 2017). To measure the critical state friction angle (ϕ_c), a series of direct shear tests were performed at three normal stress levels (σ_n = 50, 100, 150 kPa) on sand samples of two densities: dense ($D_R = 88 \pm 6\%$) and medium ($D_R = 55 \pm 3\%$).

Air pluviation was used to create repeatable, uniform sand samples in the testing tank. This method involves raining sand through an array of holes onto a mesh, which disperses the sand before it falls into the tank. The adopted rainer and methodology are described in Templeman (2022). This process consistently achieved uniform sand samples with a global dry unit weight of $\gamma_d = 16.13 \pm 0.11$ kN/m^3, which equates to a mean relative density of 72% with a standard deviation of 3.7%. This value was chosen to closely replicate relative densities observed in recent case studies (e.g. Abdrabbo & Gaaver, 2012; Royston et al., 2022b). Cone penetration testing demonstrated satisfactory sample repeatability and uniformity.

4.3.2 Lubrication and Grouting

To ensure complete hydration, the bentonite slurry and cementitious grout were thoroughly mixed using a high-shear bench-mounted stirrer at speeds incremented up to 2000 rpm. For both mixtures, water was first added to a bucket. With the stirrer running, the powdered dry components were gradually incorporated to achieve complete mixing. For the present testing,

Table 4.1: Leighton Buzzard 14/25 sand properties (Templeman, 2022).

Property	**Value**
Particle sizes, d_{10}, d_{30}, d_{50}, d_{60} (mm)	0.65, 0.77, 0.89, 0.95
Minimum dry unit weight, $\gamma_{d,min}$ (kN/m^3)	14.22
Maximum dry unit weight, $\gamma_{d,max}$ (kN/m^3)	17.00
Maximum void ratio, e_{max}	0.834
Minimum void ratio, e_{min}	0.566
Particle specific gravity, G_s	2.66
Critical state friction angle, ϕ_c (°)	33.2

TUNNEL-GEL® PLUS was used to produce the bentonite slurry, mixed using a typical ratio adopted in industry (1 l water : 62.5 g bentonite powder; Templeman, 2022). Once mixed, the slurry was left to stand for 24 hours to hydrate. During sinking, lubrication was injected at a constant rate of 650 g/min, accounting for penetration of lubricant into the sand (Phillips, 2023) and the rate of actuation during sinking (25 mm/min).

Following the sinking cycles, grout was injected into the lubricant-filled annulus under controlled pressure. A regulated pressurised airline was used to maintain injection at 1 bar. The grout mix used was 1 l water : 813 g cement : 125 g bentonite, which resulted in a density of 1430 kg/m^3; this mix was used on a recent project in Arklow, Ireland (Willis et al., 2023). Injecting grout into the annulus initially resulted in bentonite being displaced and emerging at the sand surface, followed by direct flow of grout to the surface (Figure 4.4). This behaviour matches on-site observations. Once a steady, uninterrupted flow of grout was observed at the sand surface, injection was stopped.

4.3.3 Testing Programme

In all tests, four sinking cycles were first carried out to form the annulus and ensure sufficiently large shearing occurred at the interface. The bentonite-filled annulus was established using the process illustrated in Figure 4.5 (test stage 1). During testing, the overcut was created by fitting 20 mm thick plywood 'overcut panels' to the concrete face during the initial cycles. As these progressed through the tank, the annulus was created in their wake. The panels were

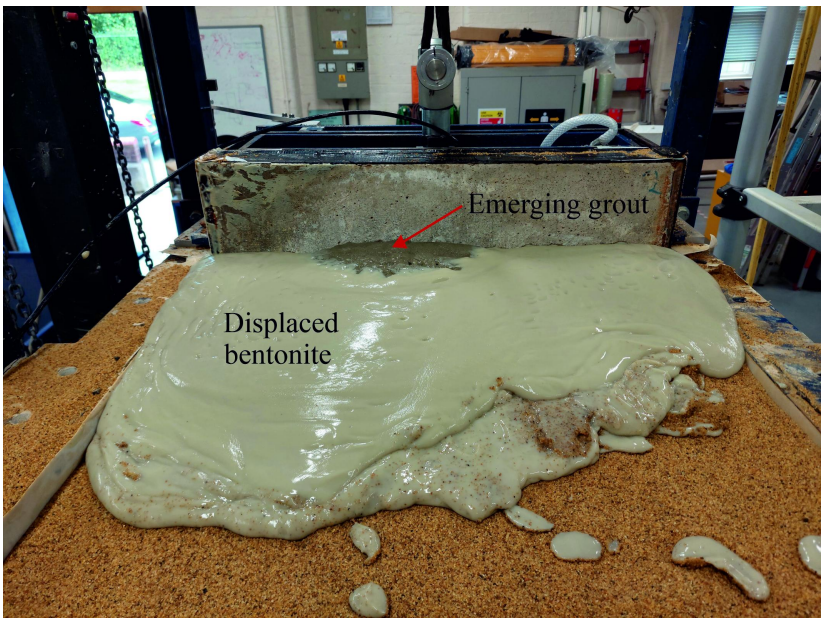


Figure 4.4: A photograph of the sand surface showing bentonite being displaced from the annulus due to grout injection, followed by the direct flow of grout to the surface.

removed from the TP once they passed the bottom of the tank before the bottom TP was detached and recycled to the top of the TP train. The 20 mm annulus thickness matches previous experimental studies which have successfully simulated full scale behaviour (Templeman, 2022; Phillips, 2023).

Bentonite was initially injected from the TP directly trailing the plywood panels (TP4). In cycle 3, lubrication was changed to TP2, since TP4 passed out of the tank. Whilst the annulus was fully formed after cycle 3, an additional sinking cycle was carried out to ensure full lubricant coverage. The rate of actuation during all sinking cycles was 25 mm/min, closely replicating sinking rates observed on site (Templeman, 2022).

Each test consisted of six stages (see Figures 4.5 and 4.6):

1. Four downward sinking cycles with annulus formation and lubricant injection.
2. A post-sinking stoppage (PSS).
3. Injection of grout.
4. A post-grouting stoppage (PGS).
5. Upwards actuation of the TPs, enabling measurement of frictional resistance in uplift.

6. Excavation of the tank, enabling retrospective qualitative observation of behaviour during testing.

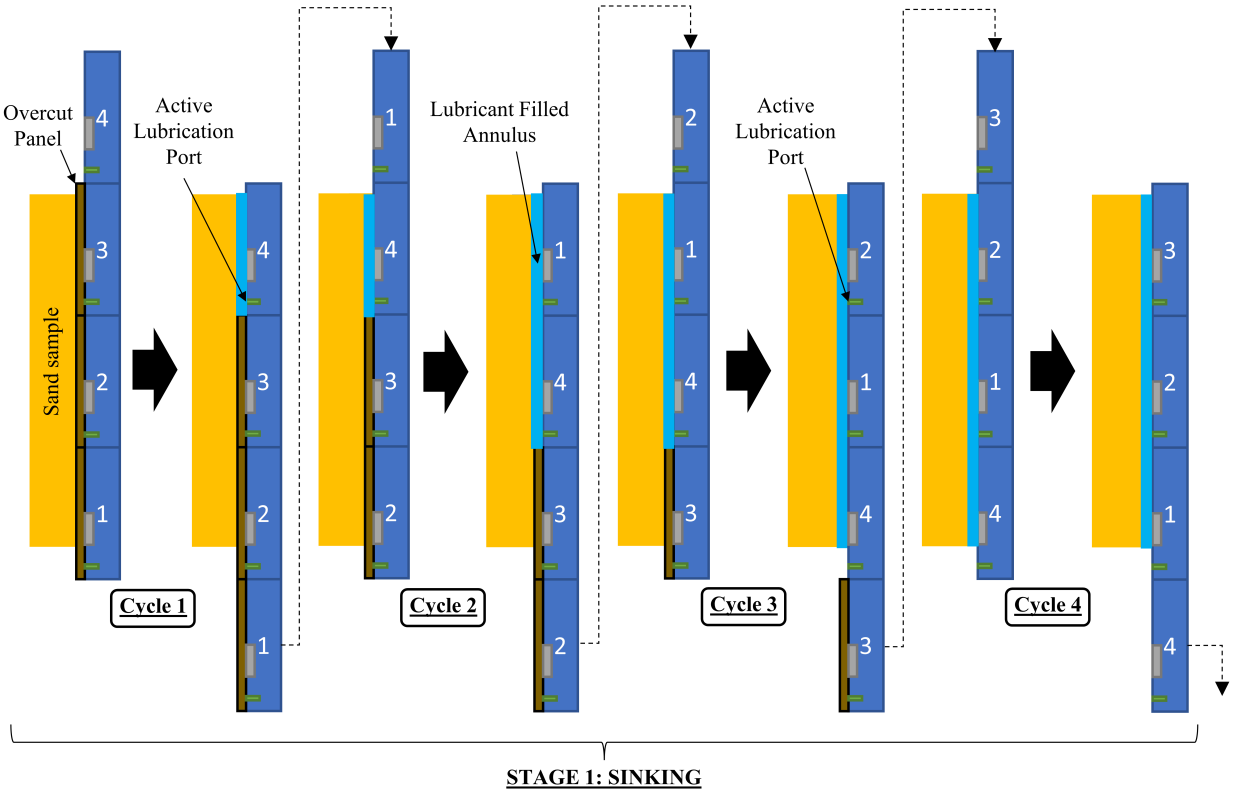


Figure 4.5: Schematics of a section through the testing apparatus demonstrating annulus formation during the four sinking cycles (test stage 1).

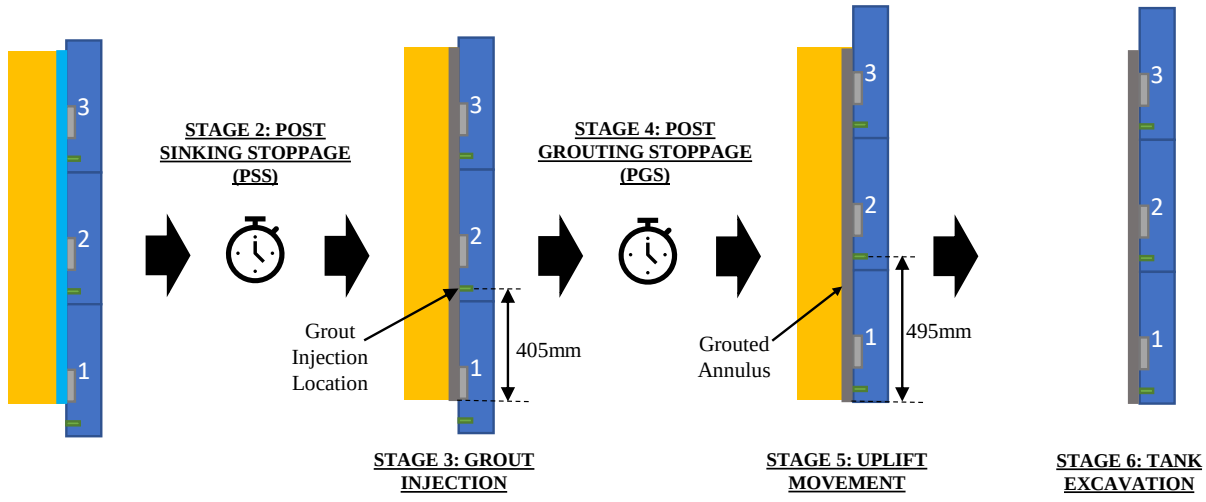


Figure 4.6: Schematics of a section through the testing apparatus demonstrating stages 2-6 of each test.

Table 4.2 summarises the testing programme where the primary parameters investigated are the respective lengths of the PSS (test stage 2) and the PGS (test stage 4). The PSS controls

Table 4.2: Summary of the testing programme and key parameters (PSS/PGS = post-sinking/grouting stoppage).

Stage	**(1)**		**(2)**		**(3)**		**(4)**		**(5)**		**(6)**
Test no. (PSS-PGS)	Sinking Cycles	→	PSS (Days)	→	Grout Injection Locations	→	PGS (Days)	→	Upwards Actuation Rate (mm/min)	→	Excavate Tank
1 (4-1)	4		4		2		1		1		
2 (1-20)	4	→	1	→	1	→	20	→	1	→	Excavate Tank
3 (0-1)	4		0*		1		1		1		
Baseline	4		1		0		N/A		1		

*1 hour

the age of the bentonite present in the annulus, which is expected to influence viscosity and thixotropy (see Section 2.5), both of which could impact grout injection behaviour and subsequent friction. On site, the age of the bentonite is a function of three factors: (i) the duration of sinking, which may be approximately 2 - 3 months for a large-diameter caisson (Royston et al., 2022b; Willis et al., 2023); (ii) the frequency of injection of fresh bentonite during sinking; and (iii) the time taken between completion of sinking and injection of grout (typically one day). Accounting for the complex range of on-site factors and practical constraints in the laboratory, three PSS lengths were considered: four days (Test 1), one day (Test 2), and one hour after sinking (Test 3).

Equivalently, the PGS represents the length of time between pumping grout into the annulus and the onset of flotation (i.e. when the caisson base is constructed). The PGS is typically one week on-site and dependent on several factors, such as the size of the caisson and whether the base is composed of reinforced or unreinforced (mass) concrete. Accounting for this variability, the influence of the PGS was explored by considering a likely lower bound case (one day) in Tests 1 and 3, and a likely upper bound case in Test 2 (20 days).

The sinking phase was identical for all tests. Grout injection was as described above for Tests 1 and 3. In Test 2, the internal grouting pipelines became blocked. In this case, grouting

was achieved by inserting a rigid hose into the annulus from the surface to closely replicate the injection procedure used in Tests 1 and 3. The author of this thesis is confident this different methodology did not influence subsequent results and observations. In Tests 2 and 3, grout was injected at only one location. In contrast, to explore the spacing of injection ports around the caisson circumference, injection was performed at two locations in Test 1.

The 'baseline' test involved no grouting. In this case, the bentonite lubrication was left in the annulus for one day prior to performing the uplift cycle. Comparisons to these baseline results enabled quantification of the relative increase in friction caused by the injection of grout. The rate of upwards actuation was chosen to imitate quasi-static conditions expected in the field, whilst working within the practical constraints of the present actuation system. ICE (2017) recommends a rate of approximately 0.02 mm/s (1.2 mm/min) for constant rate static load testing of piles. Under these considerations, a rate of 1 mm/min was implemented in all tests. In each case, the TPs were actuated upwards by a total displacement of 90 mm.

4.4 Modelling Assumptions and Scaling

The experiments presented in this chapter aim to model the construction process outlined in Section 2.3.1. Carefully designed experimental procedures were required to ensure faithful replication of caisson behaviour. Three key factors merit explicit consideration here:

1. Dry sand conditions were selected to tacitly model the behaviour of caissons constructed with effective dewatering (see Figure 2.2). This approach initially ensures faithful modelling of sinking and annulus formation. Following grout injection, the most critical design phase for caissons in uplift occurs immediately after base construction, before any subsequent internal structures have added weight. At this stage, dewatering will typically still be in place, making the modelling of uplift friction under dry conditions appropriate. Continued dewatering is not guaranteed to prevent the onset of uplift, justifying the present investigation of uplift friction during this critical design phase.

2. Whilst caisson profiles are typically circular, the 500 mm wide concrete face of the TP approximates the caisson-soil interface as plane-strain for these analyses. For a large diameter caisson with an OD of 35 m (Royston et al., 2022b), the centre point of a 500 mm section of caisson wall would only protrude into the sand sample 1.8 mm compared to

the flat TPs used in these experiments. Even for a relatively small diameter caisson, with an OD of 11 m (Royston, 2018), the equivalent value is 5.6 mm. These differences are smaller than typical construction tolerances in practice. Therefore, modelling the caisson wall in plane-strain is considered reasonable.

3. To faithfully simulate key aspects of caisson construction (including vertical annulus formation, large-displacement sinking, and grout injection over a large interface), this study employed a free sand surface at 1g. An important consideration when conducting experiments at low stress levels is that dilatancy suppression in sands under high pressures can lead to reduced peak friction angles (Bolton, 1986; 1987). This difference may affect the observed behaviour in the laboratory compared to deeper field conditions.

   To evaluate the applicability of the present experimental results, calculations are performed using the approach outlined in Bolton (1987). To consider any change in peak friction, a representative confining stress (p') is required. Following the precedent of Song & Sheil (2023), p' is taken as half the tank depth (experimental scale) or half the caisson depth (field scale). Using the unit weight of the sand sample ($\gamma_d = 16.1$ kN/m^3) and a coefficient of lateral earth pressure ($K_0 = 0.91$; Templeman, 2022), the confining stress at the tank half-depth (0.5 m) is calculated as $p' = 7.32$ kPa. Bolton (1987) specifies that no suppression of dilation is expected up to $p' = 150$ kPa. Therefore, equivalent behaviour could be expected up to a reference depth of 10.25 m in the field, corresponding to an overall shaft depth of 20.5 m. This depth is sufficient to capture behaviour down to the full depth of numerous caisson case studies documented in the literature (see Table 2.1).

   There is also substantial precedent in the literature demonstrating that low-stress 'laboratory floor' testing can reliably represent full-scale geotechnical phenomena, further validating the present modelling approach (e.g. Byrne & Houlsby, 2004; Kelly et al., 2006; Abadie et al., 2019; Richards et al., 2021; Song & Sheil, 2023). To ensure the risk of over-estimating friction is mitigated, a high displacement (90 mm) is employed during the uplift cycle, with the subsequent analysis in this thesis focusing on critical state friction to ensure a conservative bias.

4.5 Experimental Results

4.5.1 Frictional Resistance in Uplift

The friction that developed during the uplift cycles was determined from the top axial load cell (see Figure 4.3b). The raw measurements of actuation force for the four tests detailed in Table 4.2 are plotted in Figure 4.7. Also plotted are the results from an uplift movement conducted without a sand sample in the testing tank ('Empty Tank') and the weight of the TPs used during uplift movement ('TP Weight'). The 'Empty Tank' measurements capture both the weight of the TPs plus the rig's internal resistance, which was found to be low and consistent. The 'Baseline' test results are only marginally higher than the 'Empty Tank' results, indicating effective lubrication by the bentonite and minimal increase in internal resistance with a full tank.

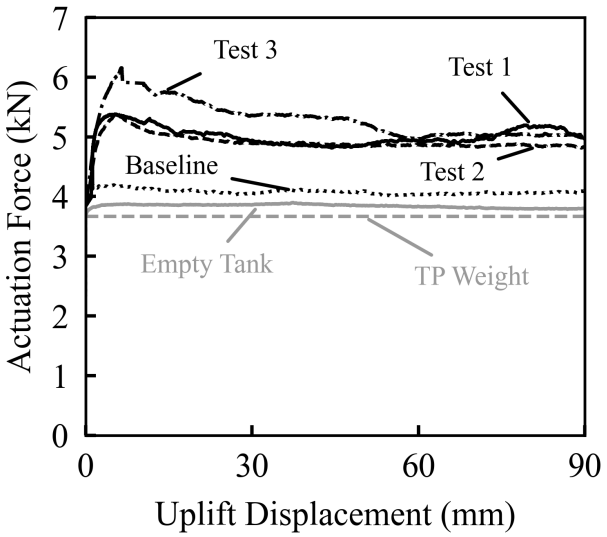


Figure 4.7: Actuation force during uplift for Test 1 (PSS = 4 days; PGS = 1 day), Test 2 (PSS = 1 day; PGS = 20 days), Test 3 (PSS = 1 hour; PGS = 1 day), and the Baseline test (PSS = 1 day; no grout). Also included for comparison: results from an uplift movement with no sand sample present (Empty Tank) and the weight of the TPs (TP Weight).

Total resistance at the interface for each test is the difference between the relevant test and the 'empty tank' line in Figure 4.7. These results are plotted in Figure 4.8. Tests 1-3 all show significantly increased resistance relative to the baseline test, demonstrating that post-lubrication grouting can effectively increase skin friction in resistance to uplift. All three tests present similar critical state friction, whilst Test 3 presented an apparently greater peak strength. It is suspected that the peak strengths in these tests were influenced by grout adher-

ence to the tank boundaries during initial actuation, further incentivising a focus on critical state friction in subsequent analysis.

Figure 4.8 suggests that both the PSS duration and the PGS duration have little influence on the uplift friction. In Test 1 the injected grout was allowed to set for 1 day, whilst 20 days were allowed in Test 2. Despite this, both tests show very similar friction results. This corresponds well with the findings of Lam et al. (2014), who found concrete strength to have little influence on interface friction during bored pile construction, albeit using polymer support fluids. The grout mixture used in the present testing had high cement content (≈ 600 kg/m^3). The present results suggest that grout strength does not play a significant role and there is therefore scope to use lower cement content in practice, reducing EC.

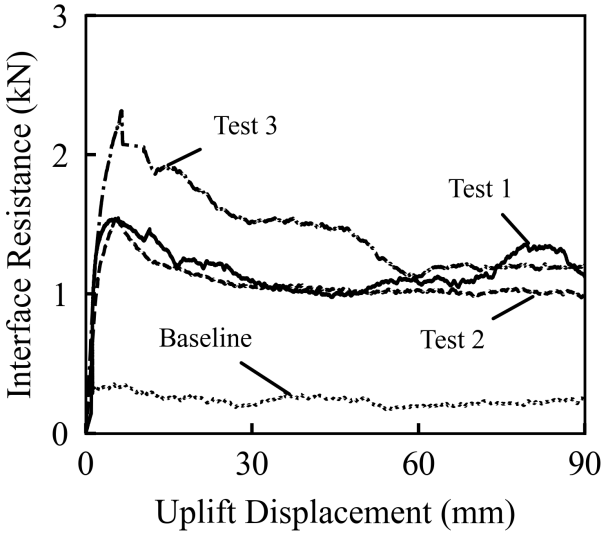


Figure 4.8: Total resistance at the interface during uplift for Test 1 (PSS = 4 days; PGS = 1 day), Test 2 (PSS = 1 day; PGS = 20 days), Test 3 (PSS = 1 hour; PGS = 1 day), and the Baseline Test (PSS = 1 day; no grout).

4.5.2 Visual Observations

To explore the mechanisms governing the measured friction, the sand sample was carefully excavated by hand, removing only loose and unbonded sand. Figure 4.9 presents initial observations from the three tests. In all cases, it appears infiltration of bentonite into the sand sample has led to the formation of a layer of self-supporting, cohered sand at the interface, commonly referred to as internal filter cake (see Section 2.5.2). In Tests 2 and 3, the excavation of the tank was carried out with the TPs maintained in their elevated position, providing evi-

dence that this layer of sand moved upwards with the TPs. This is demonstrated by the sand layer extending beyond the top of the tank, and the rupture of the sand layer at approximately half-tank depth (see Figures 4.9b and 4.9c). This implies the following failure mechanism: (i) the grout adheres to both the concrete face and filter cake; (ii) the concrete face, grout, and filter cake translate together in uplift, meaning that the failure plane occurs within the sand sample. This demonstrates a key benefit of the present test set-up, which allows unrestricted self-determination of the shear plane (in contrast to conventional direct shear apparatus, where the shear plane is confined to the plane between the two boxes). In the baseline test a similar filter cake formed. However, shearing occurred at the bentonite-concrete interface, so did not move with the TPs.



(a) Test 1 (4-1) (b) Test 2 (1-20) (c) Test 3 (0-1)

Figure 4.9: Photographs of the interface after initial excavation.

Figure 4.10 presents observations during the uplift movement in Test 2 where the formation of both internal and external filter cakes is evident. This behaviour is consistent with predictions in the literature for the present sand particle size distribution (d_{10} = 0.65 mm $\approx$ 1 mm; see Section 2.5.2). Whilst the internal filter cake was narrow near the surface (2-3 mm; Figure 4.10), it was measured to be much thicker near the tank base (30-35 mm), where higher surcharge pressures likely caused greater bentonite penetration into the sand. The external filter cake remained thin (1-3 mm) at all depths.

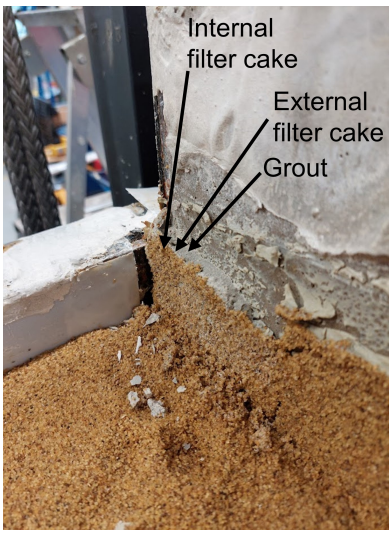
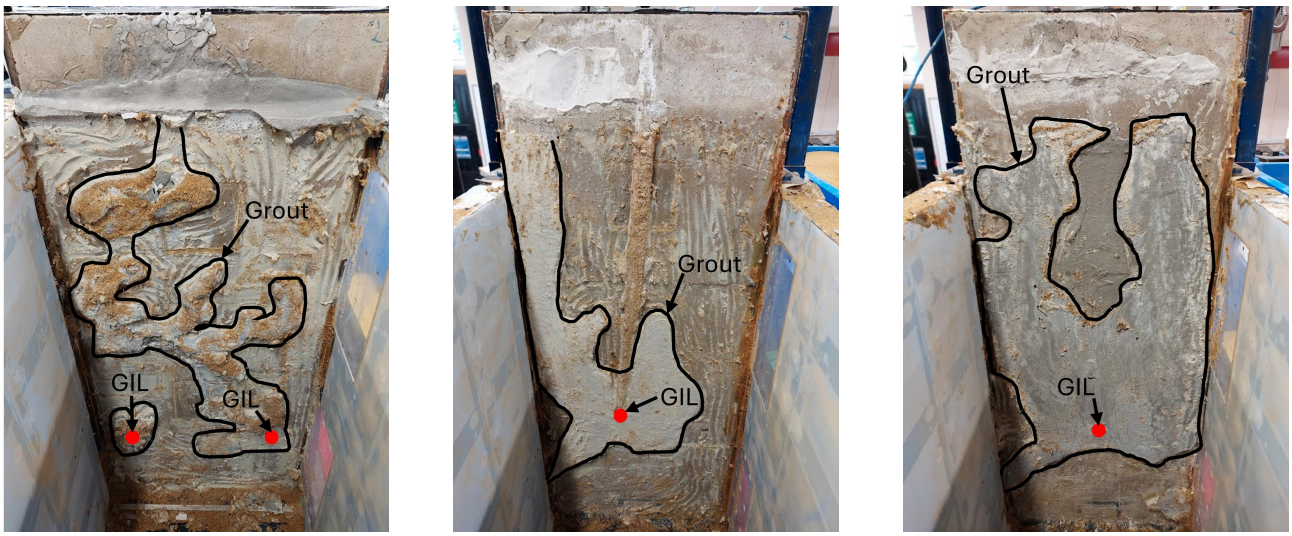


Figure 4.10: Photographs demonstrating the grout, filter cake, and sand layer translating with the TP at the sand surface during Test 2.

4.5.3 Grout Injection Behaviour

Following the initial excavation, all remaining sand and bentonite was carefully removed from the interface, leaving only the grout exposed. The exposed grout was observed to be relatively smooth, indicating that the grout did not penetrate the filter cake or sand. Photographs in this state are presented for all three tests in Figure 4.11. The spread of grout can be seen to vary significantly between tests, demonstrating that the PSS duration had a significant impact on the spread of grout at the interface. This can be seen by comparing the greatest grout coverage in Test 3 (PSS = 0 days), the intermediary coverage in Test 2 (PSS = 1 day), and lowest coverage in Test 1 (PSS = 4 days). This behaviour is likely driven by thixotropy and/or bentonite water loss, resulting in an increase in viscosity (see Section 2.5.2). Under these circumstances, the dispersion of grout appears to be governed by VF (see Section 2.5.3).

Samples of bentonite obtained during excavation were weighed, dried, and re-weighed to determine the water content (Table 4.3). These samples were taken from the bentonite closest to the grout injection location (GIL). No sample was obtained for Test 3. As expected, the water-to-bentonite ratio decreases with increased filtration time, corroborating the anticipated increase in viscosity. Insufficient quantities of bentonite were obtained from the interface to enable rheological testing, and no suitable methods for predicting viscosity in the annulus are available in the literature (Praetorius & Schößer, 2017). Consequently, further analysis of the



(a) Test 1 (4-1) (b) Test 2 (1-20) (c) Test 3 (0-1)

Figure 4.11: Photographs of the interface after further excavation of the sand and bentonite. For each test, the following are indicated: the spread of grout in the annulus, and the grout injection location(s) (GIL).

relative viscosity of the grout and bentonite is beyond the scope of this chapter. The grout injection process is instead isolated and studied in detail in Chapter 5.

Table 4.3: Water content of the bentonite samples obtained at the end of each test. Sample taken from the interface near the grout injection location. No result was obtained for Test 3.

Test	**Filtration Time (= PSS)**	**Water : Bentonite Ratio**
Test 1	4 days	10.0 : 1
Test 2	1 day	13.2 : 1
Test 3	6 hours	-
All	Fresh bentonite mix	16.0 : 1

The circles in Figure 4.11, labelled GIL, show where grout was injected in each test. In Test 1, grout was injected from two locations, both supplied by the same pressure vessel. Figure 4.11a shows that grout infiltration ceased from the left port soon after the commencement of injection, suggesting the grout encountered less resistance exiting the right port. This has significant implications for site practices where there are typically multiple injection locations around the caisson circumference, all supplied from the same feed. To ensure effective grout distribution, injection at each port should be controlled independently.

4.5.4 Failure Mechanism

Whilst grout coverage varied significantly across the three tests (Figure 4.11), the translation of a sand layer with the TP (Figure 4.9) and the resulting friction remained consistent (Figure 4.8). These findings suggest that the same failure mechanism (where the caisson wall, the grout, remaining lubricant, and filter cake move as a single block) develops for both 'poor grout coverage' (Test 1) and 'good grout coverage' (Test 3) in the present tests (Figure 4.12). These results instil confidence that, under the present conditions, full friction can be mobilised even with imperfect grout coverage. However, there is likely a threshold for how 'poor' grout coverage can be whilst still enabling the same failure mechanism. Therefore, efforts should still be made to ensure uniform grout distribution.

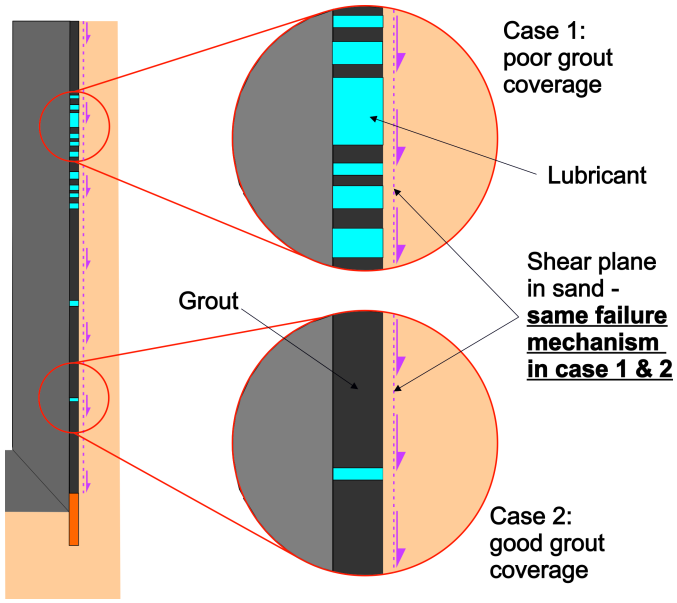


Figure 4.12: A schematic illustration of the proposed failure mechanism, which is the same for both 'poor' and 'good' grout coverage.

4.6 Limitations

The present testing was carried out using dense coarse sand in dry conditions. Caution should be exercised when applying these results to other conditions. In particular, the observed failure mechanism relied on the formation of an internal filter cake. In finer-grained soils, such a filter cake is unlikely to develop (see Section 2.5.2). Consequently, the layer of self-supporting, cohered sand at the interface is also unlikely to form. Under these conditions, the failure plane may instead occur at the grout-external filter cake boundary, making the maximisation of grout

coverage a critical priority.

4.7 Summary

This chapter introduced the experimental apparatus used to investigate the development of skin friction on caissons subjected to uplift forces. Four experimental tests were described, demonstrating that grout injection after sinking can lead to an effective increase in friction.

The first factor considered in the testing was the influence of the age of the bentonite on the injection of grout. Older, more viscous bentonite was shown to lead to less effective spread of grout. Experimental observations indicated that injection at each grouting port should be controlled independently to ensure the effective spread of grout. Whilst the spread of grout was shown to vary considerably, the resulting failure mechanism and friction were both relatively consistent. This suggests that although ensuring an effective spread of grout is important, there can be high confidence in the development of skin friction even if 'perfect' grout coverage is not achieved.

The second factor investigated was the influence of the length of time between injecting grout and the onset of uplift (controlling the grout strength). This duration was demonstrated to have little impact on skin friction; the same failure mechanism was observed to occur irrespective of grout age. This has positive implications: (i) the caisson base can be poured as soon as possible after grouting without concern of lower skin friction; and (ii) the cement content of the grout can be decreased.

The bentonite lubrication was observed to form an internal (up to 35 mm) and external filter cake (up to 3 mm). The internal filter cake formation enabled the observed failure mechanism, where the caisson wall, the grout, any remaining lubricant, and filter cake move together as a block. This resulted in the shear failure plane occurring in the sand. This demonstrated a key benefit of the present test set-up, which allows unrestricted self-determination of the shear plane (in contrast to conventional direct shear apparatus, where the shear plane is confined to the plane between the two boxes).

In cases of poor grout coverage, it is suspected that VF is the underlying cause. Observation of this phenomenon was facilitated by the relatively large scale of the apparatus, highlighting another key advantage of the present test set-up compared to more traditional element-scale

testing. It is suspected that: (i) the observed failure mechanism may not occur in other soil types; and (ii) even in coarse sand, there is likely a threshold for how 'poor' grout coverage can be whilst still enabling the same failure mechanism. Therefore, maximising grout spread remains a critical priority. To address this, the grout injection process is examined in greater detail in the next chapter.

5 Laboratory Testing on Grout Injection into Bentonite-Filled Annuli

5.1 Introduction

Evidence presented in Chapter 4 confirmed concerns that VF may lead to non-uniform grout coverage (see Figure 4.11). Analysis of grout spread in those experiments was limited by two factors: (1) the inability to predict or measure the viscosity of bentonite in the annulus; and (2) the inability to observe the grout injection process. This chapter addresses these limitations by presenting experimental results obtained using a bespoke apparatus designed to isolate and observe the grout injection process. The experiments aim to elucidate the influence of two key factors: bentonite viscosity and thixotropy. Rheological testing of the bentonite and grout is also undertaken to provide context to the results. The experiments in this chapter were conducted at the University of Cambridge during the author's tenure as a visiting researcher.

5.2 Laboratory Apparatus

Figures 5.1 and 5.2 present the key features of the new experimental apparatus, which was developed to enable the simulation and observation of grout injection into an annulus. The apparatus consists of a 25 mm thick aluminium plate and a 80 mm thick acrylic sheet, which are parallel to one another and separated using an 25 mm thick aluminium spacer, creating an 800 mm × 800 mm × 25 mm internal void (see Figures 5.1b and 5.2b). A sacrificial 5 mm acrylic sheet is positioned internally to protect the primary acrylic window, reducing the void depth from 25 mm to 20 mm (see Figure 5.1b). When filled with bentonite, the void represents a planar approximation of an annulus; an assumption justified in Section 4.4. For clarity and consistency with Chapter 4, the term 'annulus' is used throughout this chapter.

The internal void dimensions were selected to ensure close replication of field conditions whilst minimising boundary effects. A void depth of 20 mm was used, consistent with Chapter 4, as a compromise between typical field-scale annuli (50–100 mm; Templeman, 2022) and practical laboratory constraints, such as the volume of lubricant required for each test. The

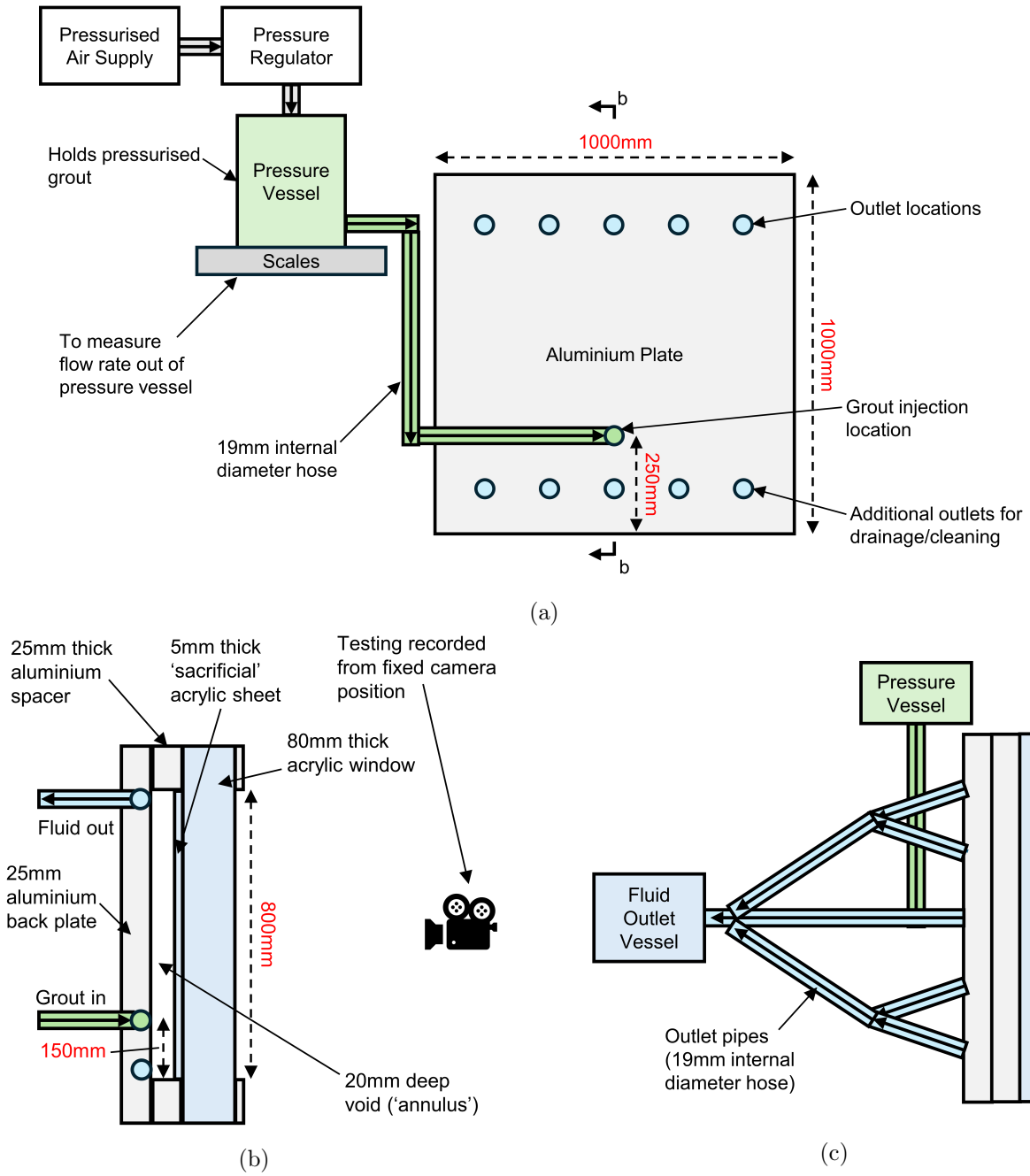
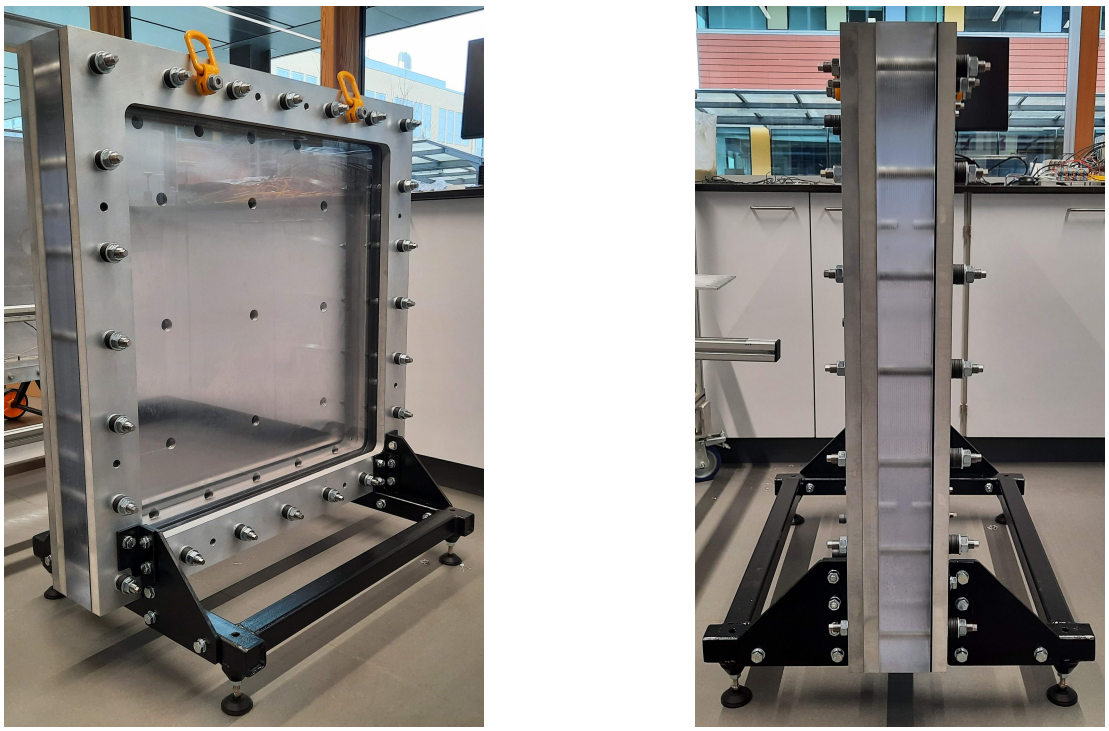


Figure 5.1: Simplified schematic illustrations of the testing apparatus indicating key features: (a) a rear elevation view depicting the grout injection system; (b) a section view (b-b) showing the 800 mm x 800 mm x 20 mm void used to imitate the annulus; and (c) a plan view demonstrating the fluid outlet arrangement. Not to scale.

overall apparatus dimensions (800 mm × 800 mm) were chosen to ensure boundary effects did not influence the results. The setup is analogous to a Hele-Shaw cell, where the width and length must be significantly greater than the void thickness to allow VF behaviour to develop independently of boundary interference (Tanveer, 2000). The selected width-to-depth ratio of 20 falls within the range used successfully in previous VF studies (e.g. Lindner et al., 2000; Lindner et al., 2002). This requirement for a sufficiently high width-to-depth ratio constrained



(a) (b)

Figure 5.2: Photographs of the testing tank, excluding pipework: (a) a diagonal view; and (b) a side view.

the maximum void depth, as a deeper void would have required a proportionally larger tank, which would be impractically large and risk bending of the acrylic sheet.

During testing, the void is filled with bentonite, before grout is injected under pressure via 19 mm ID ports in the aluminium back plate, which represents the caisson wall in practice. The acrylic window is positioned where soil would be expected. Testing in Chapter 4 revealed that grout infiltration into the soil is unlikely, even in coarse grained soils with high permeability. As such, the acrylic is not expected to alter the grouting behaviour. The spread of grout is visually monitored through the acrylic window, as shown in Figure 5.1b. To enable upward displacement of bentonite during grout injection, as observed in the field and Chapter 4 (Figure 4.4), five fluid outlet locations were incorporated at the top of the tank (Figure 5.1). These outlets connect to an open-top outlet vessel, which is positioned at the same level to prevent syphoning effects (Figure 5.1b and 5.1c). The outlet pipelines were carefully arranged to ensure equal hydraulic resistance across all five potential flow paths, minimising the formation of unrealistic preferential flow patterns during testing (Figure 5.1c). Additional outlets are provided at the bottom of the tank to facilitate cleaning and drainage after testing (Figure 5.1a). Ball valves were fitted to all inlets and outlets to enable independent flow control.

5.3 Experimental Methodology

5.3.1 Bentonite Slurry and Grout Preparation

The bentonite slurry and grout were mixed using the same methodology outlined in Section 4.3.2. The bentonite was made using TUNNEL-GEL® PLUS at two different mix ratios, as detailed in Table 5.1. Note that the ratio is quoted as the fraction of water to bentonite, such that 12:1 indicates a higher bentonite concentration than 16:1. The 16:1 matches the slurry used in Chapter 4, which represents a typical mix in industry (Templeman, 2022). The 12:1 mix produces a thicker, more viscous bentonite and is used as a proxy for consolidated bentonite in the field, which will have become more viscous due to water loss into the surrounding soil. The 12:1 mix was selected as a compromise, balancing the most viscous 10:1 ratio achieved in Test 1 in Chapter 4 (Table 4.3) with the requirement for sufficiently low viscosity to ensure smooth flow through the pipes during testing. Table 5.1 also details the grout mixture used in all the present tests, which also matches Chapter 4.

Table 5.1: Bentonite and grout mixtures used during testing (expressed per litre of water).

Mixture	**Water (L)**	**Bentonite (g)**	**Cement (g)**	**Density (kg/m^3)**
Baseline Bentonite Slurry (16:1)	1	63	N/A	1040
High Viscosity Bentonite Slurry (12:1)	1	83	N/A	1050
Grout	1	125	813	1430

5.3.2 Rheological Testing

Density and viscosity are the key properties which govern the stability of the injection of one fluid into another (see Section 2.5.3). To measure density, a cylindrical container of a known volume was filled with the fluid, levelled off, and its mass was measured. The measured densities of the fluids are given in Table 5.1. Viscosity for each fluid was calculated as a function of shear rate using an Anton Paar RheolabQC rotational rheometer fitted with a CC27 measuring system. For each sample of bentonite slurry and grout, a standard test was carried out, measuring the variation in shear stress (τ) for a linearly increasing shear rate ($\dot{\gamma}$)

from 1 to 100 s^{-1}. Viscosity (μ) can be subsequently calculated using the relationship $\mu = \tau/\dot{\gamma}$.

5.3.3 Main Test Procedure

Each test consists of four stages:

1. The bentonite slurry is prepared and the pressure vessel is filled (see Figure 5.1a). A low pressure is applied to fill the apparatus with bentonite via the grout injection hose (replicating on-site methodology, where the same pipelines are used for bentonite lubricant and grout injection). This process proceeds until all air is removed from the system and bentonite is flowing into the fluid outlet vessel (see Figure 5.1c).

2. The bentonite is left to rest for a pre-determined time (varies between tests), with both the inlet and the outlets left open. The pressure vessel is positioned at the same height as the outlets (see Figure 5.1a), enabling replication of hydrostatic pressure in the annulus; see Figure 2.7).

3. The grout mixture is prepared. Removing any remaining bentonite first, the pressure vessel is filled with the grout. Any remaining bentonite in the grout injection hose is left in-situ, replicating on-site conditions.

4. Grout is injected into the bentonite-filled annulus at a fixed pressure of 1 bar, controlled using an automatic digital pressure regulator. The mass flow rate of the grout is logged using scales supporting the pressure vessel (see Figure 5.1a) and the spread of grout is recorded using a video camera, which is aligned with the centre of the tank window to minimise distortion (Figure 5.1b). Grout is injected until it reaches the top of the tank, boundary effects are observed, or the pressure vessel is empty.

5.3.4 Image Processing

To analyse each test video, Python programming was used to identify the proportion of the tank filled with grout. The program first crops the video to only the central viewing window which is then divided into an 800 × 800 pixel grid. As this central portion of the tank is 800 mm by 800 mm, one square pixel is equivalent to one square millimetre. An initial frame is used to normalise the subsequent video frames, aiding in the correction of errors

in the raw images (e.g. reflections). Three manual inputs are required: (i) the time grout injection commenced; (ii) the desired sampling rate; and (iii) the desired number of frames. A representative sample of 40-50 frames was taken for each test, with the sampling rate and number of frames adjusted depending on the duration of grout injection. For each sampled frame, the programme identifies the injected fluid from the normalised image using the 'Source Extraction and Photometry' library (Bertin & Arnouts, 1996; Barbery, 2016). Since the grout is consistently darker than the bentonite, the pixels in which grout is present can be identified and returned as a segmentation map. The image is represented by an 800 x 800 array, where the pixels identified as grout are denoted with a value of 1, and the remaining bentonite pixels are denoted with a value of 0. The area of the grout can subsequently be calculated by the sum of the array elements.

5.3.5 Testing Programme

Five tests were carried out, as detailed in the test schedule in Table 5.2. Two main variables were tested: (i) the bentonite mixture ratio, and (ii) the length of time for which the bentonite was left in the tank before grout was injected (i.e. the 'rest time'). Varying the bentonite mixture allowed the influence of bentonite viscosity on grout injection to be explored, whilst adjusting the rest time was used to assess the influence of thixotropy. Test 1 is considered the baseline test, involving a 16:1 bentonite mix and one hour rest time.

Table 5.2: Grout injection testing programme.

Test Number	**Bentonite Mixture**	**Rest Time**
1	Baseline (16:1)	1 hr
2	Baseline (16:1)	40 hrs
3	Baseline (16:1)	18 days
4	High Viscosity (12:1)	1 hr
5	High Viscosity (12:1)	40 hrs

5.4 Modelling Assumptions: Boundary Conditions

Although the apparatus dimensions were carefully selected to minimise boundary effects on VF behaviour (see Section 5.2), other aspects of the imposed boundary conditions influence the applicability of the results to field conditions and therefore merit explicit consideration. In the present setup, the bottom and side boundaries are fixed, whilst the open ports at the top approximate a free boundary. The influence of each boundary condition is considered in turn below:

Fixed Bottom Boundary: This boundary condition closely replicates field conditions, where the injection point is typically located near the base of the annulus and the cutting shoe prevents downward grout displacement (see Figure 2.2).

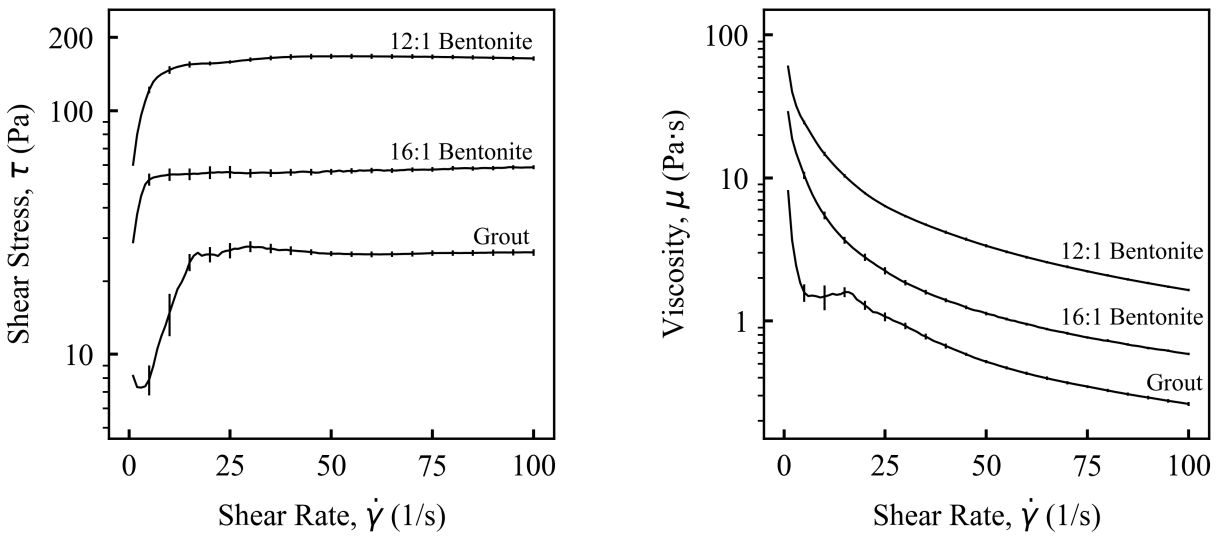
Free Top Boundary: The ports at the top of the tank allow bentonite outflow during grout injection, approximating the free-surface outflow at ground level typically observed in the annulus on-site (see Figures 2.7 and 4.4).

Fixed Side Boundaries: This boundary condition implies that the vertical edges of the tank act as lines of symmetry, effectively modelling simultaneous and identical grout injection from ports located 800 mm to either side of the actual injection point. To model injection from a single isolated port, outflow ports could also be introduced at the tank sides in future experiments. In practice, injection may occur either simultaneously or independently in sequence through ports around the caisson. The experiments in this chapter focus on simultaneous injection, as this remains the more common industry approach and is more likely to lead to the critical undesired outcome of limited lateral grout spread.

5.5 Rheological Test Results

To ensure repeatability, the rheology of four samples of each fluid, prepared from distinct batches, was tested. The averaged shear stress measurements and inferred viscosity results are presented in Figures 5.3a and 5.3b, respectively. Error bars denote the standard error of the mean at intervals of $\dot{\gamma} = 5\ \mathrm{s}^{-1}$. The testing confirms the expected shear-thinning behaviour of both the bentonite and grout. The grout is less viscous than the bentonite mixtures, confirming the potential risk of VF during grout injection.

Both bentonite mixtures exhibit a smooth relationship between shear rate and viscosity, with small error bars indicating good sample repeatability (see Figure 5.3b). The grout shows similar behaviour at high shear stresses (> 20 s^{-1}), but a more irregular relationship at low shear stresses (< 20 s^{-1}), with larger standard errors. It is suspected that the high cement content of the grout mixture may have affected the rheometer's performance. At the start of rheometer testing (at low shear rates), it is hypothesised that cement particles within the grout settle, causing the rheometer testing interface to be lubricated by a lower viscosity fluid than the fully mixed grout. This leads to the observed low initial shear stresses. As the shear rate increases, the grout mixture remixes, returning to homogeneous shear-thinning behaviour. Consequently, the viscosity measurements obtained for the grout under low shear stress conditions may not accurately reflect its behaviour during field or laboratory injection. Despite this limitation, the results were deemed sufficient to capture the relevant behaviour for subsequent analysis in this thesis. Alternative methods for measuring viscosity should be considered in future testing.



(a) (b)

Figure 5.3: The variation of (a) shear stress, and (b) viscosity as a function of shear rate for the baseline bentonite mixture (16:1), the high viscosity bentonite mixture (12:1), and the grout mixture. The error bars indicate the standard error of the mean at intervals of $\dot{\gamma} = 5$s^{-1}.

5.6 Grout Injection Test Results

5.6.1 Grout Progression

Grout was injected into the tank at a fixed pressure, resulting in varying flow rates across the five tests. Each test exhibited a relatively stable flow rate throughout its duration. The average flow rate for each test is given in Table 5.3. The variation in flow rates is largely due to the differing bentonite viscosities. Tests 1-3, which used 16:1 bentonite, all show relatively similar flow rates, whilst lower flow rates were measured in Tests 4 and 5 due to the higher viscosity (12:1) bentonite.

Table 5.3: Averaged mass and volume flow rates for the injection of grout in each test.

Test Number	**Bentonite Mixture**	**Rest Time**	**Mass Flow Rate, $\dot{m}$ (g/s)**	**Volume Flow Rate, Q (L/s)**
1	16:1	1 hr	222	0.155
2	16:1	40 hrs	296	0.207
3	16:1	18 days	203	0.142
4	12:1	1 hr	8	0.006
5	12:1	40 hrs	72	0.050

Figure 5.4 presents exemplar results from the baseline test (Test 1) midway through the test (Figure 5.4a) and at the end of the test (Figure 5.4b). Both raw and processed images are presented showing effective identification of the grouted area throughout testing. Figure 5.5 presents processed images at four equally spaced time intervals for each test. The duration of grout injection differed between different tests; therefore, the time intervals are normalised by the overall length of the relevant test (T). Figure 5.5 suggests the approximate profile of the grout is defined early during injection, with the profile scaling proportionally for the rest of injection. This suggests ensuring good grout coverage may be achieved by ensuring stability of the system at the onset of grout injection.

Comparing tests with a fixed rest time of 1 hour (Tests 1 and 4, Figures 5.5a and 5.5d) indicates that a higher viscosity bentonite (12:1) results in less uniform grout distribution. Analysis of the tests with a fixed resting time of 40 hours (Tests 2 and 5, Figures 5.5b and 5.5e) confirms this trend, revealing an even more pronounced deterioration in grout coverage. These

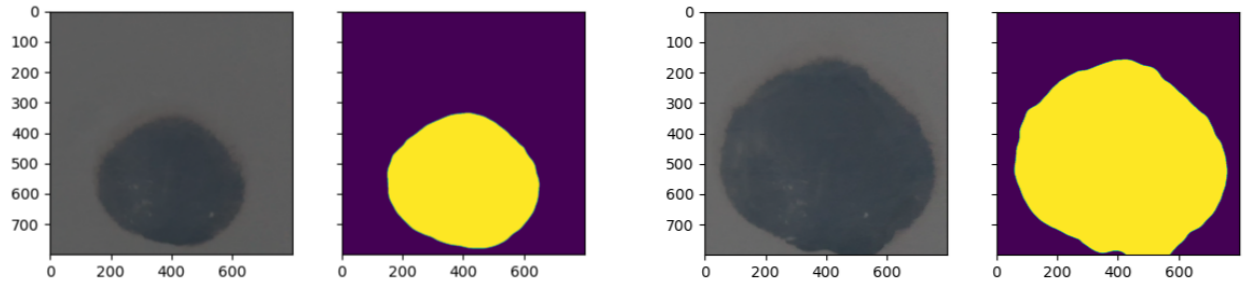


Figure 5.4: Grout injection results for Test 1 (16:1 bentonite, rest time 1 hour): (a) halfway through grout injection; (b) at the end of grout injection. The left images present greyscale images, as captured by the camera during testing. The right images present the processed images, where the grout is indicated by yellow and the bentonite by purple. Axis units mm.

two comparisons indicate increasing the bentonite viscosity leads to a decrease in the lateral spread of the grout. This poses a significant risk in caisson construction, where sections of the annulus in between grout injection locations may remain 'ungrouted', reducing overall friction with the surrounding soil in uplift.

The second factor explored during testing was the effect of thixotropy, which was explored by varying the rest time. This can first be assessed by comparing Tests 1-3, which used 16:1 bentonite with rest times of 1 hour, 40 hours, and 18 days, respectively (Figures 5.5a, 5.5b, and 5.5c). Relatively good spread of grout was observed in all three cases, with a slight decrease in the lateral extent of coverage in Test 3, which had a longer rest time of 18 days. Comparing Tests 4 and 5 (Figures 5.5d and 5.5e), which used the higher viscosity 12:1 bentonite with rest times of 1 and 40 hours respectively, a more significant deterioration in grout spread is observed with increasing rest time. However, this behaviour may have also been influenced by the higher injection rate in Test 5 (see Table 5.3). Increased rest time appears to decrease the local stability of the interface between the grout and bentonite, demonstrated by the development of more irregular grout profiles for longer rest times in all cases.

The variation in VF behaviour observed across the five tests suggests that boundary effects were effectively minimised by the apparatus design. The extensive lateral grout spread in Test 1, where VF was well controlled, indicates that good grout coverage can be achieved with simultaneous injection from adjacent ports around the caisson (as assumed in these experiments; see Section 5.4).

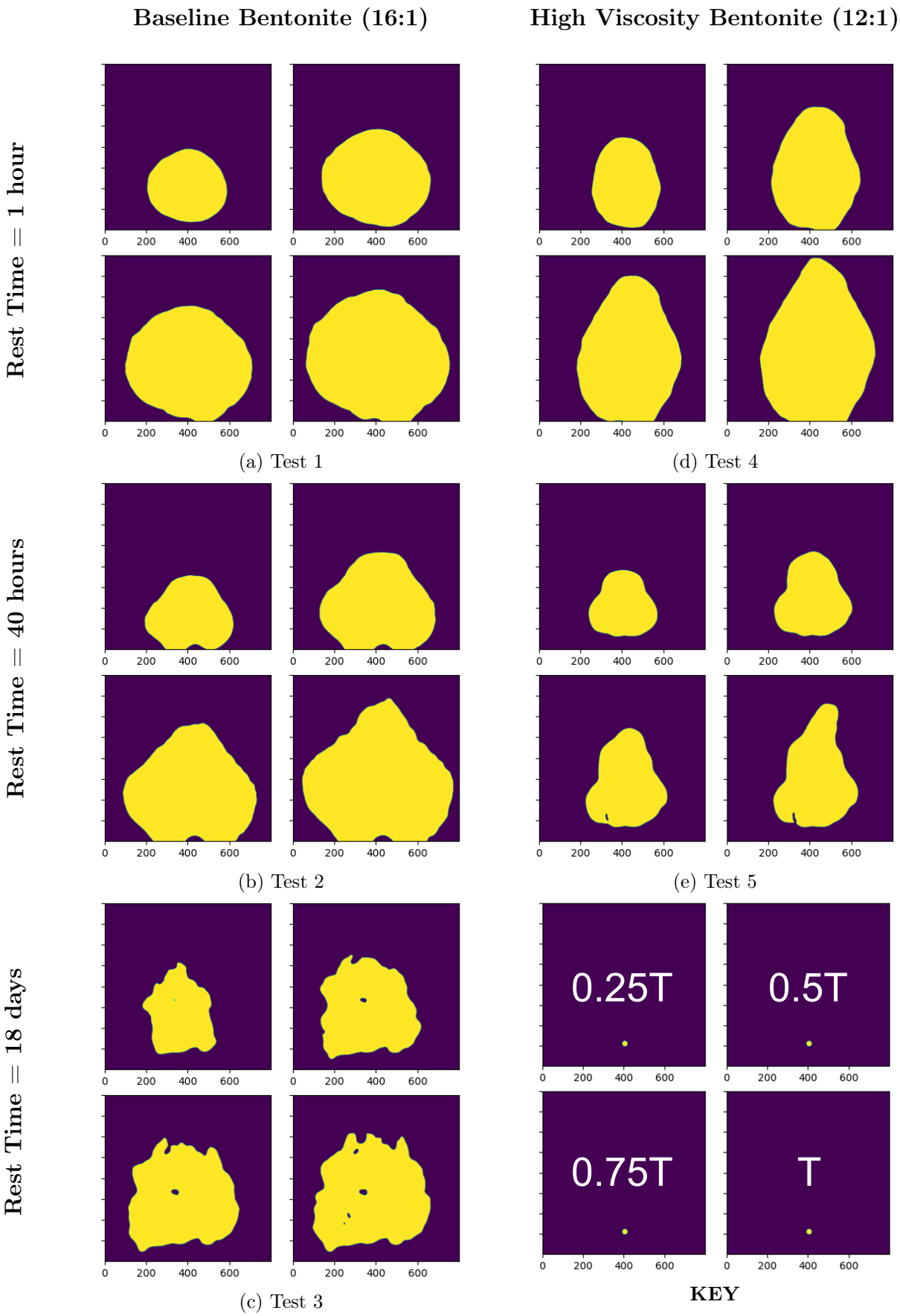


Figure 5.5: Processed images throughout grout injection for Tests 1-5. Images presented at normalized time intervals of 0.25T, where T is the total injection time for the relevant test. Axis units in mm.

5.6.2 Ellipticity Results

Ellipticity is used in this section as a metric to compare the uniformity of the injected shape and hence the stability of the system. Figure 5.6 uses the final grout profile of Test 5 as an example to demonstrate how ellipticity is calculated. Firstly, the maximum spatial dispersion of the grout profile along any direction is identified (with the two extrema denoted x_1 and x_2). This is used to define the orientation and length of the major axis. Coordinates are defined such that the x-axis is parallel to the major axis, which has length $L_{major} = x_2 - x_1$. The y-axis is subsequently defined perpendicular to the x-axis, and the two most distal points on the grout profile in this direction are defined as y_1 and y_2, giving the minor axis length $L_{minor} = y_2 - y_1$. Ellipticity is then calculated using Equation 5.1, such that $E = 0$ corresponds to a perfectly circular profile and a value of $E = 1$ denotes a straight line.

$$E = 1 - \frac{L_{minor}}{L_{major}}, \tag{5.1}$$

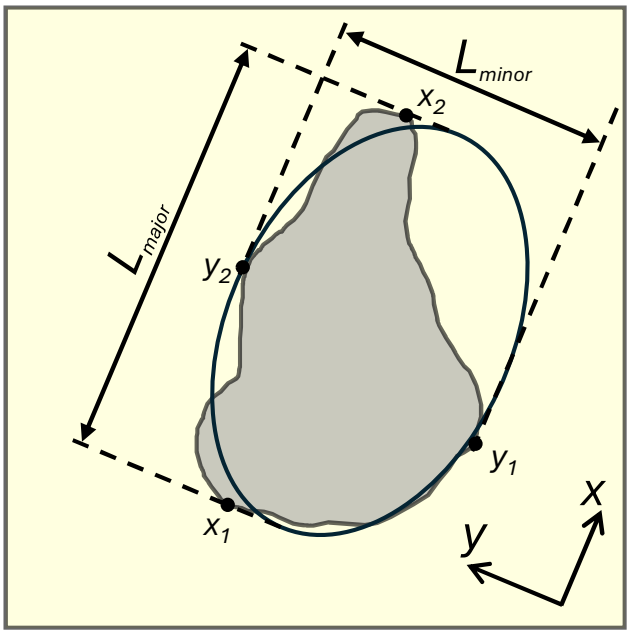


Figure 5.6: A schematic illustration showing the final grout profile of Test 5, with an ellipse overlaid along with the coordinate system used to define ellipticity.

Figure 5.7 presents the development of ellipticity as a function of the calculated grout area as injection progressed during each test. Tests 1 and 2, characterised by low ellipticity values and large grout areas, demonstrate the best grout spread, corroborating the qualitative observations in Figures 5.5. The results also confirm that viscosity has the greatest influence on the uniformity of grout distribution, with Tests 4 and 5 (12:1 bentonite) yielding the largest ellipticity at the end of testing. Considering Test 4, the results show a smooth increase in ellipticity as injection progresses, effectively demonstrating that without thixotropic effects, higher viscosity bentonite leads to limited horizontal grout dispersion, even with apparently stable vertical displacement (see Figure 5.5d). Ellipticity in Test 5 was initially lower than in Test 4, but then increased sharply due to the formation of a "finger" (Figure 5.5e), which ultimately led to a much lower final area. Tests 2 and 3, which used 16:1 bentonite with rest times of 40 hours and 18 days respectively, both experienced an initial increase in ellipticity followed by a decrease, suggesting thixotropy may only have a transient effect on the stability of grout injection.

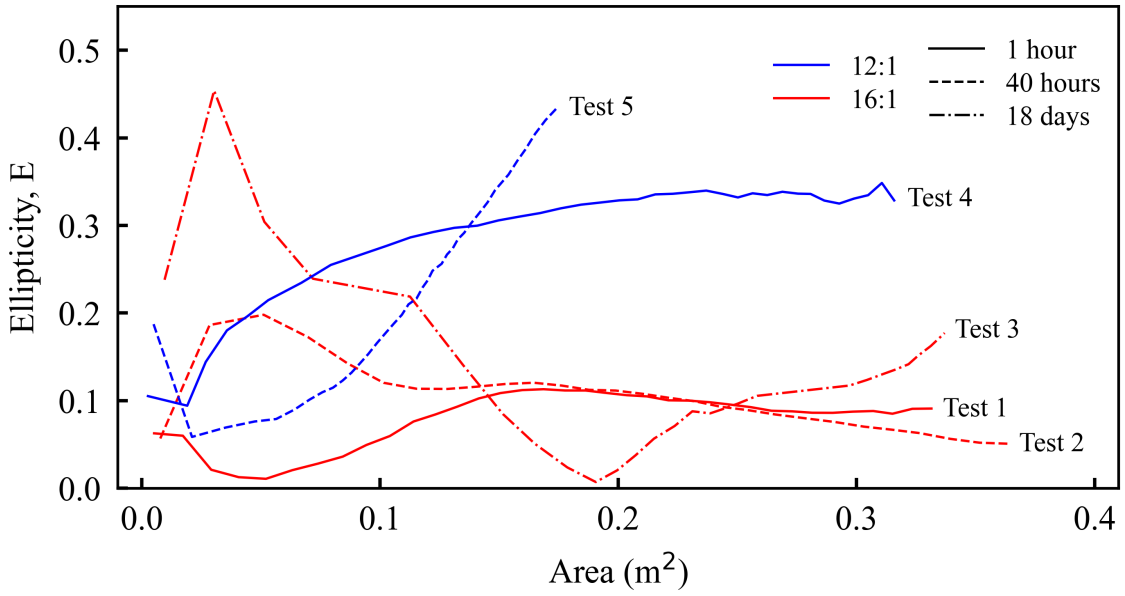


Figure 5.7: Ellipticity of the grout profile plotted against total grouted area as injection progressed for all five tests.

5.7 Summary

This chapter presented the key features of a novel apparatus developed to enable the observation of the injection of cementitious grout into a bentonite-filled annulus during caisson construction. Five tests were undertaken to explore the influence of bentonite viscosity and thixotropy on the grout injection process and the likelihood of encountering VF issues. The spread of grout was tracked using image processing techniques.

Observations demonstrated a strong correlation between increased bentonite viscosity and reduced grout coverage. Increased viscosity particularly limited the lateral spread of the grout. The impact of thixotropy was less pronounced, manifesting primarily in localised instabilities and irregular grout profiles. Ellipticity of the grout profile was demonstrated to be an effective metric for quantifying the uniformity of grout spread. These results, combined with the qualitative observations, suggest the influence of thixotropy is transient and only serves to make the grout profile more irregularly shaped, with limited impact on the final grouted area.

6 Numerical Modelling of Under-Reamed Caissons in Sands

6.1 Introduction

Sheil et al. (2024) introduced a design method for under-reamed caissons in undrained soil. However, no studies have considered drained conditions. This chapter seeks to fill this gap by describing results from a suite of finite-element analysis (FEA) calculations. A novel workaround is developed using Python and the PLAXIS Remote Scripting Interface, enabling straightforward implementation of adaptive remeshing (AR) in PLAXIS 2D. The methodology is validated using small-strain FEA employing a linear elastic perfectly plastic (elasto-plastic; EP) material model, incorporating the Mohr-Coulomb failure criterion and associated flow rule.

The numerical study first examines the suitability of ultimate limit state (ULS) analyses for practical use. Initially, small-strain EP models with non-associated flow are employed to evaluate the impact of the associated flow assumption in the validation modelling. Large-deformation FEA calculations using a Hypoplastic (HP) material model are then performed to consider the effects of soil stiffness and stress-state dependency. These findings inform the modelling approach for the second part of the numerical study, which focuses on serviceability limit state (SLS) analyses. Four key parameters are explored: caisson depth, anchor roughness, soil initial relative density, and the inclination of the under-ream.

6.2 Problem Definition

Figure 6.1 defines the problem and key variables considered in this chapter. The shaft base is enlarged to form an annular anchor around the caisson. The anchor is defined by its width (b), taper angle (β), and interface roughness factor (α). The interface roughness factor is defined by:

$$\tan\delta = \alpha \tan\phi \tag{6.1}$$

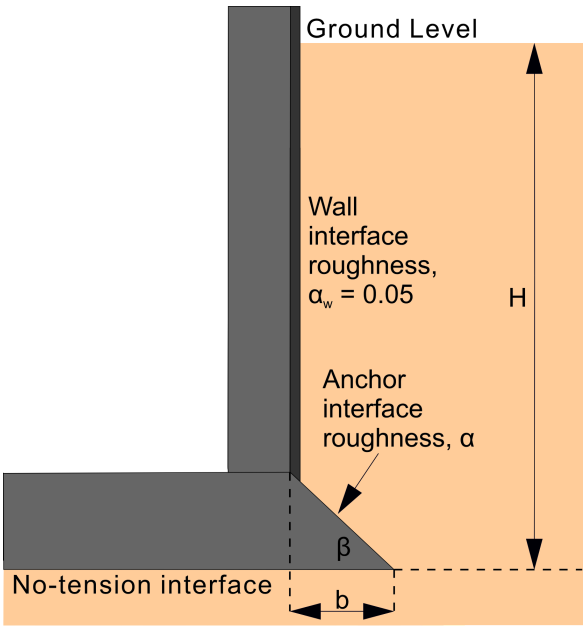


Figure 6.1: Plane strain problem definition including key features and parameters considered.

where δ is the interface friction angle and ϕ is the internal friction angle of the soil. The anchor interface roughness (α) can vary between $\alpha = 0$ (fully smooth) and $\alpha = 1$ (fully rough). A few key assumptions are made to ensure conservative predictions and to constrain the extensive parameter space: (i) plane strain conditions are assumed; (ii) the interface between the vertical shaft wall and surrounding soil is assumed to be approximately smooth ($\alpha_w = 0.05$); and (iii) no-tension conditions are imposed at the base-soil interface to avoid reliance on suction.

The caisson depth, H, is non-dimensionalised as H/b. The results are interpreted using a dimensionless uplift factor N_g (Merifield & Sloan, 2006):

$$N_g = \frac{F_v}{\gamma' H b} \tag{6.2}$$

where F_v is the vertical force exerted by the soil on the anchor (Figure 1.4) and γ' is the effective unit weight of the soil.

6.3 Finite-Element Analyses

6.3.1 Finite-Element Model

The FEA calculations were performed using PLAXIS 2D. The soil domain is meshed using fourth order 15-node elements. The caisson base, wall, and anchor are modelled as 5-node beam elements. For all models, the soil domain has: a fully fixed bottom boundary, horizontally

fixed side boundaries, and free ground level boundary. Dry soil conditions are assumed during modelling to ensure drained behaviour. In PLAXIS, this is achieved by defining the phreatic surface at the bottom of the soil domain. Uplift movement is simulated by applying a prescribed vertical displacement to the caisson. The caisson is fixed horizontally, tacitly modelling the caisson and anchor as a single rigid body. Since structural deformation is precluded under these constraints, the structural material properties are assigned arbitrarily. This study employs both small-strain and large-deformation analyses. The large-deformation analyses utilise the methodologies of Bathe (1982) and van Langen & Vermeer (1991). Further details are available in Bentley Systems (2024b).

6.3.2 Material Models

The HP model is used for the majority of the calculations (416 out of 468). Hypoplasticity is a class of non-linear constitutive models. In contrast to elasto-plasticity, strain is not decomposed into separate elastic and plastic parts. The model can predict features of soil behaviour not captured by 'traditional' EP modelling, including: (a) the critical state; (b) dependency of the peak strength on soil density and stress level; (c) non-linear behaviour in the small and large-strain range; and (d) dependency of the soil stiffness on the loading direction (Maŝín, 2010). The HP model developed by von Wolffersdorff (1996) is used in this study, using the implementation in PLAXIS developed by Maŝín (2010).

The HP model is defined using eight parameters: ϕ_c, h_s, n_{HP}, e_{d0}, e_{c0}, e_{i0}, α_{HP}, and β_{HP}. Four of the parameters have clear physical meanings: ϕ_c corresponds to the critical state friction angle, whilst the reference void ratios e_{d0}, e_{c0}, and e_{i0} correspond to the densest, critical state, and loosest particle packing at zero mean stress, respectively. Of the remaining parameters, h_s and n_{HP} are computed from oedometric loading curves, whilst α_{HP} and β_{HP} are calibrated using single-element simulations of drained triaxial tests. For further details on the parameters and calibration, refer to Herle & Gudehus (1999).

Two calibrated HP sands from recent studies are used in this chapter (Tasan & Yilmaz, 2019; Wichtmann et al., 2019). The HP parameters for each sand are given in Table 6.1, alongside a 'Soil ID' number, which is used to identify each soil hereon. Soils 1 and 2 are described in their sources as 'poorly graded medium to coarse sand' and 'Karlsruhe fine sand,' respectively. The

dry unit weight of both soils is fixed as $\gamma_d = 20$ kN/m^3. Since dry conditions are assumed, it follows that $\gamma' = \gamma_d$ when Equation 6.2 is applied in this study.

Table 6.1: Hypoplastic (HP) material model parameters for the two sands considered.

Soil ID	**Source**	$\boldsymbol{\phi_c}$ (°)	$\boldsymbol{h_s}$ (MPa)	$\boldsymbol{n_{HP}}$	$\boldsymbol{e_{d0}}$	$\boldsymbol{e_{c0}}$	$\boldsymbol{e_{i0}}$	$\boldsymbol{\alpha_{HP}}$	$\boldsymbol{\beta_{HP}}$
1	Tasan & Yilmaz (2019)	31.5	2300	0.30	0.391	0.688	0.791	0.13	1.00
2	Wichtmann et al. (2019)	33.1	4000	0.27	0.677	1.054	1.212	0.14	2.50

The interface strength is defined using classical frictional parameters: the interface friction angle (ϕ_{inter}), the interface dilatancy angle (ψ_{inter}), and the interface cohesion (c_{inter}). The following values are used in the modelling: $\phi_{inter} = \delta$ (see Equation 6.1); $\psi_{inter} = 0$; and $c_{inter} = 0.001$ kPa (for numerical stability). The interface stiffness is defined using a power law formulation based on oedometric stiffness (E_{oed}) defined by Equation 6.3 (Bentley Systems, 2024a):

$$E_{oed} = E_{oed}^{ref} \left(\frac{\sigma'_{\mathrm{n}}}{p_{ref}} \right)^{UD_{power}} \tag{6.3}$$

where σ'_n is the effective normal stress, p_{ref} is a reference stress level, E_{oed}^{ref} is the oedometric stiffness measured at p_{ref}, and UD_{power} is a curve-fitting exponent. This relationship enables stress-dependent stiffness compatible with the surrounding HP soil. To calibrate the interface models, PLAXIS was used to simulate an oedometer element test using the relevant HP soil parameters up to $p_{ref} = 100$ kPa. Least squares regression was then used to find optimal values for E_{oed}^{ref} and UD_{power}. Since the HP model accounts for the influence of initial soil density on stiffness, the interface model was calibrated individually for each soil and initial density level considered in this study.

A limited number of additional calculations were carried out using EP modelling. Fixed parameters used for these calculations are given in Table 6.2. For consistency, a value of $\gamma_d = 20$ kN/m^3 is adopted for the soil. To approximate rigid-plastic soil behaviour, the Young's modulus (E'_{ref}) is set to an unrealistically high value. The value used is several orders of magnitude greater than typical values for sands, which are generally in the order of 10^4 to 10^6 kN/m^2 (Kézdi, 1974). This approach is well established and has been shown not to affect the

resulting ultimate capacity (Griffiths, 1982). The Poisson's ratio (ν) matches similar recent modelling (Sheil & Templeman, 2023), whilst the small values adopted for cohesion (c'_{ref}) and tensile strength (σ'_t) ensure numerical stability and approximate zero tension conditions on the caisson base. The remaining parameters required to define the material model, namely the internal friction angle (ϕ) and the dilatancy angle (ψ), vary between calculations. The interfaces are also defined using the EP model. Interface stiffness is defined using the values in Table 6.2, whilst the strength parameters are consistent with those used in the HP modelling ($\phi_{inter} = \delta$; $\psi_{inter} = 0$; and $c_{inter} = 0.001$ kPa).

Table 6.2: Fixed parameters for the linear elastic perfectly plastic (EP) material model.

Parameter	**Value**
Dry unit weight, γ_d (kN/m^3)	20
Young's modulus, E'_{ref} (kN/m^2)	500×10^9
Poisson's ratio, ν	0.3
Cohesion, c'_{ref} (kN/m^2)	0.001
Tensile strength, σ'_t (kN/m^2)	0.001

6.3.3 Adaptive Remeshing in PLAXIS 2D

AR methods decrease reliance on manual 'trial and error' mesh sensitivity studies, as well as improving the numerical accuracy and computational efficiency of FEA calculations (e.g. Kardani et al., 2012; Zienkiewicz et al., 2013). PLAXIS is arguably the most popular geotechnical FEA software in industry, primarily due to its user-friendliness. Whilst the software is accessible, customisation of the modelling is challenging. As a result, whilst there are numerous examples of AR using alternative software packages, there are limited examples of AR implemented in PLAXIS.

The present approach is inspired by Martin (2011) but extended and customised to be compatible with PLAXIS modelling. Martin (2011) proposed a highly effective and straightforward AR method that seeks to equalise the quantity $\int \gamma_{\max} \, dA$ (integral of the maximum shear strain in each element) over all the elements of the mesh. Over multiple iterations, this process refines the mesh, concentrating elements in areas experiencing high shear strains. This approach

has been successfully implemented in a range of recent research (e.g. Royston et al., 2022a; Sheil & Templeman, 2023; Templeman et al., 2023; Sheil et al., 2024). These studies used the open-source program Triangle (Shewchuk, 1996; 2002) to generate the mesh coordinates, before importing them into the relevant FEA programme, which is not permitted in PLAXIS. The proposed AR procedure, which utilises PLAXIS' in-built mesh generator, is summarised in Figure 6.2.

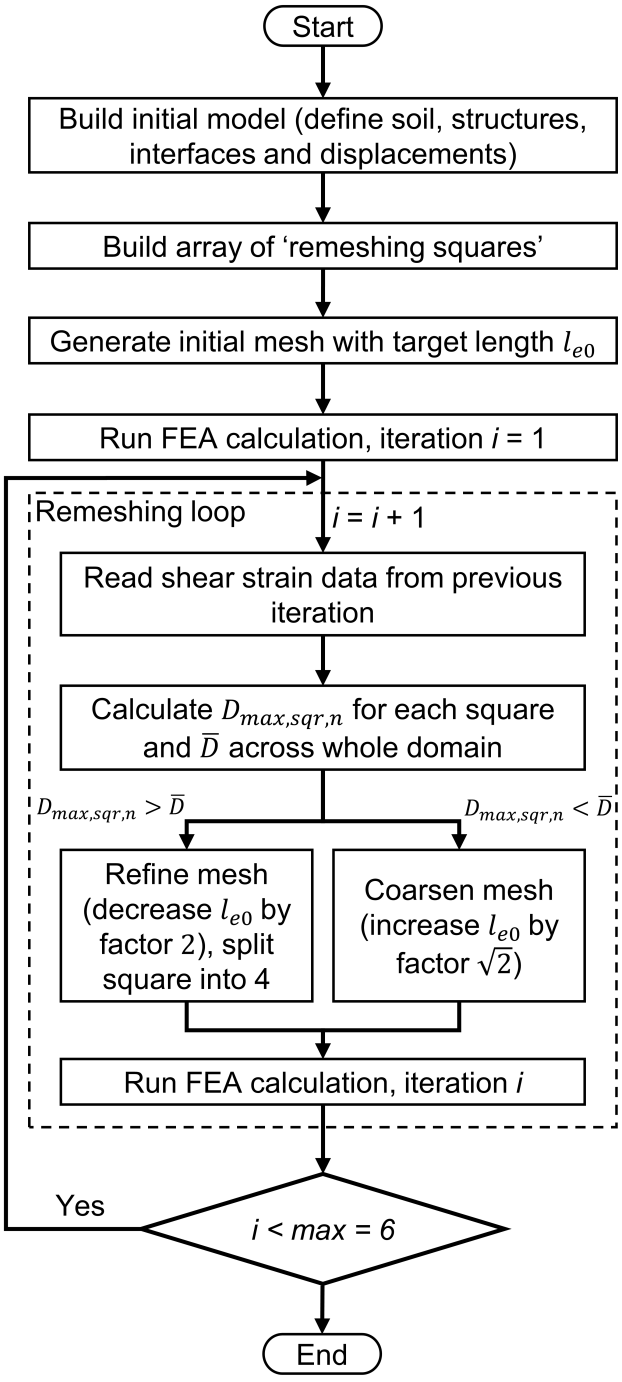


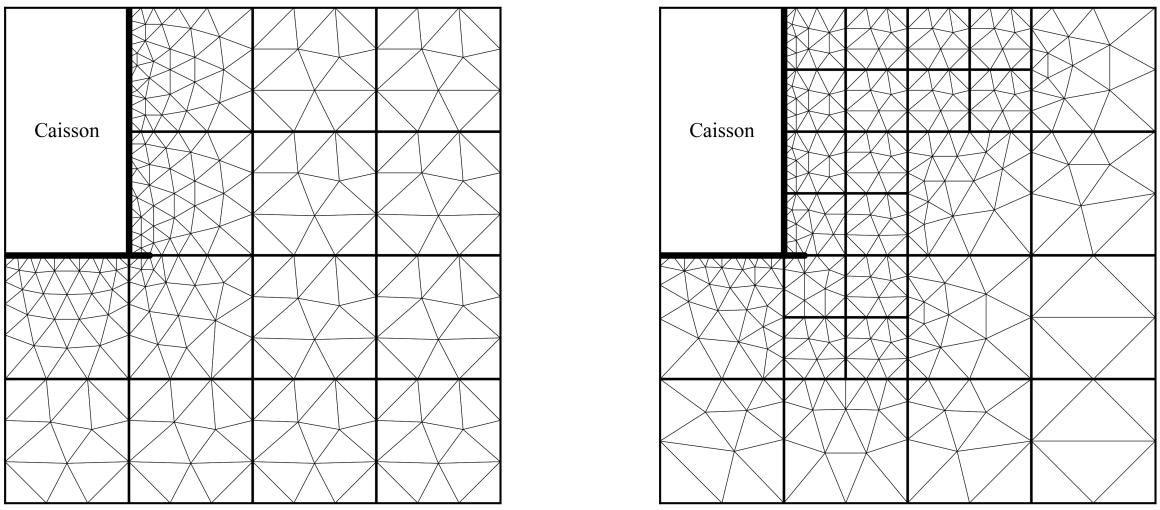
Figure 6.2: A flow chart representing the adaptive remeshing (AR) procedure.

In PLAXIS, global mesh density is controlled by inputting a target element dimension (l_{e0}), whilst local mesh density is controlled by defining geometries within the soil domain, within which l_{e0} can be increased or decreased locally using a local coarseness factor, F_c (Bentley Systems, 2024b). To harness this refinement procedure, the soil domain is subdivided into a grid of remeshing squares (see Figure 6.3a), within which the local target element dimension is $l_{e0,\text{sqr}} = F_c l_{e0}$. For the initial mesh, the squares are uniform, and the mesh is generated without local refinement (i.e. $F_c = 1$ in all squares; Figure 6.3a).

Following the calculation of iteration 1, the shear strain factor (D_n; Equation 6.4) is found for each element by extracting the maximum shear strain within each element ($\gamma_{\text{max},n}$) and multiplying it by the area of the given element (A_n). The maximum D_n value within each remeshing square is then found, denoted $D_{\text{max,sqr},n}$. Finally, $\bar{D}$ (the mean value of D_n across the domain of N elements) is calculated (Equation 6.5).

$$D_n = \gamma_{max,n} A_n \tag{6.4}$$

$$\bar{D} = \frac{1}{N} \sum_{n=1}^{N} D_n \tag{6.5}$$



(a) Iteration 1 (b) Iteration 2

Figure 6.3: (a) An exemplar first iteration mesh, sub-divided by remeshing squares; and (b) an exemplar second iteration mesh, demonstrating coarsening, refinement, and sub-division of remeshing squares.

From Figure 6.2, mesh refinement then takes place in remeshing squares with a high $D_{\text{max,sqr},n}$ (i.e. $> \bar{D}$), whereas mesh coarsening occurs in remeshing squares with a low $D_{\text{max,sqr},n}$ (i.e. $< \bar{D}$). Within PLAXIS, the local coarseness factor (F_c) can be specified in stepwise multi-

ples of $\sqrt{2}$, up to 10 times to refine and up to 6 times to coarsen. After each iteration, in squares that are coarsened, $l_{e0,\mathrm{sqr}}$ is increased by a factor $F_c = \sqrt{2}$. Conversely, in each square where refinement occurs, $l_{e0,\mathrm{sqr}}$ is decreased by two multiples of $\sqrt{2}$, i.e., $F_c = \left(1/\sqrt{2}\right)^2 = 1/2$. This enables up to 5 subsequent iterations, when the maximum refinement of $F_c = \left(1/\sqrt{2}\right)^{10} = 1/32$ will have been achieved in high-strain regions, and a maximum coarsening of $F_c = \left(\sqrt{2}\right)^5 = 4\sqrt{2} \approx 4.66$ will have occurred in low-strain regions. This limitation defines the maximum number of iterations in Figure 6.2 ($i = 6$). Each square which undergoes refinement is also subdivided into four new remeshing squares, enabling the mesh to be refined with more precision in subsequent iterations. Figure 6.3 presents two exemplar meshes, demonstrating refinement and subdivision (e.g. in the top left corner of Figure 6.3b), and coarsening (e.g. in the bottom right corner of Figure 6.3b). All the calculations in this chapter use 3 m $\times$ 3 m initial remeshing squares and l_{e0}= 1.2 m.

6.3.4 Finite-Element Calculation Stages

Each iteration of a given calculation involves the following steps:

1. Generate the soil domain and define the remeshing squares, which subdivide the domain. The initial stress state is generated using the PLAXIS K_0 procedure, which calculates vertical stresses that are in equilibrium with the self-weight of the soil. Horizontal stresses are determined from a user-defined coefficient of lateral earth pressure $K_0 = 0.5$.

2. Activate the caisson wall and interface, whilst deactivating the soil inside the caisson.

3. Activate the anchor and interface. The anchor width is set as $b = 1$ m for all models.

4. Deactivate any remaining soil within the caisson. Activate the caisson base and interface.

5. Apply an upwards displacement to the caisson until the termination condition is reached. Different termination conditions are used in different parts of this chapter, depending on the type of modelling.

6.4 Validation of Numerical Methods

To validate the methodology, results for a flat anchor ($\beta = 0°$) are compared to analogous results for conventional plate anchors (Figure 6.4). For these analyses, the calculation was terminated once the load-displacement curve reached a plateau. The results in Figure 6.4, which were calculated using the EP model with associated flow ($\psi = \phi$), are compared to the lower bounds calculated by Merifield & Sloan (2006) using finite-element limit analysis. The agreement between the results is excellent across a range of normalised depths (H/b) and soil friction angles (ϕ). Anchor roughness (α) is expected to have no influence on the capacity of a horizontal plate, which is also reflected well in Figure 6.4.

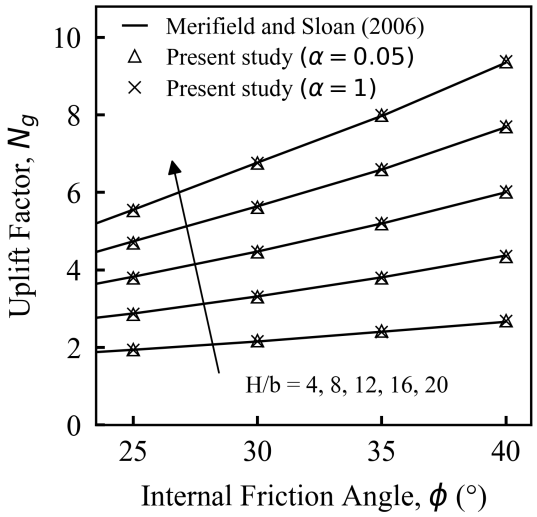
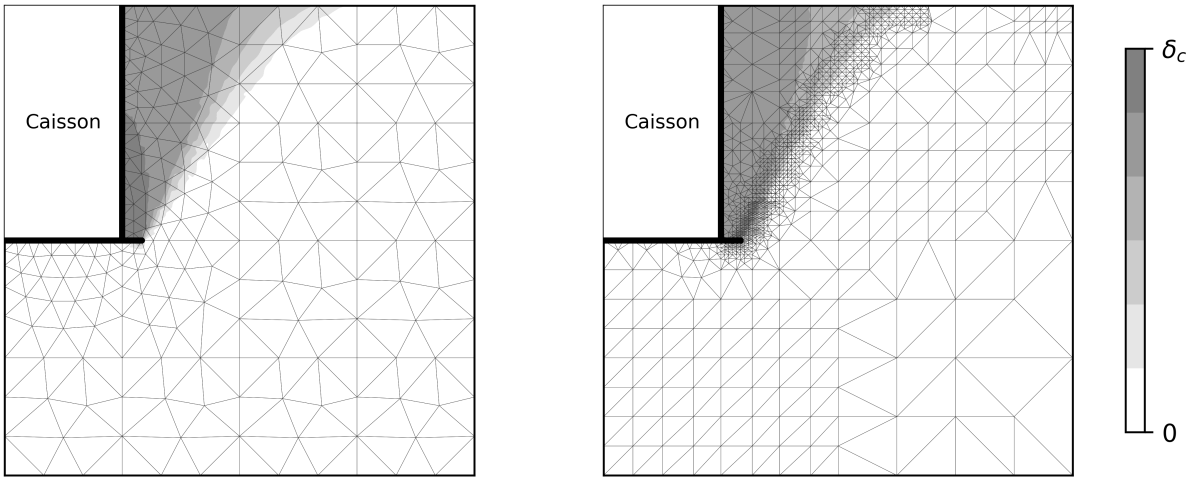


Figure 6.4: Validation of the finite-element modelling through comparison of uplift factors to previous solutions for horizontal plate anchors (Merifield & Sloan, 2006). Analyses carried out using linear elastic perfectly plastic (EP) material model with associated flow ($\psi = \phi$).

Figure 6.5 presents the mesh and total displacement field of an exemplar model after first and sixth iterations, demonstrating the progressive refinement and subdivision of the remeshing squares in high-strain regions. Comparison of the mesh with the superimposed total soil displacements demonstrates that the AR procedure effectively refines the mesh in high shear strain areas. Figure 6.6 plots the uplift capacity from each iteration against the corresponding number of elements, demonstrating that the remeshing procedure facilitates convergence to an accurate solution. Note that employing a uniform mesh with the maximum refinement level throughout the entire domain would require approximately 600,000 elements. In contrast, the present remeshing approach achieves comparable accuracy with only 13,962 elements (representing a

97.6% reduction) across the six iterations. A key benefit of the present remeshing procedure is the ability to coarsen the mesh, which was not possible in previous similar implementations of AR (e.g. Martin, 2011; Royston et al., 2022a; Sheil & Templeman, 2023; Templeman et al., 2023; Sheil et al., 2024). This is evident qualitatively in Figure 6.5b, where the mesh has visibly reduced in density in remote regions of the domain. Figure 6.6 quantitatively demonstrates the benefits of coarsening, most notably with the decrease in the number of elements between iteration 1 and 2.



(a) Iteration 1 (b) Iteration 6

Figure 6.5: An exemplar FEA mesh with total soil displacement superimposed: (a) after the 1^{st} iteration; (b) after the 6^{th} iteration. (EP model, $\beta = 0°$, $H/b = 12$, $\phi = 30°$, $\psi = \phi$, $\alpha = 0.05$). δ_c = total upwards caisson displacement.

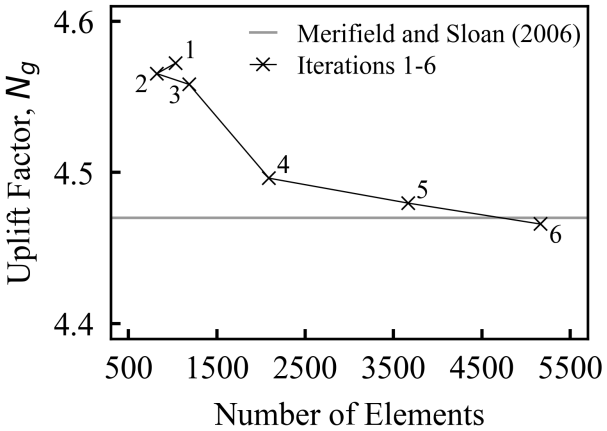


Figure 6.6: Exemplar convergence to a final result using the AR procedure (EP model, $\beta = 0°$, $H/b = 12$, $\phi = 30°$, $\psi = \phi$, $\alpha = 0.05$). Also shown is the lower bound solution from Merifield & Sloan (2006).

6.5 Flat Anchors (ULS)

6.5.1 Overview

Focusing on flat anchors ($\beta = 0°$), this section examines the suitability of ULS analyses for use in practice. To satisfy the ULS condition, these calculations were terminated upon identifying a plateau or peak in the load-displacement curve. The uplift capacity was then selected as the maximum load that occurred during the analysis, in accordance with the approach taken by Loukidis & Salgado (2009).

EP analyses were used for validation (Figure 6.4), assuming associated flow ($\psi = \phi$). This assumption is likely to be unrealistic in practice, especially in loose sands and at greater depths, where dilation is suppressed (Bolton, 1986). The first part of this section therefore investigates the impact of the associated flow assumption. Small-strain EP models with non-associated flow ($\psi = 0$) are analysed to enable direct comparison to the associated flow results in Figure 6.4. All 20 combinations of the parameters detailed in Table 6.3 are considered.

Table 6.3: Adopted parameter space for the small-strain ULS analyses (EP model).

Parameter	**Values**
Internal friction angle, ϕ	25°, 30°, 35°, 40°
Dimensionless depth, H/b	4, 8, 12, 16, 20
Anchor interface roughness, α	0.05
Anchor taper angle, β	0°
Dilatancy angle, ψ	0°

The second part of the ULS study explores the influence of the small-strain assumption by considering large-deformation FEA calculations using HP modelling. This approach provides insights into the realistic deformations required to achieve ULS, as well as the effects of stress level and relative density. Eight analyses are undertaken, considering the parameters detailed in Table 6.4.

Table 6.4: Adopted parameter space for the large-deformation ULS analyses (HP model).

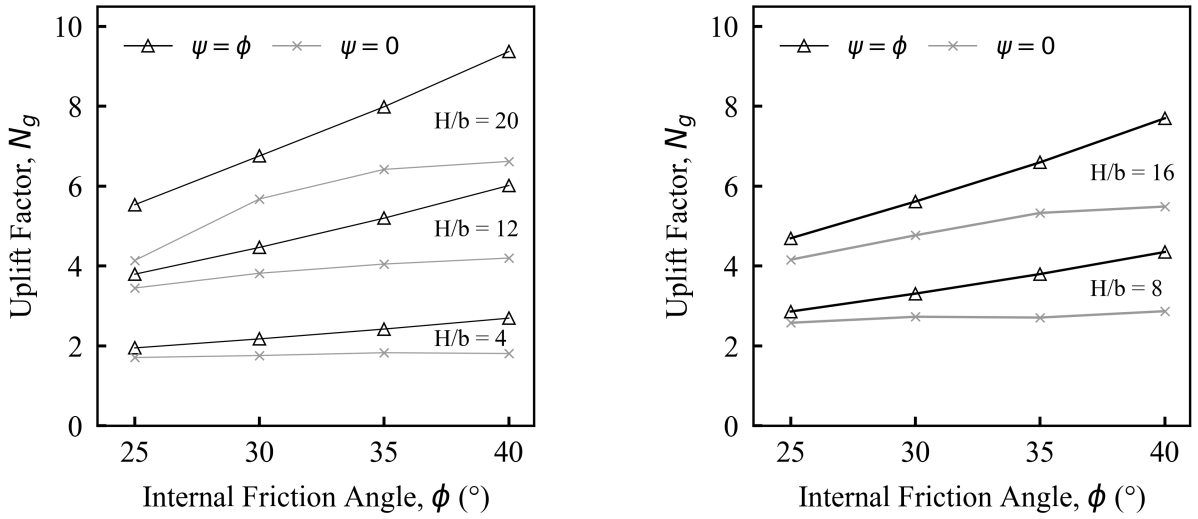
Parameter	**Values**
Soil type	Soil 1 ($\phi_c = 31.5°$), Soil 2 ($\phi_c = 33.1°$)
Dimensionless depth, H/b	4, 12
Anchor interface roughness, α	0.05
Anchor taper angle, β	0°
Initial density, I_{d0}	0%, 90%

6.5.2 ULS Results: Influence of the Associated Flow Assumption

Figure 6.7 shows that the assumption of associated flow leads to significantly greater uplift capacities than when non-associated flow is assumed. The biggest differences in uplift capacity are observed at greater depths and higher internal friction angles. For example, the non-associated analysis for $H/b = 20$ and $\phi = 40°$ leads to a 32.9% lower N_g than the equivalent associated flow result. In contrast, the smallest relative difference (9.1%) is observed when $H/b = 12$ and $\phi = 25°$. The notably low non-associated uplift capacity recorded for $H/b = 20$ and $\phi = 25°$ is attributed to a localised 'flow-around' mechanism, similar to those observed in undrained conditions (Sheil et al., 2024). All other analyses revealed failure mechanisms extending to ground level, such as those illustrated in Figure 6.8. Associated flow models exhibited larger failure surfaces (Figure 6.8a), and consequently higher uplift capacities compared to non-associated flow models (Figure 6.8b). At greater depths, there is a more significant difference between the length of the associated and non-associated flow failure surfaces, leading to greater reductions in uplift capacity.

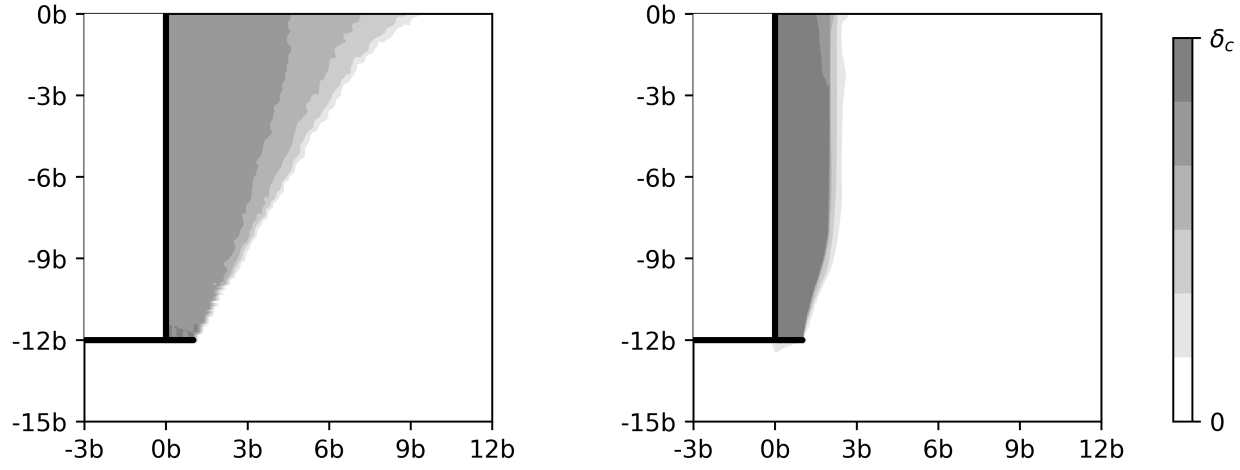
6.5.3 ULS Results: Influence of Soil State Dependence and Stiffness

The non-associated EP results in Figure 6.7 demonstrate the substantial impact of dilation on uplift capacity. Recognising that both stress level and relative density influence dilation, a series of calculations were undertaken using the HP model, which accounts for these factors (Table 6.4). 'Real' HP soils were considered (Table 6.1), such that the results correspond to realistic stiffnesses. Large-deformation analyses were therefore required to achieve the high



(a) (b)

Figure 6.7: Comparison of flat anchor ULS results ($\beta = 0°$; $\alpha = 0.05$). EP model with associated flow ($\psi = \phi$) and non-associated flow ($\psi = 0$): (a) $H/b = 4, 12, 20$; (b) $H/b = 8, 16$.



(a) $H/b = 12$, $\psi = \phi$ (b) $H/b = 12$, $\psi = 0$

Figure 6.8: Exemplar displacement fields for a flat anchor, with (a) associated flow ($\psi = \phi$); (b) non-associated flow ($\psi = 0$). ($H/b = 12$, ULS, EP model, $\beta = 0°$, $\phi = 30°$, $\alpha = 0.05$). Contours of total soil displacement. Mesh excluded for clarity. Axes indicate distance in terms of anchor width, b (x-axis = distance from caisson wall; y-axis = depth). δ_c = total upwards caisson displacement.

displacements needed to satisfy the ULS calculation termination condition (a plateau or peak in the load-displacement curve). The results are plotted alongside the EP calculations in Figure 6.9. Note that such comparisons are indicative only, given the HP results are plotted as a function of ϕ_c whereas the EP results are plotted against ϕ. At shallow depths ($H/b = 4$), the loose HP results ($I_{d0} = 0\%$) agree well with the EP non-associated flow results (no dilation is expected for both cases). Similarly, where significant dilation is expected, the dense HP results

($I_{d0} = 90\%$) agree well with the EP associated flow results. These results are explained by the exemplar failure mechanisms presented in Figure 6.10, which demonstrate similar 'block' style failures to those presented in Figure 6.8 for the EP analysis.

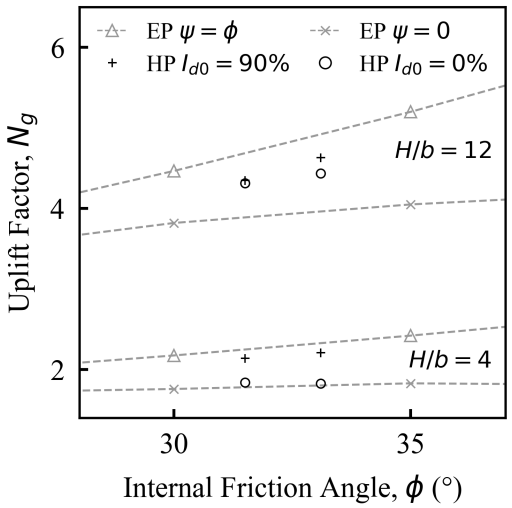
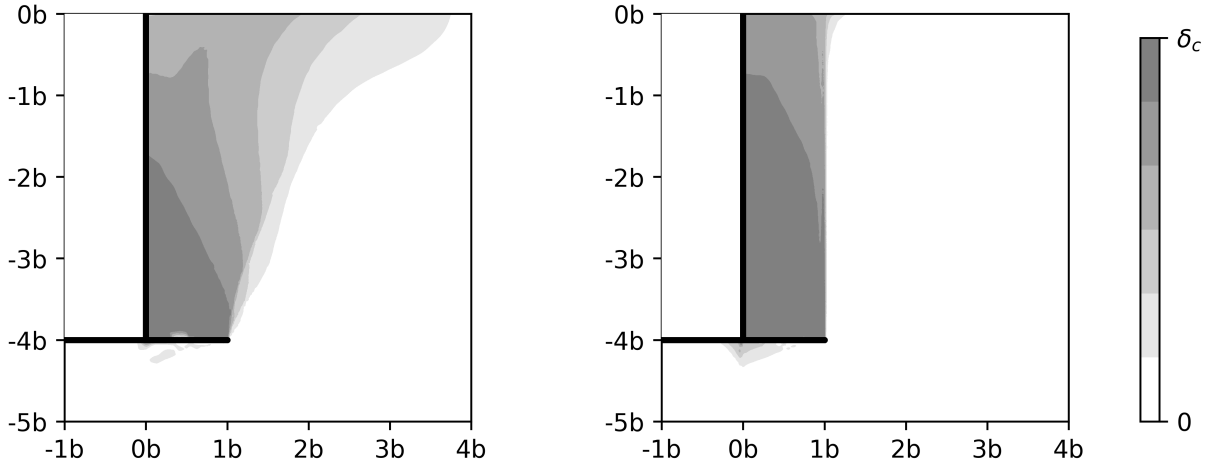


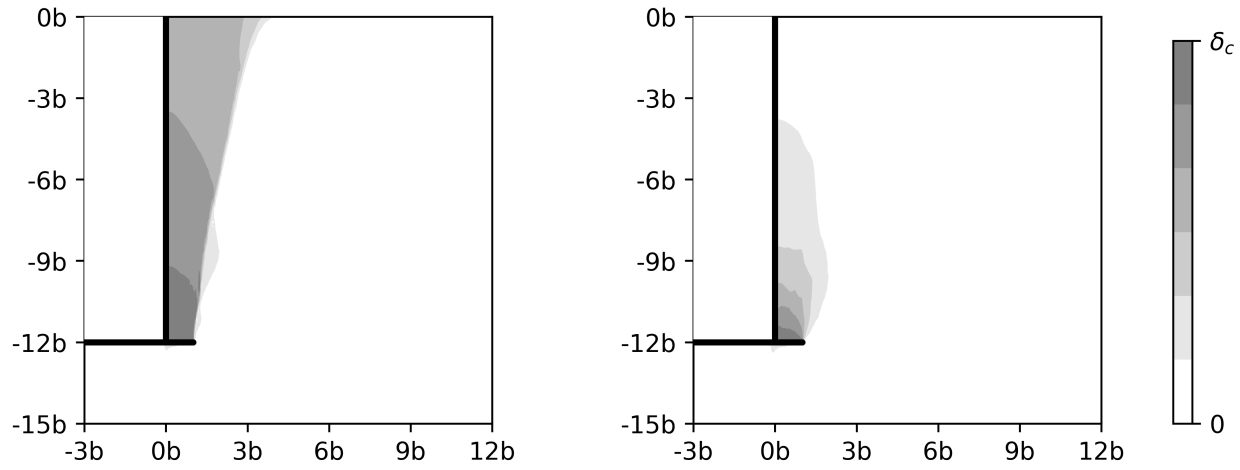
Figure 6.9: Hypoplastic (HP) large deformation analyses for a flat anchor compared to equivalent EP analyses ($\beta = 0°$; $\alpha = 0.05$; $H/b = 4$ and $H/b = 12$). Plotted: EP associated flow ($\psi = \phi$); EP non-associated flow ($\psi = 0$); HP initially loose ($I_{d0} = 0\%$); and HP initially dense ($I_{d0} = 90\%$).



(a) $H/b = 4$, $I_{d0} = 90\%$ (b) $H/b = 4$, $I_{d0} = 0\%$

Figure 6.10: Exemplar large deformation displacement fields for a flat anchor using the HP model: (a) initially dense ($I_{d0} = 90\%$); (b) initially loose ($I_{d0} = 0\%$). ($H/b = 4$, ULS, $\beta = 0°$, Soil 1, $\phi_c = 31.5°$, $\alpha = 0.05$). Contours of total soil displacement. Mesh excluded for clarity. Axes indicate distance in terms of anchor width, b (x-axis = distance from caisson wall; y-axis = depth). δ_c = total upwards caisson displacement.

In contrast to the shallow results, the deep ($H/b = 12$) HP large-deformation results show significant differences compared to the analogous EP calculations (Figure 6.9). Firstly, the results for the dense HP sands ($I_{d0} = 90\%$) are lower than the associated EP results. Figure



(a) $H/b = 12$, $I_{d0} = 90\%$ (b) $H/b = 12$, $I_{d0} = 0\%$

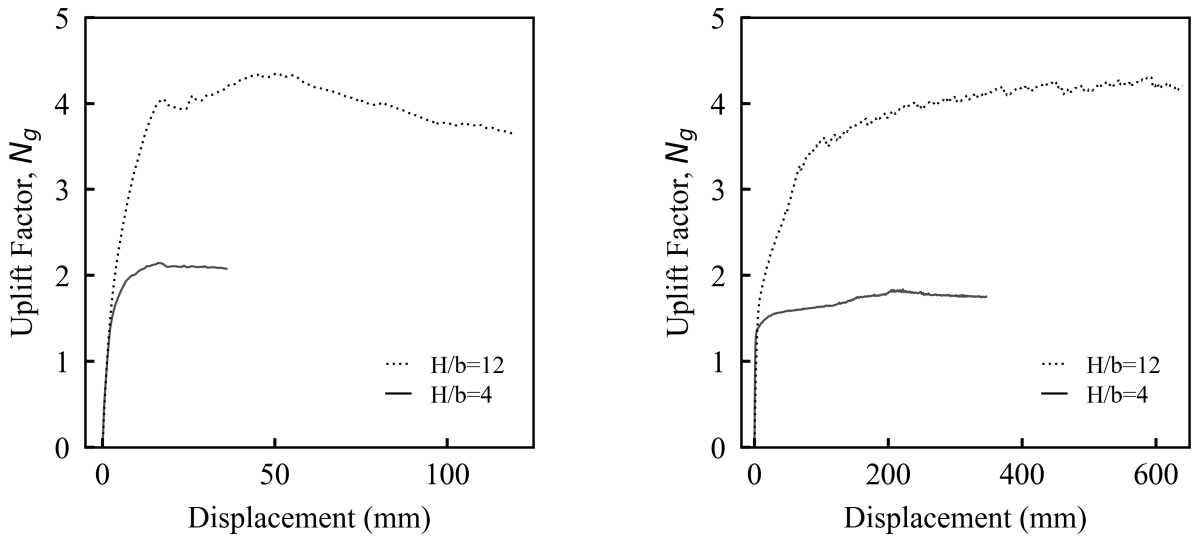
Figure 6.11: Exemplar large deformation displacement fields for a flat anchor using the HP model: (a) initially dense ($I_{d0} = 90\%$); (b) initially loose ($I_{d0} = 0\%$). ($H/b = 12$, ULS, $\beta = 0°$, Soil 1, $\phi_c = 31.5°$, $\alpha = 0.05$). Contours of total soil displacement. Mesh excluded for clarity. Axes indicate distance in terms of anchor width, b (x-axis = distance from caisson wall; y-axis = depth). δ_c = total upwards caisson displacement.

6.11 plots the total displacement fields for Soil 1 at $H/b = 12$. For the dense sample (Figure 6.11a), failure is still characterised by 'block' failure, but the width of the 'block' is narrower when compared to the equivalent associated EP analyses (Figure 6.8a), resulting in the lower capacity observed in Figure 6.9. This is likely caused by the suppression of dilation at greater depths, leading to lower peak strength. From Figure 6.9, the loose results ($I_{d0} = 0\%$) for $H/b = 12$ also diverge from the non-associated EP analyses. This is because 'block' failure is no longer governing uplift capacity, as demonstrated in Figure 6.11b. Instead, negligible displacement is observed at ground level, suggesting the failure of the anchor is mostly 'stiffness driven'.

Figure 6.12 presents exemplar load-displacement curves from the large-deformation analyses for Soil 1. The dense samples experience pronounced peak loads at relatively low displacements (16 mm and 51 mm for $H/b = 4$ and $H/b = 12$, respectively). In contrast, the loose samples initially exhibit a work-hardening response until peak loads are observed at much larger displacements (222 mm and 590 mm for $H/b = 4$ and $H/b = 12$, respectively).

6.5.4 Suitability of ULS Analyses in Practice

The present ULS analyses highlight the limitations of the EP model in capturing essential soil behaviours, such as stiffness and stress-state dependency. Whilst HP modelling can address



(a) $I_{d0} = 90\%$ (b) $I_{d0} = 0\%$

Figure 6.12: Exemplar load-displacement curves for large-deformation FEA analyses carried out using the HP model for: (a) initially dense sand ($I_{d0} = 90\%$); and (b) initially loose sand ($I_{d0} = 0\%$). ($\beta = 0°$, Soil 1, $\phi = 31.5°$, $\alpha = 0.05$).

these issues, the predicted failure displacements often significantly exceed acceptable values in practice. The results suggest ULS analyses may be suitable only for shallow depths in dense soils, where low displacements are required to realise failure (Figure 6.12a; $H/b = 4$).

Whilst traditional design methods commonly rely on ULS calculations with an applied factor of safety, SLS methods offer the potential for more economical design and are increasingly favoured in practice. In light of this, and considering the limitations of ULS analyses established above, the remainder of this chapter focuses on uplift resistance developed at a specified displacement that satisfies SLS conditions. Previous studies have used specified displacements to define plate anchor 'failure' (Liu et al., 2014). For example, Song et al. (2008) defined 'failure' of a circular anchor at a displacement of $0.2D$ (D = anchor diameter), whilst Mistri & Singh (2011) employed a different approach, using 2.5% of the plate embedment depth as the failure criterion. Such approaches are arbitrary to differing extents and have limited practical application in design. Instead, the next section focuses on small deformation FEA undertaken using a fixed displacement of 10 mm. Working in collaboration with industry partners, this displacement was chosen as a likely maximum tolerable deformation to prevent damage to adjoining structures such as tunnels. This value also aligns well with typical settlements considered tolerable in current design practice. For example, 10 mm is specified as the critical value above which any settlements will be investigated on the current High-Speed Rail 2 project in

the UK (HS2, 2017).

6.6 Inclined Anchors (SLS)

6.6.1 Overview

To provide an improved basis for design, a parametric study was conducted to investigate the SLS uplift resistance of inclined anchors. Two soils are considered to explore the repeatability of results between the soils. Four other key parameters are systematically varied: depth (H/b); anchor roughness (α); anchor taper angle (β); and soil initial density (I_{d0}). Using HP modelling and a fixed displacement of 10 mm, all 400 combinations of the parameters detailed in Table 6.5 are considered.

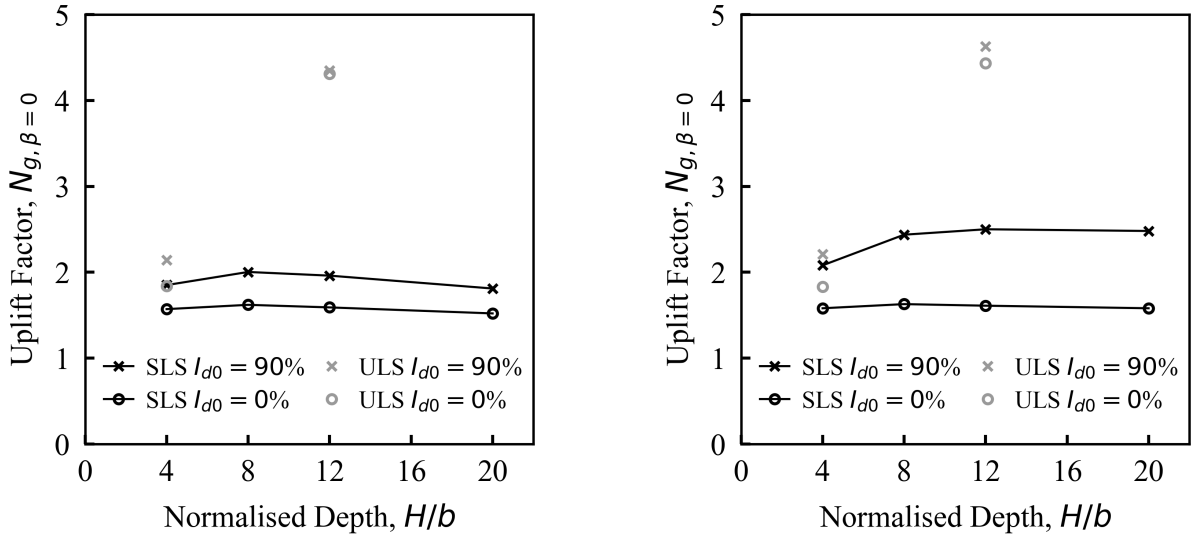
Table 6.5: Adopted parameter space for small-strain SLS analyses (HP model).

Parameter	**Values**
Soil type	Soil 1 ($\phi_c = 31.5°$), Soil 2 ($\phi_c = 33.1°$)
Dimensionless depth, H/b	4, 8, 12, 20
Anchor interface roughness, α	0.05, 0.25, 0.5, 0.75, 1
Anchor taper angle, β	0°, 15°, 30°, 45°, 60°
Initial density, I_{d0}	0%, 90%

6.6.2 SLS Results: Flat Anchors

Figure 6.13 plots the SLS uplift resistance for flat anchors ($N_{g,\beta=0}$) against H/b, alongside the equivalent ULS results (where applicable). The results consider both initially loose ($I_{d0} = 0\%$) and initially dense sand ($I_{d0} = 90\%$). Only results for $\alpha = 0.05$ are shown, since α has a negligible influence when $\beta = 0°$. Figure 6.13 demonstrates that higher uplift resistance is observed for dense sand in all cases. Increasing H/b has limited influence on $N_{g,\beta=0}$: given $N_g \propto 1/H$ (see Equation 6.2), this indicates that the SLS uplift resistance has an approximately linear relationship with depth. A comparison of the SLS and ULS results reveals relatively good agreement at shallow depths ($H/b = 4$), verifying that ULS analyses may be suitable for such cases. However, significant discrepancies emerge at greater depths ($H/b = 12$), emphasising

the limitations of ULS analyses.



(a) Soil 1 ($\phi_c = 31.5°$)

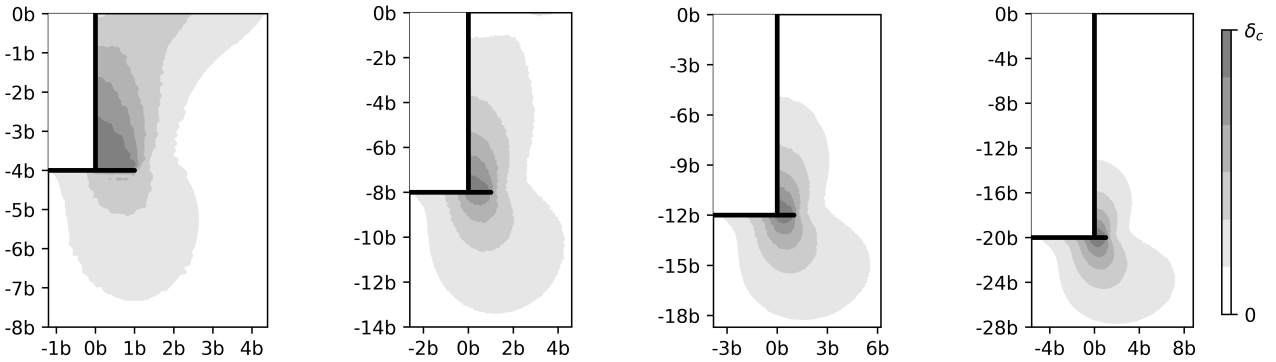
(b) Soil 2 ($\phi_c = 33.1°$)

Figure 6.13: SLS uplift resistance for flat anchors in Soils 1 and 2, compared to the equivalent ULS results from Figure 6.9. (HP model, $\beta = 0°$; $\alpha = 0.05$; $I_{d0} = 0\%$, 90%).

Representative soil displacements are plotted in Figure 6.14 for the flat anchor SLS results. At shallow depths ($H/b = 4$; Figure 6.14a), soil displacement extends to ground level. At greater depths ($H/b = 8, 12, 20$; Figure 6.14b - 6.14d), negligible displacement occurs at ground level, suggesting that resistance is governed by soil compression above the anchor. The shape and extent of the soil displacement field appears to be independent of depth, extending $\sim 7b$ above and below the anchor in all three deep-embedment cases (Figure 6.14b - 6.14d). This consistency likely explains the independence of $N_{g,\beta=0}$ with respect to depth (Figure 6.13).

6.6.3 SLS Results: Inclined Anchors

Figure 6.15 investigates the influence of β and α on uplift resistance by normalising the FEA results by the equivalent flat anchor result from Figure 6.13 (i.e. $N_{g,\beta=0}$ for the same soil, H/b, I_{d0}, and α). Figure 6.15 shows that increasing β leads to decreases in N_g (exception: $\beta = 15°$ for $H/b = 8$ and 20). For $\beta \leq 30°$, N_g is typically similar to the flat anchor result, and α has little influence. For $\beta > 30°$, α has a significant influence because the soil displacement mechanism involves much greater shearing at the anchor-soil interface. As a result, for low α values ($\alpha = 0.05, 0.25, 0.5$), significant decreases in uplift resistance are observed, whilst only minor reductions in resistance are observed for $\alpha = 0.75$ and 1. For $\beta = 60°$, uplift resistance



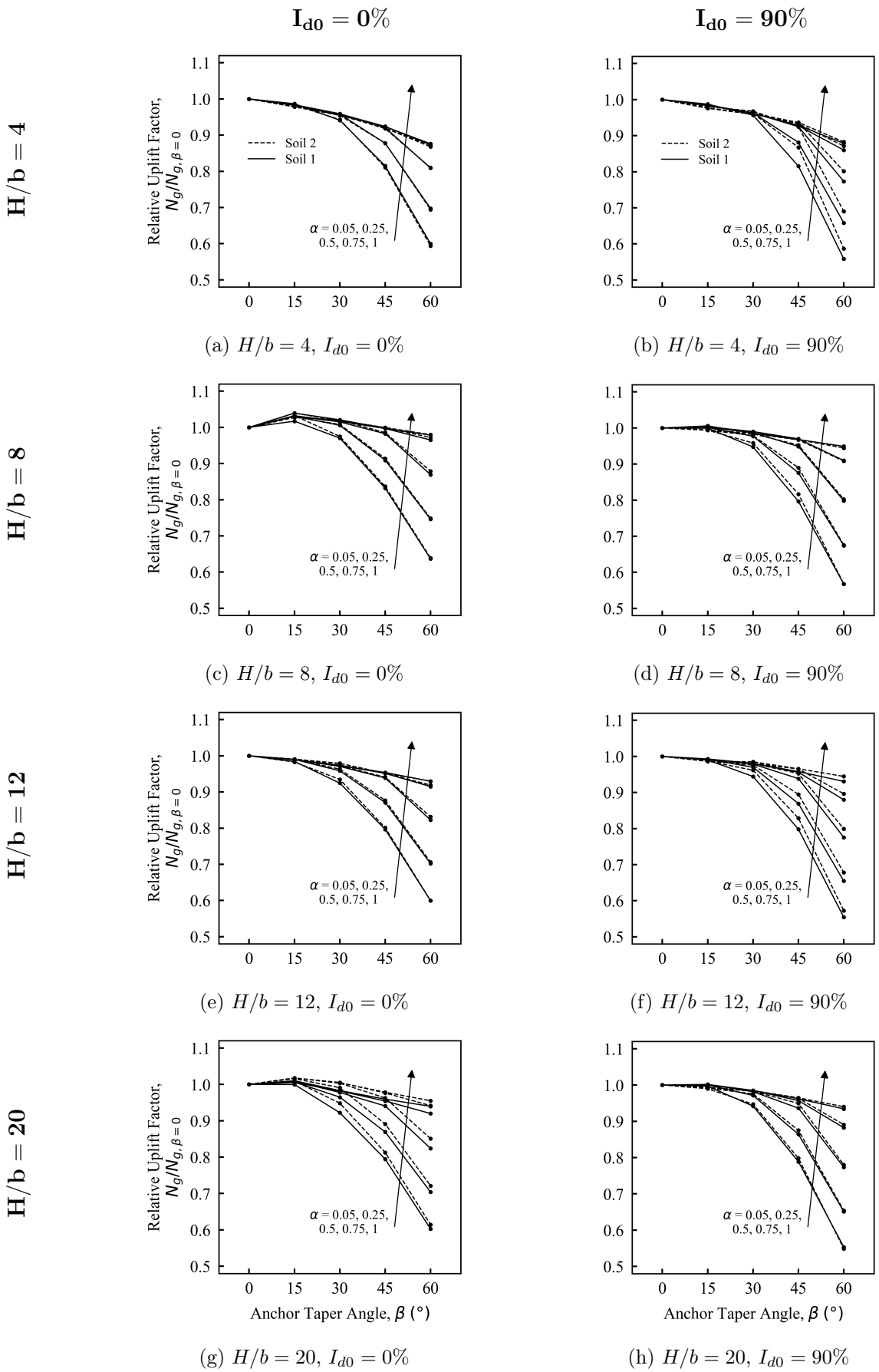
(a) $H/b = 4$ (b) $H/b = 8$ (c) $H/b = 12$ (d) $H/b = 20$

Figure 6.14: Exemplar SLS displacement fields for a flat anchor (HP model, Soil 1, $\beta = 0°$, $\alpha = 0.05$, $I_{d0} = 90\%$). Contours of total soil displacement. Mesh excluded for clarity. Each plot uses a different length scale for clarity. Axes indicate distance in terms of anchor width, b (x-axis = distance from caisson wall; y-axis = depth). δ_c = total upwards caisson displacement (10 mm).

increases approximately linearly with increasing α between 0.05 and 0.75, whilst increasing α from 0.75 to 1 leads to a smaller increase. The results therefore suggest that minimising β is desirable in order to: (i) maximise N_g; and (ii) minimise the influence of α.

Overall, Figure 6.15 suggests that relative uplift resistance ($N_g/N_{g,\beta=0}$) is strongly driven by β and α, but relatively insensitive to soil type, H/b and I_{d0}. Figure 6.13 indicates that soil type and I_{d0} can have an influence on the $N_{g,\beta=0}$ results, however. Therefore, it is concluded that N_g is independent of H/b for a given set of soil conditions.

To further investigate the influence of β and α, exemplar soil displacements for $\alpha = 0.05, 1$ and $\beta = 0°, 30°, 60°$ are plotted in Figure 6.16. When α is low (Figures 6.16a - 6.16c), increasing β significantly reduces soil mobilisation and compression, resulting in a substantial reduction in uplift resistance. For example, the displacement field in Figure 6.15c ($\alpha = 0.05$, $\beta = 60°$) shows a 44% reduction in uplift resistance compared to Figure 6.15a ($\alpha = 0.05$, $\beta = 0°$). In contrast, when α is high (Figures 6.16d - 6.16f), the impact of β on displacement patterns is less pronounced, resulting in a smaller reduction in uplift resistance. Comparing Figures 6.16b ($\alpha = 0.05$, $\beta = 30°$) and 6.15e ($\alpha = 1$, $\beta = 30°$), it is evident that α has little influence when $\beta \leq 30°$. However, for larger taper angles (i.e., $\beta = 60°$), α has a significant influence. This is exemplified by the reduced soil mobilisation in Figure 6.16c ($\alpha = 0.05$, $\beta = 60°$), producing a 37% reduction in uplift resistance compared to Figure 6.16f ($\alpha = 1$, $\beta = 60°$).



(a) $H/b = 4$, $I_{d0} = 0\%$

(b) $H/b = 4$, $I_{d0} = 90\%$

(c) $H/b = 8$, $I_{d0} = 0\%$

(d) $H/b = 8$, $I_{d0} = 90\%$

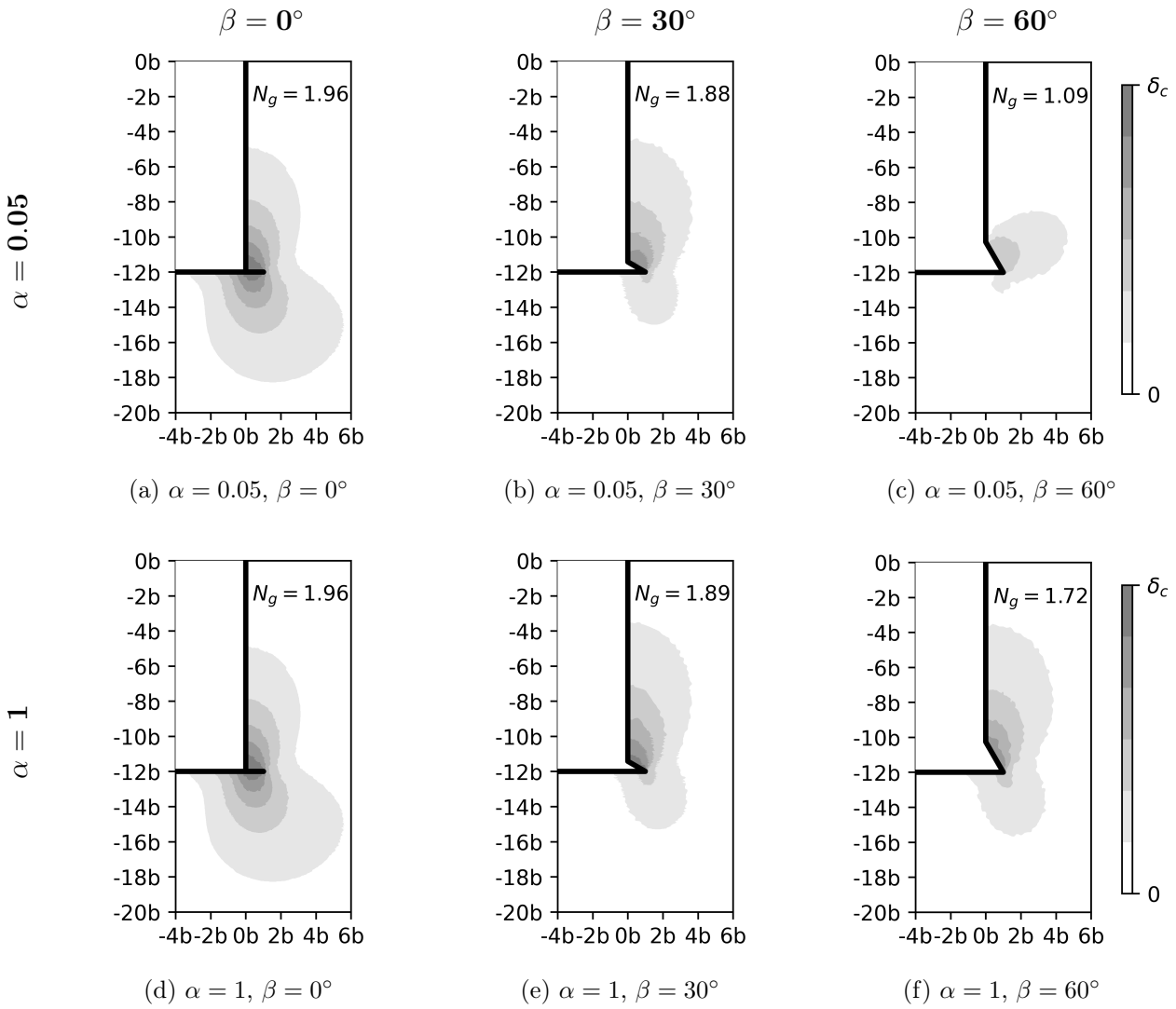
(e) $H/b = 12$, $I_{d0} = 0\%$

(f) $H/b = 12$, $I_{d0} = 90\%$

(g) $H/b = 20$, $I_{d0} = 0\%$

(h) $H/b = 20$, $I_{d0} = 90\%$

Figure 6.15: The influence of anchor taper angle (β) on anchor uplift factor. SLS results using the HP material model.



(a) $\alpha = 0.05$, $\beta = 0°$ (b) $\alpha = 0.05$, $\beta = 30°$ (c) $\alpha = 0.05$, $\beta = 60°$

(d) $\alpha = 1$, $\beta = 0°$ (e) $\alpha = 1$, $\beta = 30°$ (f) $\alpha = 1$, $\beta = 60°$

Figure 6.16: Exemplar SLS displacement fields for inclined anchors, demonstrating the influence of α and β. (HP model, Soil 1, $I_{d0} = 90\%$). Contours of total soil displacement. Mesh excluded for clarity. Axes indicate distance in terms of anchor width, b (x-axis = distance from caisson wall; y-axis = depth). δ_c = total upwards caisson displacement (10 mm).

6.7 Limitations

The shear strength, stiffness, and dilatancy of drained materials are highly influenced by density, confining stress, and shear strain, making rigorous modelling complex. Whilst the present modelling was carefully designed to account for these factors, there remain important limitations that must be considered when applying these results in practice. Most importantly, the parametric study was carried out using HP model parameters calibrated to two specific sands with relatively similar critical friction angles. The results should be applied to other soils with caution, especially those with different strengths.

The present study considered a fixed anchor width of 1 m. It is well-established that uplift

capacity factors increase with decreasing anchor width (Khatri & Kumar, 2011). The present results could be conservatively applied to smaller anchors ($b \leq 1$ m), but are not suitable for larger anchors. Given the thesis aims to reduce over-conservatism, it is recommended that the present results are only applied to anchors with a width of 1 m to avoid overly conservative designs. Considering the practical challenges of constructing anchors wider than 1 m and the limited capacity likely provided by smaller anchors, the results of this study remain highly relevant.

All the results are expressed in terms of N_g (see Equation 6.2), which assumes uplift capacity scales linearly with confining pressure. This approach is adopted given the considerable precedent for normalising uplift capacity in this manner (e.g. Merifield & Sloan, 2006; Merifield et al., 2006; Giampa et al., 2019; Roy et al., 2021; Roy et al., 2022). Whilst this assumption holds for the ULS analyses, it may not apply to the SLS analyses, where uplift resistance was shown to be stiffness-driven. Despite this potential source of error, the SLS results are still expressed in terms of N_g for consistency and to enable effective comparison with the ULS results. The discrepancy only affects Figure 6.13, which presents absolute $N_{g,\beta=0}$ values. As a result of the potential discrepancy, it is recommended that these results (Figure 6.13) are not directly applied in practice. Results in Figure 6.15 are presented as a relative uplift capacity factor, $N_g/N_{g,\beta=0}$, which, by considering Equation 6.2, simply corresponds to the ratio of absolute vertical forces (F_v), since the other variables cancel out. The relative uplift capacity factors can therefore be applied with confidence, regardless of any concerns about non-dimensionalisation using N_g.

6.8 Summary

This chapter investigated the uplift resistance of under-reamed caissons in sand using finite-element analysis in PLAXIS 2D, employing a novel workaround to implement fully automated AR using Python and the PLAXIS Remote Scripting Interface. The modelling approach was validated by comparing predictions to conventional plate anchors using an EP model with Mohr-Coulomb failure criterion and associated flow.

The first part of the numerical study examined the suitability of ULS analyses for use in practice. EP analyses employing non-associated flow revealed that the associated flow assump-

tion may overestimate uplift capacity. To consider the influence of additional soil behaviours, such as realistic stiffness and stress-state dependency, large-deformation analyses were undertaken using a HP material model. The results suggest that ULS analyses may be reliable in dense sands at shallow depths. However, in loose sands and at greater depths, the predicted displacements at failure were impractically large for design applications. Most realistic depths are sufficient to render ULS analyses ineffective. Therefore, the remainder of the study focused on small deformation, SLS analyses using the HP model with a fixed displacement of 10 mm.

The SLS study investigated the influence of depth (H/b), anchor taper angle (β), anchor roughness (α), and initial soil relative density (I_{d0}) on non-dimensionalised uplift resistance (N_g) for two sands. The results demonstrated depth had limited influence on N_g under SLS conditions, indicating that SLS uplift resistance has an approximately linear relationship with depth. Increasing β led to significant decreases in N_g for low α, whilst more modest decreases were observed for high α. The results suggest that it is desirable to minimise β in design to: (i) maximise N_g; and (ii) minimise the influence of α. For a given soil, N_g was shown to be independent of H/b, making N_g a function of β and α alone.

7 Applications and Discussion

7.1 Introduction

This chapter provides further analysis and a critical discussion on the application of the findings from the preceding chapters. It begins with an examination of the grout injection process. A bespoke modelling approach, based on first principles of VF, is developed and validated using experimental data from Chapter 5. The primary grout injection results (Chapter 5) are then compared with those from the uplift testing (Chapter 4). Additionally, potential remedial measures to ensure a uniform spread of grout in practice are discussed.

The uplift experimental results from Chapter 4 are then used to derive an operational friction factor for design purposes. Comparisons are made with bored pile construction, exploring the applicability of the present findings to different soil types and the relevance of existing bored pile literature to caisson design. The numerical results (Chapter 6) are then used to develop a design chart for preliminary design of under-reamed caissons.

The final part of this chapter focuses on reducing EC. Using the results from Chapter 3, MT is compared with OCI, the principal alternative pipeline construction method. Additional analysis examines the impact of high-level design optimisation in MT, particularly the reduction of the number of shafts. A critical discussion follows on the contribution of construction materials to EC, incorporating the EC results from Chapter 3 to evaluate the impact of different steel production methods. Finally, a realistic caisson case study is presented to verify the potential for the uplift friction results (Chapter 4) and under-reaming results (Chapter 6) to reduce carbon emissions by reducing reliance on caisson self-weight.

7.2 Grout Injection Design Model

7.2.1 Problem Definition

To model grout injection, the problem depicted in Figure 7.1 is considered. The injection of grout into bentonite is simplified by approximating the annulus as planar, creating a 2D problem. The grout is considered to be flowing into the annulus (flow rate Q m^3/s) from a point source. The grout profile at a given point in time is defined in radial coordinates (R, θ),

and the direction of grout flow in the annulus is assumed to be purely radial. Other important parameters are indicated in Figure 7.1, including the direction of gravity, plus the densities (ρ) and viscosities (μ) of the grout and bentonite.

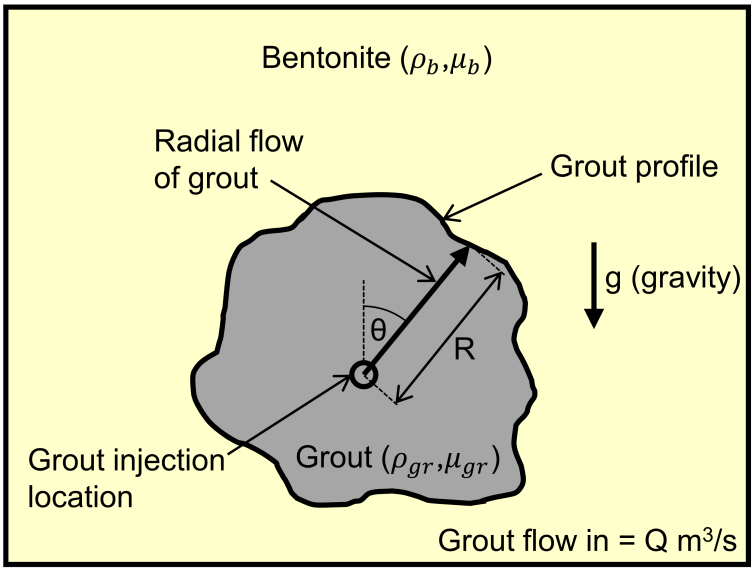


Figure 7.1: Problem definition showing the key parameters that influence the grout injection process.

7.2.2 Model Derivation

Stability of the grout injection process, and hence the likelihood of uniform spread, can be considered using Darcy's law (see Section 2.5.3). In one dimension, and in radial coordinates, Darcy's law can be defined as:

$$\frac{dp}{dR} = -\frac{\mu U}{k} + \rho g \tag{7.1}$$

where p is pressure, μ is viscosity, U is the injection velocity, k is the permeability, and ρ is the fluid density. For the present problem, it follows that the pressure exerted by the injected fluid (grout; subscript gr) on the displaced fluid (bentonite; subscript b) over a virtual displacement of δR can be defined as:

$$\delta p = p_{\mathrm{gr}} - p_b = \left[\left(\mu_b(\dot{\gamma}) - \mu_{\mathrm{gr}}(\dot{\gamma})\right)\frac{U}{k} + (\rho_b - \rho_{\mathrm{gr}})g\cos\theta\right]\delta R = S\delta R \tag{7.2}$$

To aid calculations, the term in square brackets is defined as the stability parameter, S:

$$S = S_\mu + S_\rho = \Big((\mu_b(\dot{\gamma}) - \mu_{\text{gr}}(\dot{\gamma})\Big)\frac{U}{k} + (\rho_b - \rho_{\text{gr}})g\cos\theta \tag{7.3}$$

where S_μ and S_ρ represent the viscosity and density-controlled components respectively.

Bentonite and grout both exhibit non-Newtonian behaviour, such that μ is expressed as a function of shear rate ($\dot{\gamma}$) in Equations 7.2 and 7.3. This approach aligns with previous studies investigating VF (e.g. Coussot, 1999; Lindner et al., 2000; Azaiez & Singh, 2002; Kim & Choi, 2011; Shokri et al., 2017; Jangir et al., 2022). The Sisko model (Equation 2.3), which effectively captures the behaviour of bentonite (Li et al., 2016), can be rewritten in terms of μ:

$$\mu(\dot{\gamma}) = \frac{\tau}{\dot{\gamma}} = \mu_\infty + K\dot{\gamma}^{n-1} \tag{7.4}$$

where μ_∞, K, and n are curve-fitting parameters, which can be determined using appropriate rheological testing.

The Sisko rheological model can be incorporated into the grout injection model by substituting Equation 7.4 into Equation 7.3:

$$S_\mu = \left(\mu_{\infty,b} + K_b\dot{\gamma}^{n_b-1} - \mu_{\infty,\text{gr}} - K_{\text{gr}}\dot{\gamma}^{n_{\text{gr}}-1}\right)\frac{U}{k} \tag{7.5}$$

Grout injection into a planar annulus (as defined in Figure 7.1) is analogous to a Hele-Shaw cell (see Figure 2.10). For classical VF analysis in Hele-Shaw cells, shear rate is commonly approximated using $\dot{\gamma} \approx U/b_c$, where b_c is the depth of the cell (e.g. Lindner et al., 2000; Azaiez & Singh, 2002; Jangir et al., 2022). Applied to grout injection, b_c equates to the annulus depth (b_a). U is the characteristic injection velocity, which can be approximated as $U \approx q/R$ (Homsy, 1987), where q represents the flow rate of grout per unit depth (i.e. $q = Q/b_a$). Combining these relations, it can be shown $\dot{\gamma} \approx Q/Rb_a^2$. Finally, k can be demonstrated to be $k = b_a^2/12$ (see Section 2.5.3). Combining these relations and Equation 7.5, S is derived in terms of Q, R, b_a and θ:

$$S = S_\mu + S_\rho = \left(\mu_{\infty,b} + K_b\left(\frac{Q}{Rb_a^2}\right)^{n_b-1} - \mu_{\infty,\text{gr}} - K_{\text{gr}}\left(\frac{Q}{Rb_a^2}\right)^{n_{\text{gr}}-1}\right)\frac{12Q}{Rb_a^3} + (\rho_b - \rho_{\text{gr}})g\cos\theta \tag{7.6}$$

In classical VF analysis, the system is considered stable if $S < 0$ and unstable if $S > 0$ (Homsy, 1987). Whilst stability could theoretically be achieved by making the grout more viscous than the bentonite, the selection of bentonite and grout is typically governed by practical

constraints on-site, often resulting in viscosities that exceed this stability criterion. The extent of instability is expected to increase progressively with rising S values. Therefore, minimising S should remain a critical priority, even during injection scenarios that are intrinsically unstable.

7.2.3 Model Validation

In this section, the experimental data from Chapter 5 is used to evaluate the suitability of Equation 7.6 for predicting the uniformity of grout spread. Firstly, the Sisko model parameters (see Equation 7.4) for each fluid were determined through non-linear least squares regression of the rheological data presented in Figure 5.3. The results are summarized in Table 7.1. The resulting viscosities are plotted against the measured data in Figure 7.2, demonstrating good agreement. The bentonite is more viscous than the grout at all shear rates. Considering Equation 7.6, this means $S_\mu > 0$ in all cases, confirming viscosity has a destabilising effect.

Table 7.1: Sisko coefficients for modelling the three fluids used (see Equation 7.4).

Mixture	μ_∞ **(Pa·s)**	**K**	**n**
Baseline Bentonite Slurry (16:1)	-0.11	40.632	0.112
High Viscosity Bentonite Slurry (12:1)	-1.02	83.361	0.249
Grout	-0.65	6.426	0.573

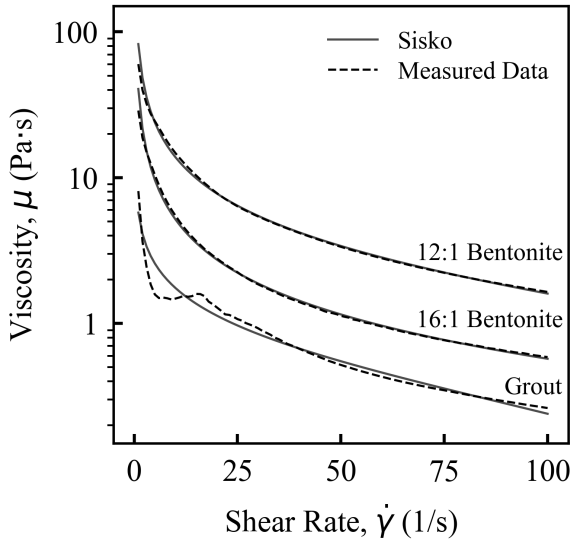


Figure 7.2: Measured viscosity data (reproduced from Figure 5.3b, excluding the error bars), compared to viscosity as predicted by the Sisko model using the coefficients from Table 7.1.

As per the problem definition in Figure 7.1, grout flow is assumed to be radial, with the direction of flow at a given point on the grout profile defined by θ. Since $\rho_g > \rho_b$ (Table 5.1), Equation 7.6 indicates that flow with an upwards component (i.e. $-90° < \theta < 90°$) will always lead to a negative S_ρ, thereby having a stabilising effect. Given the typical injection point is near the bottom of the annulus (Figure 2.2), downward grout displacement is negligible. Thus, to examine the practical limiting case where instability is most likely, this section focuses on horizontal displacement ($\theta = 90°$), where the stabilising influence of density is absent.

Other input parameters required for calculations using Equation 7.6 include b_a, Q, and R. The annulus depth (b_a) is 20 mm for the present apparatus (Figure 5.1b), whilst the flow rate (Q) for each test is in Table 5.3. Since $S_\mu \propto 1/R$ (Equation 7.6), the highest and most unstable S value is expected when R is minimised. Calculations were therefore performed using the internal radius of the grout inlet pipe, $R = 9.5$ mm (Figure 5.1a), which represents the initial and smallest extent of the grout profile. This approach is supported by the qualitative observations in Section 5.6.1, which indicate that the approximate profile of the grout is established early during injection and scales proportionally throughout the remainder of the injection process.

Table 7.2 and Figure 7.3 present the results of calculations performed using Equation 7.6. In addition to the calculated S values, the injection flow rate (Q) and final ellipticity (E), which effectively captures the uniformity of grout spread (Section 5.6.2), are also provided for each test in Table 7.2. The model proves effective in capturing relative differences in grout spread. Tests 1–3, characterised by good grout distribution (low E), correspond to lower S values. Test 4 exhibits a significantly higher S value compared to Tests 1–3, reflecting the observed decrease in grout uniformity and the corresponding increase in E. This trend becomes more pronounced in Test 5, where the highest observed S value aligns with the poorest grout distribution (highest E).

These results suggest that the proposed model could form the basis of an approach for ensuring grout injection stability. Such an approach could rely on an adapted stability criterion informed by experimental data. As a preliminary guideline, a conservative criterion of $S < 18$ kN/m^3 is proposed, based on Tests 1–3.

The present calculations focused on the limiting case of $\theta = 90°$, neglecting any stabilising effect of density. Considering the counter case of vertical displacement ($\theta = 0°$), the calculated

Table 7.2: Stability parameter (S) calculations carried out using Equation 7.6 ($b_a = 20$ mm, $R = 9.5$ mm, $\theta = 90°$).

Test Number	Injection Flow Rate, Q (L/s) [Table 5.3]	Stability Parameter, S (kN/m^3) [Eq. 7.6]	Final Grout Profile Ellipticity, E
1	0.155	18.1	0.09
2	0.207	18.0	0.05
3	0.142	18.2	0.18
4	0.006	49.9	0.33
5	0.050	75.3	0.43

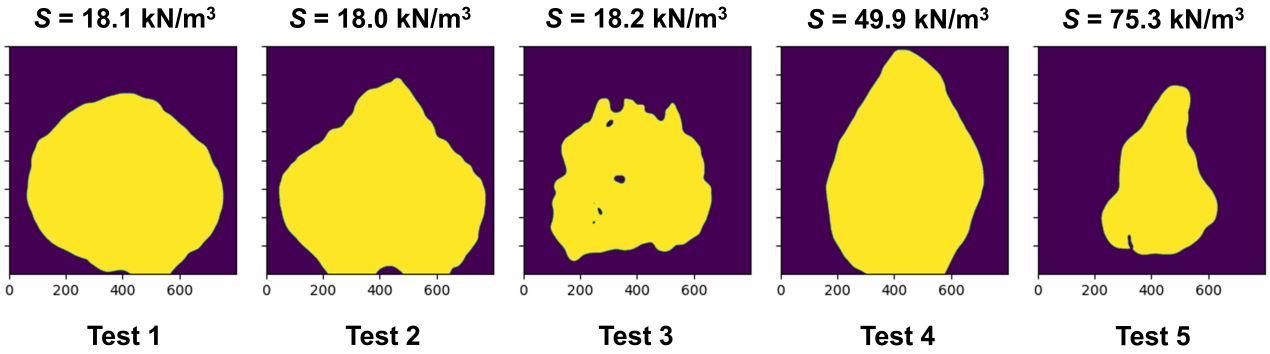


Figure 7.3: Processed images at the end of grout injection for Tests 1-5 and their respective stability parameters (S) calculated in Table 7.2. Axis units in mm.

value for all five tests is $S_\rho(\theta = 0) \approx -3.8$ kN/m^3. Compared to the destabilising S_μ values, which are on the order of 18.0 kN/m^3 and higher, this indicates that density contributes relatively little to increasing stability during vertical displacement.

7.2.4 Limitations

Equation 7.6 captures key factors influencing grout injection. However, the modelling approach does not account for the influence of thixotropy. As observed in Chapter 5, thixotropy appears to only have a transient effect, primarily making the grout profile more irregular in shape, with limited impact on the final grouted area. Consequently, the omission of thixotropy from the model is considered a reasonable assumption.

The sinking phase of a caisson may typically be 2 - 3 months (e.g. Royston et al., 2022b; Willis et al., 2023), meaning significant filtration and/or consolidation of the bentonite will occur, increasing viscosity. To the authors' knowledge, there are no suitable methods available

for estimating the viscosity of bentonite in the annulus under such circumstances. This is a key barrier preventing implementation of the present model in practice and should be a key focus of future work. The model also assumes that the annulus has been successfully maintained. If the annulus collapses, different behaviour may occur. The present experimental results are based on the assumption of simultaneous grout injection from adjacent ports around the caisson (see Section 5.4). Application of the present stability criterion should therefore be limited to such conditions at present.

7.3 Comparison of Grout Injection Results

The most pronounced VF effects observed in Chapter 4 (Test 1) were significantly more severe than those presented in Chapter 5 (Test 5), as illustrated by comparing Figures 4.11a and 5.5e. The primary cause of this difference is likely the higher viscosity of the bentonite in Chapter 4 (Test 1), indicated by the 10:1 water-to-bentonite ratio (see Table 4.3), which is more concentrated than the 12:1 ratio used in Chapter 5 (Test 5). In practice, higher soil stresses may lead to even greater bentonite water loss, highlighting the significant risk that bentonite viscosity increases pose to grout injection.

Additionally, the grout injection port in Chapter 4 had an ID of 12.5 mm (Templeman, 2022), compared to 19 mm in Chapter 5 (chosen to reduce the risk of blockages). Since $S_\mu \propto 1/R$ (Equation 7.6), the smaller port diameter would have resulted in a higher initial S, leading to greater instability during injection. Both experimental setups adopted an annulus depth of $b_a = 20$ mm, so although b_a is a key parameter in Equation 7.6, it is not expected to have influenced the results.

7.4 Implications for Grout Injection On-Site

7.4.1 Injection Flow Rate

Tests 4 and 5 in Chapter 5 both used high-viscosity bentonite (12:1) and the same grout. The variation in S can therefore be solely attributed to the difference in injection flow rates (Q, see Table 7.2), suggesting that controlling Q could be an effective strategy for enhancing grout injection stability. This approach is evaluated using Test 5. Keeping all other parameters in Equation 7.6 constant, achieving the proposed criterion ($S < 18$ kN/m^3) would require

reducing the flow rate to $Q = 4.1$ ml/min. Firstly, such a low flow rate is impractical and may fail to initiate flow, as the yield stress of the bentonite might not be exceeded. Furthermore, the calculated Q is considered unreliable. As Q decreases, the corresponding shear rate also decreases ($\dot{\gamma} \approx Q/Rb^2$). At $Q = 4.1$ ml/min, the calculated shear rate is $\dot{\gamma} = 0.018$ s^{-1}, which is likely too low to be accurately captured by the present rheological data and the associated Sisko modelling (see Figure 7.2). Further investigation is therefore required to fully explore the feasibility of guaranteeing effective grout spread by controlling the injection flow rate. In the meantime, minimising the injection flow rate within practical constraints can increase confidence in achieving good grout coverage.

7.4.2 Bentonite Slurry and Grout Mix Design

The specification of the bentonite slurry is dictated by the requirement for effective lubrication during sinking, which depends on the ground conditions. Recommended water-to-bentonite ratios typically range from 14:1 to 24:1 (Phillips, 2023). At the less viscous end of this range (24:1), stable grout injection may be achieved. However, the results in this thesis suggest that stable injection may be unlikely for more viscous bentonites. Under such conditions, tailoring the grout mix design to increase grout viscosity and density may be desirable. These two factors are likely highly interrelated, and any changes to the grout specification must be carefully considered with respect to 'pump-ability' and curing properties.

7.4.3 Caisson Construction Details

The final parameters that may have influenced grout injection stability in Chapter 5 relate to the geometry of the apparatus: (i) the annulus width, b_a, and (ii) the diameter of the grout inlet hose, which determines the initial value of R used in the calculations in Table 7.2. For the apparatus used in Chapter 5, $b_a = 20$ mm and $R = 9.5$ mm (corresponding to the 19 mm ID of the inlet hose). These dimensions were chosen as a compromise between replicating on-site conditions and addressing practical laboratory constraints. In a recent case study (Royston et al., 2022b), b_a was reported as 70 mm, whilst grout is commonly delivered via 1.5" (38 mm) ID pipelines. Assuming these values, and keeping all other parameters constant, would reduce S to 10.4 kN/m^3 for Test 5, indicating that stability may indeed be achieved. Examining Equation 7.6, this reduction is primarily attributed to the increase in b_a, since $S_\mu \propto 1/b_a^3$. It is therefore

suggested that stability may be ensured in practice by employing a sufficiently large annulus width (b_a).

In addition to tailoring the annulus width, optimisation of the injection system should be considered. Greater grout coverage could be achieved through close spacing of conventional injection ports around the circumference of the caisson and/or greater diameter ports. Alternatively, a more sophisticated distributed delivery system can be employed, such as the design proposed by Templeman (2022) and illustrated in Figure 7.4. In this setup, a perforated steel section encircles the caisson, forming the top of the cutting shoe. When pressurised, lubricant or grout is forced through the perforations, filling the annulus more evenly around the caisson circumference. This delivery method could ensure adequate grout coverage, even if lateral spread from individual injection locations is poor.

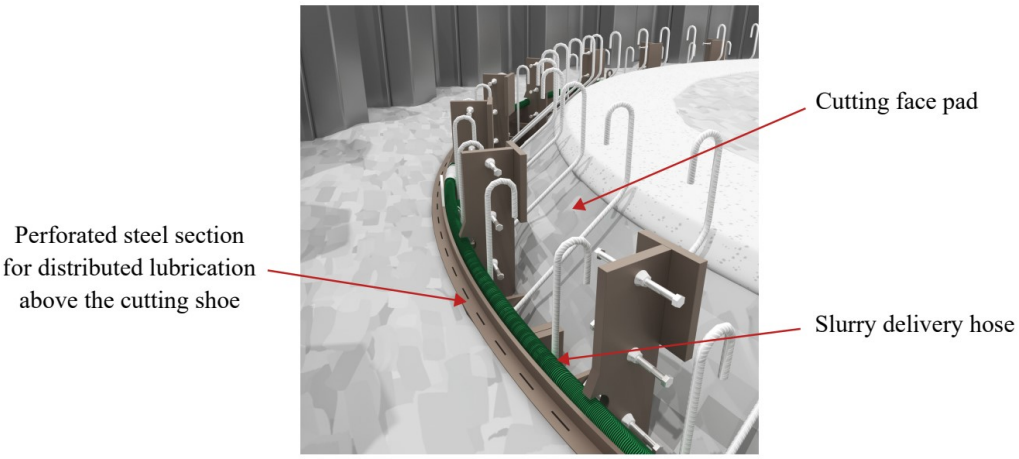


Figure 7.4: System for distributed delivery of lubricant to the annulus above the cutting shoe used by Ward & Burke Construction Ltd (from Templeman, 2022).

7.5 Caisson-Soil Uplift Friction in Sand

7.5.1 Derivation of an Interface Friction Factor (α)

The friction results presented in Section 4.5.1 confirmed that grouting led to an increase in uplift friction and provided insights into the limited influence of bentonite and grout age. However, the total resistance results presented in Figure 4.8 are expressed in terms of absolute force (kN), based on measurements from the load cell during testing. While such measurements are valuable, they offer limited context regarding the extent of friction mobilised and are of limited applicability in practice. This section addresses these limitations by recalculating the uplift

friction, firstly in terms of shear stress (τ, also referred to as skin friction) and subsequently as an interface friction angle (δ). This approach enables the derivation of an operational interface friction factor (α), which can be applied in design.

The total resistance data presented in Figure 4.8 comprise interface friction plus the weight of any adhered grout and filter cake. Hereafter the friction force is isolated from these weights and considered in terms of skin friction. It is not possible to ascertain the exact area over which friction occurred with a high degree of confidence. As such, to calculate the skin friction, the area was estimated using two approaches.

Firstly, the 'best estimate area' (BEA) is used to estimate the actual skin friction as accurately as possible. The BEA is derived by considering the area of the layer of sand which appeared to have moved with the TP during uplift. Test 2 is used as an exemplar in Figure 7.5a. Equivalent analysis was possible for Test 3, but not Test 1 (see Figure 4.9). The BEAs for Tests 2 and 3 are presented in Table 7.3, whilst the subsequent calculated skin friction results are plotted in Figure 7.6a. For the baseline test (no grout), also included in Figure 7.6a, friction was assumed to act over the total area of the interface (500 x 1000 mm).

Secondly, the 'lower bound area' (LBA) provides conservative operational friction values that can be confidently applied in practice. The LBA for Test 2 is indicated in Figure 7.5b. Given the observed failure mechanism (Figure 4.12), where a block of cohered sand moves upwards with the grout and adjacent ungrouted areas, the LBA is considered the absolute maximum feasible area over which friction could have developed (i.e. everywhere above the lowest extent of grout). LBAs were analogously derived for Tests 1 and 3, given in Table 7.3. These areas were used to calculate LB skin friction for Tests 1-3, the results of which are plotted in Figure 7.6b, also alongside the baseline test results.

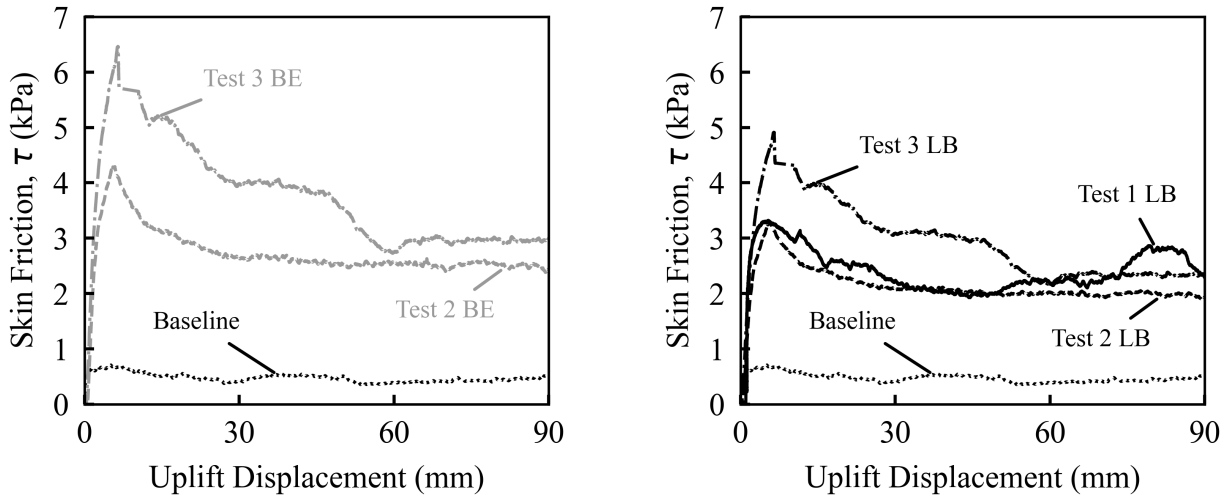
Table 7.3: Areas assumed for the calculation of skin friction; 'best estimates' and 'lower bounds' (see Figure 7.5). Note: the total interface area is 0.5m^2.

	Test 1	**Test 2**	**Test 3**
Best Estimate Area (BEA; m^2)	N/A	0.300	0.320
Lower Bound Area (LBA; m^2)	0.405	0.414	0.435



(a) (b)

Figure 7.5: Excavation results from Test 2 (reproduced from Figures 4.9 and 4.11), with the areas used to calculate uplift friction in terms of stress: (a) the 'best estimate area' (BEA), which is used to closely predict actual friction; and (b) the 'lower bound area' (LBA), which is used to derive conservative operational friction values.



(a) (b)

Figure 7.6: Estimated skin friction (τ) plotted against displacement during uplift for: (a) Tests 2 and 3 using the best estimate (BE) areas in Table 7.3; (b) Tests 1-3 using the lower bound (LB) areas in Table 7.3. Results from the Baseline Test (no grout), considered over the entire interface, are also included on both plots.

The skin friction results were then used to estimate the interface friction angle for Tests 1-3 using the following equation:

$$\tau = K_0 \sigma'_v \tan \delta \tag{7.7}$$

The vertical effective stress (σ'_v) can be simply calculated at the average depth for the given shear area using the dry unit weight of the sand sample (γ_d), providing a representative value. The value assumed for K_0 required careful consideration, as direct measurement of lateral stress at the interface was not possible following grout injection. Templeman (2022), using the same apparatus and sample preparation method, measured $K_0 = 0.91$ during caisson sinking without lubrication or annulus formation (i.e. shearing at a dry sand–concrete interface). This value is significantly higher than the nominal at-rest value of $K_0 = 0.45$. A high K_0 during sinking is consistent with field measurements by Royston et al. (2022b). Three factors may have contributed to the elevated K_0 observed in Templeman's tests:

1. Air pluviation can lead to higher-than-expected lateral stresses, particularly at low vertical stresses (Chu & Gan, 2004; Northcutt & Wijewickreme, 2013). Templeman (2022) identified this as the likely primary cause.

2. Since the measurements were taken during shearing, it is likely that dilation combined with confinement from the surrounding soil also contributed to the increased lateral stress measured at the interface.

3. A high shear rate (25 mm/min) was used by Templeman (2022) to reflect typical field sinking rates. High shear rates have been shown to increase peak strength in sandy soils (e.g. Beren et al., 2020). Higher peak strength implies greater confinement forces and, therefore, higher lateral stresses during dilation, suggesting that the influence of Factor 2 may have been amplified by the high shear rate.

Factors 1 and 2 remain unchanged in the present testing, whilst the influence of Factor 3 may be reduced due to the lower shear rate used in uplift (1 mm/min). In the absence of a reliable method to estimate this reduction or directly measure lateral stress, a value of $K_0 = 0.91$ is adopted in the present calculations as a balance between representing actual conditions and ensuring conservative prediction of δ.

Results from the calculations using the results from Figure 7.6 and Equation 7.7 are plotted in Figure 7.7. Skin friction can be generalised by considering the interface roughness factor,

α (Equation 6.1). The BE predictions, which sought to faithfully estimate the shear area, are presented in Figure 7.7a, resulting in $\alpha = 0.88$ (Test 2) and $\alpha = 0.95$ (Test 3). These results provide inferential evidence that $\delta \approx \phi$, in keeping with the observed failure plane within the sand. The LB friction results, which sought to provide operational friction data for application in practice, are plotted in Figure 7.7b. The minimum interface friction angle calculated, $\delta_{min} = 17.3°$, is used to suggest a conservative design value of $\alpha = 0.48$ for use in similar soil conditions. Pending further investigation in a range of soil conditions, it is envisaged empirical values such as this, used in tandem with an estimated area, could form the basis of a generalised simplified design method.

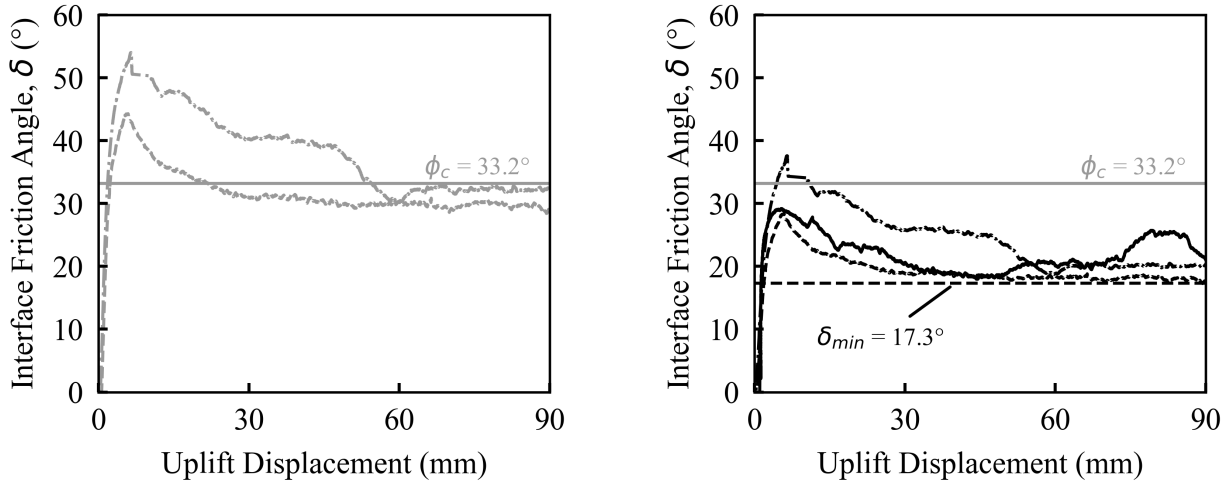


Figure 7.7: Development of the estimated interface friction angle (δ) for: (a) Tests 2 and 3 using the BE skin friction from Figure 7.6a; and (b) Tests 1-3 using LB skin friction from Figure 7.6b. Both plots include the critical state friction angle of the sand (ϕ_c). Plot (b) also contains the minimum calculated friction value (δ_{min}).

7.5.2 Experimental Comparisons to Bored Pile Construction

Key similarities and differences between caisson construction and bored pile construction were described in Table 7.4. Whilst there are some differences between the processes, the similarities are pertinent, justifying comparison. To that end, two recent experimental studies investigating the shear strength of concrete-soil interfaces were identified, based on their similarity to the present testing (Lam et al., 2014; Verst et al., 2022). Within those studies, the tests used for comparison were limited to those using concrete with fine aggregates, similar to grout.

Table 7.4: Pertinent similarities and differences between grout injection and bored pile construction.

Similarities	Differences
(i) Bentonite commonly used to provide support to soil prior to grouting/concreting.	**(i)** The use of grout instead of concrete (which contains larger aggregates and is likely denser).
(ii) Concrete placed using the tremie method in bored piling displaces bentonite upwards, analogous to grout displacing bentonite to the surface in the annulus during caisson construction.	**(ii)** Potential partial coverage at the caisson-grout-soil interface due to VF, compared to complete concrete coverage at the pile-soil interface.
(iii) Both piles and caissons rely on engagement of skin friction at the interface following prolonged soil exposure to support fluid and subsequent grouting/concreting.	**(iii)** The typical maximum exposure time of the soil to the support fluid is up to 12 hours in pile construction (ICE, 2017), compared to potentially 2 - 3 months for caisson construction (Royston et al., 2022b; Willis et al., 2023).
(iv) Both concrete (piles) and grout (caissons) placed and cured in situ, in contact with the soil body.	**(iv)** The formation of a bond between the grout and concrete caisson, rather than one continuous body of concrete (piles).

Table 7.5 presents the comparison between results from those studies and the present testing, demonstrating a broad range of α values, despite the tests being similar in nature. Lam et al. (2014) recorded much lower interface friction, whilst Verst et al. (2022) reported values within the inferred ranges in this chapter. The most notable difference in Table 7.5 is the occurrence of the failure plane within the sand for the present study, compared to within the filter cake in Lam et al. (2014) and Verst et al. (2022). When applied to caisson construction, the additional benefit of friction being independent of grout coverage (Figure 4.12) may be lost if failure occurs within the external filter cake. The studies described in Lam et al. (2014) and Verst et al. (2022) were carried out using an apparatus similar to a conventional direct shear apparatus. Both studies were set up such that the filter cake-concrete boundary coincided with the plane of the shear box. As a result, it is possible that the failure surface was forced to occur close to the interface during shearing. In contrast, the apparatus used in Chapter 4 allows unrestricted self-determination of the shear plane.

Particle size distribution is well documented as the main factor influencing filter cake formation (see Section 2.5.2). Whilst all three studies in Table 7.5 noted internal filter cake

Table 7.5: Pertinent features and results of the present testing and analogous experimental literature on bored pile construction.

Author	**Test Number***	**Sand**	**Particle Size Distribution** d_{10}, d_{30}, d_{60} (mm)	**Inferred Interface Roughness** α	**Failure Plane**
Lam et al. (2014)	Test 9	Thanet sand (saturated)	0.07, 0.10, 0.14	0.15	In external filter cake
Verst et al. (2022)	V-B-01 V-B-02 V-B-03 V-B-04 V-B-06	Medium sand (dry)	0.27, 0.42, 0.63	0.60-0.71	In filter cake**
Present Study	Test 1 Test 2 Test 3	Leighton Buzzard 14/25 (dry)	0.65, 0.77, 0.95	0.48-0.95	In sand

*as defined in the relevant study
**exact location unclear - appears to be approximately at the internal-external filter cake boundary

formation, it is expected infiltration is more significant in the present testing and Verst et al. (2022) due to the larger sand particles. For the present testing, this likely led to limited external filter cake formation and increased cohesion in the internal filter cake, promoting the failure mechanism in Figure 4.12. Verst et al. (2022) also recorded higher friction compared to Lam et al. (2014), although the failure plane was observed within the filter cake, not the sand. Overall, the present comparison suggests that frictional resistance is strongly influenced by the soil particle size distribution and the resulting filter cake composition. Coarser sand promotes greater bentonite infiltration, which subsequently increases friction. Additionally, the use of dry sand in Verst et al. (2022) and the present testing may have influenced the results when compared to the saturated conditions used in Lam et al. (2014). Further investigation into behaviour across a range of particle sizes and saturation conditions is warranted to develop a more generalised prescriptive design approach. The application of the present friction factor ($\alpha = 0.48$) should be constrained to coarse sands.

Polymer fluids are widely used as support fluids in bored pile construction, however, their

use as construction 'lubricants' remains limited at present. Both Lam et al. (2014) and Verst et al. (2022) found that the use of polymer fluids led to little reduction in friction relative to a standard concrete-sand interface. In both cases, the failure plane was observed within the sand body, leading to high friction (α = 0.85 - 1). This suggests the use of polymer fluids may also be prudent for maximising friction in uplift, especially in finer sands.

7.5.3 Application of Existing Bored Pile Research to Caisson Uplift Design

To further consider the circumstances under which such research could be applied to caisson construction, the contributions of this thesis and the existing literature are evaluated in the context of the key differences between the two construction processes outlined in Table 7.4:

- **Difference (i):** Only literature employing grout or 'microconcrete' (which does not contain large aggregates) should be considered. This is critical, as Lam et al. (2014) demonstrated that the protrusion of large aggregates into the filter cake can significantly influence frictional capacity.

- **Difference (ii):** The analysis presented in Section 7.2 can be utilised to ensure uniform grout coverage.

- **Difference (iii):** Bored pile literature indicates that frictional resistance decreases with increasing soil exposure time to bentonite until a limiting minimum is reached. The time required to reach this minimum can range from 12 hours to 14 days (e.g. Littlechild & Plumridge, 1998; Thasnanipan et al., 1998; Ng & Lei, 2003; Lam et al., 2014). Since typical soil exposure times during caisson sinking are universally longer than those considered in bored pile construction, only the highest available exposure times, and thus the minimum possible friction values, should be considered for conservative caisson uplift design.

- **Difference (iv):** The present results suggest that a sufficient bond forms between the caisson and the grout, facilitating a failure plane either within the filter cake or sand.

Lam et al. (2014), who conducted a comprehensive review of prior studies, provides a valuable reference point for experimentally verified friction values. Some of the studies detailed in Lam et al. (2014) employed low diameter model piles; the results from these studies should be

applied cautiously to larger diameter caissons. Preference should be given to research utilising shear box-type testing for more representative results. Overall, the comparison between the present findings and bored pile research suggests that the application of bored pile literature to caisson uplift design may be appropriate, provided comparable soil conditions are ensured and the constraints discussed in this section are carefully considered.

7.6 Design of Under-Reamed Caissons in Sand

In Chapter 6, the SLS results for inclined anchors suggested the influence of β and α on $N_g/N_{g,\beta=0}$ was independent of soil type, H/b, and I_{d0} (Figure 6.15). Using all the data points from Figure 6.15, the maximum, average, and minimum $N_g/N_{g,\beta=0}$ observed at each β for $\alpha = 0.05$ and $\alpha = 1$ are plotted in Figure 7.8 (i.e., lumping together all H/b, I_{d0}, and soil types). For each value of α, all results lie within a narrow band, confirming the influence of β and α are relatively independent of soil type, normalised depth (H/b), and initial density (I_{d0}).

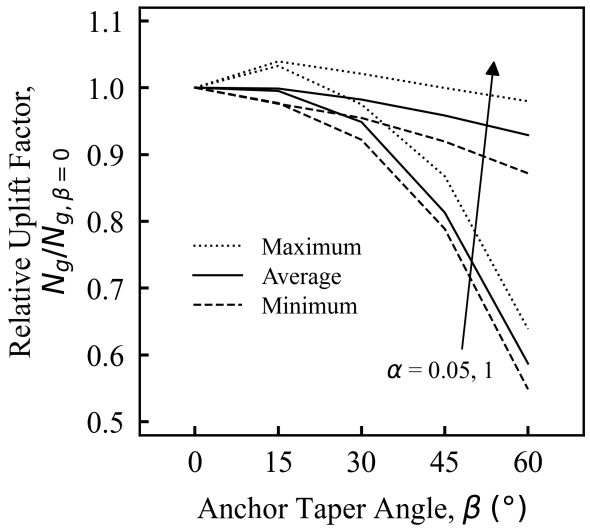


Figure 7.8: The maximum, average, and minimum relative SLS uplift factors for $\alpha = 0.05$ and $\alpha = 1$ (both soils, all H/b, both I_{d0}).

The relationship between N_g and $N_{g,\beta=0}$ is therefore used to develop a chart to aid the design process in practice. For clarity, and a conservative bias, Figure 7.9 plots only the minimum observed value at each β for the given α. To use Figure 7.9, the engineer should first carry out calculations, using FEA or otherwise, to predict the SLS flat anchor resistance ($N_{g,\beta=0}$) for a practical range of b values (in a practical design case, the soil, I_{d0}, and H will be predefined). Figure 7.9 can then be used to estimate the expected resistance at various values of β and α

based on the $N_{g,\beta=0}$ results. The chart is designed to streamline the preliminary design process by reducing the computational demand associated with conducting numerous analyses, thereby facilitating design optimisation. Site-specific modelling considering the chosen anchor geometry should be used to analyse any final design.

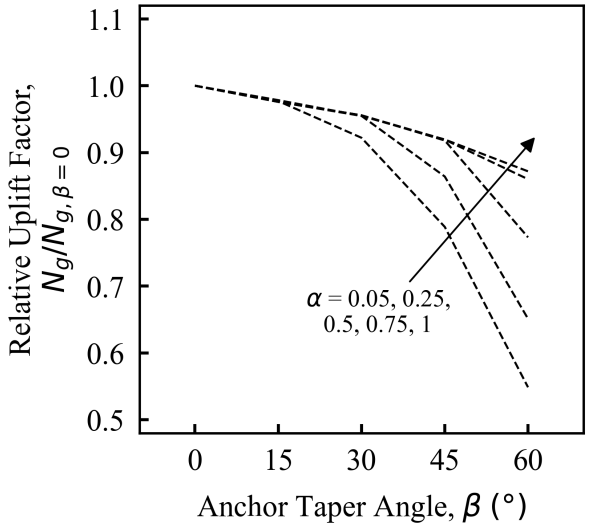


Figure 7.9: A design chart for estimating tapered anchor uplift resistance, given prior knowledge of the equivalent flat anchor resistance. Based on the minimum SLS uplift resistance factors calculated at each β for the respective α (both soils, all H/b, both I_{d0}).

7.7 Reducing Embodied Carbon

7.7.1 Microtunnelling vs Open-Cut Pipeline Installation

To provide a basis for comparison, the total EC results for each case study evaluated in Chapter 3 are presented in Table 7.6 and Figure 7.10, normalised by the internal volume of tunnel space created. The results are compared to those produced by Alsadi & Matthews (2020), which considered OCI. No suitable MT studies were identified in the literature. Regarding comparable pipeline literature, six studies were identified which consider emissions from both material manufacture and construction operations. Five studies were excluded (Piratla et al., 2012; Khan & Tee, 2015; Chilana et al., 2016; Kyung et al., 2017; Matar et al., 2019) due to the use of outdated metrics (i.e. EE) and/or the consideration pipelines of diameter <600 mm, the typical minimum for MT (Phillips, 2023).

Comparison of the present results to Alsadi & Matthews (2020) suggests MT is a good solution with respect to EC. CS1 and CS2 provide the best comparison, as their depths are

Table 7.6: Summary of EC results (modules A1-A5 inclusive) normalised by the internal volume of tunnel/pipeline for the present case studies, alongside results from Alsadi & Matthews (2020) for a comparable pipeline constructed using OCI. OCI = Open Cut Installation, RC = Reinforced Concrete, PCCP = Prestressed Concrete Cylinder Pipe.

	Case Study 1	**Case Study 2**	**Case Study 3**	**Alsadi & Matthews (2020)**
Excavation Method	MT	MT	MT	OCI
Pipeline Material	RC	RC	RC	PCCP
Total Length (m)	360	459	51	122
Number of Shafts	4	3	2	N/A
Cover to Pipe Crown (m)	2.23 - 3.36	1.74 - 2.15	5.51 - 6.06	1.38
Internal Diameter (m)	1.2	1.2/1.5	1.2	0.76
Pipeline(s) EC ($kgCO_2e/m^3$)	598.0	530.6	727.1	985.9
Shafts EC ($kgCO_2e/m^3$)	330.0	193.8	1525.8	N/A
Total ($kgCO_2e/m^3$)	928.0	724.4	2253.0	985.9

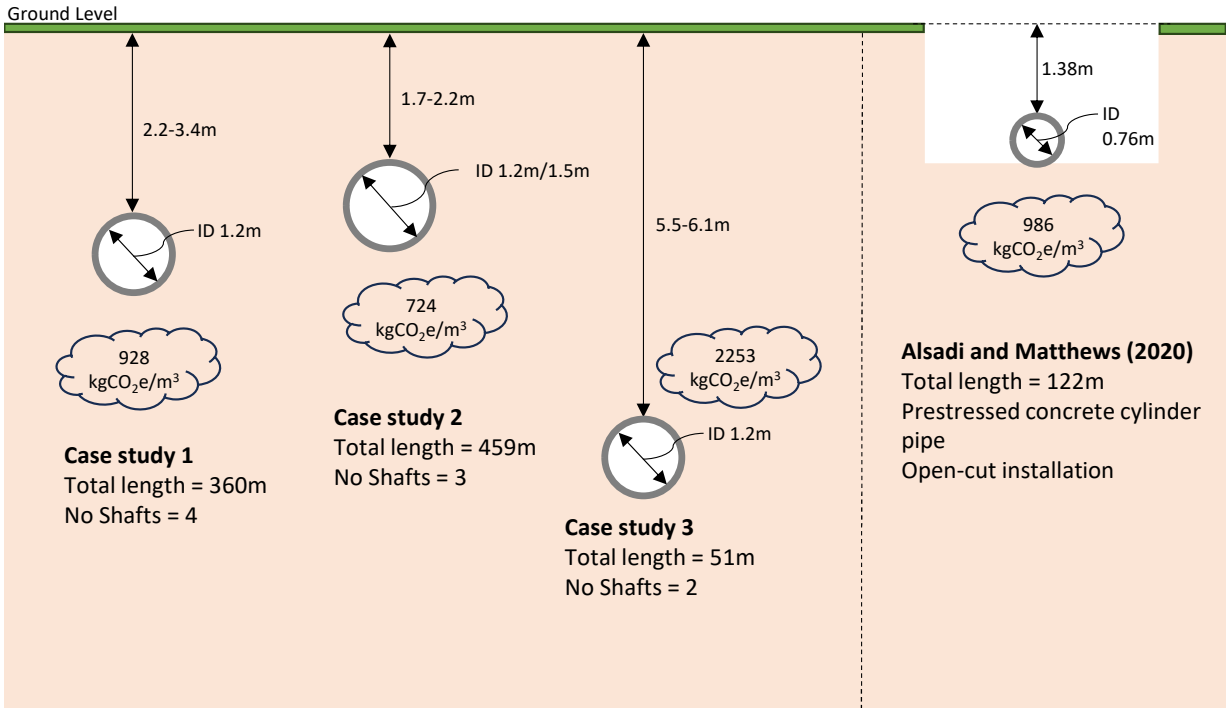


Figure 7.10: A schematic illustration of the normalised Total EC results from Table 7.6.

most similar to that of Alsadi & Matthews (2020). In both cases, CO_2e per unit pipeline volume is lower than the quoted OCI results, despite that pipeline being constructed at a shallower depth (see Table 7.6 and Figure 7.10). However, the present values could have been influenced by having a larger diameter and greater lengths than Alsadi & Matthews (2020). Further investigation is warranted to enable objective comparison of the construction methods. It is also worth noting the present comparison does not consider the additional benefit of reduced road closures from MT, which can lead to further reductions in emissions.

CS3 results in significantly higher EC per unit pipeline volume, mainly due to the greater cover necessitating deep shafts (see Figure 3.9), giving the high shaft EC in Table 7.6. CS3 also has a higher EC for the pipeline, which is mainly due to the significantly higher A5 emissions observed during tunnelling (see 'T3' in Figure 3.12). CS2 has the lowest normalised EC in Table 7.6, mainly due to the high tunnel length to shaft ratio, which reduces the relative impact of the shafts per unit pipeline volume. This demonstrates a key benefit of increasing MT drive lengths, which enables the elimination of intermediate shafts.

7.7.2 Minimising Shafts in Microtunnelling

CS1 (Section 3.4) required the sewer network to be diverted in 2 locations to enable roadworks. High-level design optimisation of CS1 before construction allowed for retrospective analysis of the impact of the design changes on the project's EC. The preliminary design for CS1 involved two launch shafts, four reception shafts, and four 1.2 m ID tunnels of lengths 18, 117, 51 and 111 m (Figure 7.11). This design centred around making use of 129 m of existing sewer, which meant that the final optimised design, which connects to the existing sewage network in a different location, increased the length of new tunnels by 21% (from 297 to 360 m). The design optimisation focused on achieving a reduction in the number of shafts.

To enable a like-for-like comparison, the shafts with the most similar depth from the final design for each respective location were considered (see Figure 7.11). Shaft diameter is determined by the space required for jacking equipment and insertion/removal of the TBM, which are, in turn, controlled by the tunnel diameter. As the tunnels in the preliminary and final designs had the same diameter, it is assumed that the shafts also had the same diameter in the preliminary design. Since the shafts are the same as those considered in the original

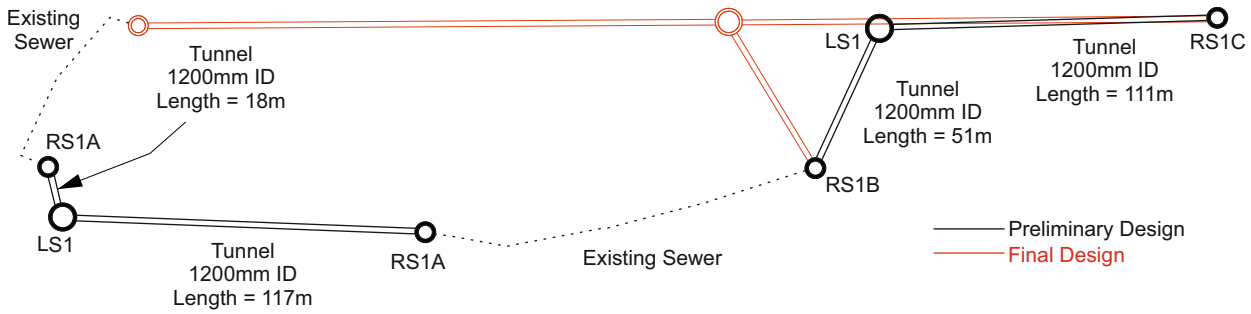


Figure 7.11: CS1 preliminary site layout with labels indicating the shafts from the CS1 final design that were assumed at each preliminary shaft location.

analysis (Section 3.4), the inputs used are the same as those shown in Table 3.5 and Table 3.6. New inputs required are shown in Table 7.7. The diesel values are estimated based on diesel consumption per metre tunnelled for the three tunnels constructed for the final design. All other inputs in Table 7.7 are derived using the tunnel lengths and assuming the tunnels are constructed using the same jacking pipes as the final design.

Table 7.7: Case study 1 preliminary design tunnel inputs. Shaft inputs are assumed to be the same as the final design (see Figure 7.11).

Input	**Unit**	**18 m 1200ID**	**117 m 1200ID**	**51 m 1200ID**	**111 m 1200ID**
Steel Plate Fabrication	kg/m^3	61.7	61.7	61.7	61.7
Reinforcing Steel	kg/m^3	153.5	153.5	153.5	153.5
Total Concrete Volume	m^3	11.0	71.7	31.2	68.0
Diesel Volume	l	2061	5038	3053	4858
Volume Excavated Material	kg/m^3	31.4	204.0	88.9	193.5

The resulting A1-A5 EC for the preliminary design is compared with the calculations for the optimised design in Figures 7.12 and 7.13. A1-A4 emissions increase linearly with tunnel length given the similarity in the pipes used. The difference between the increase in tunnel length (21%) and increase in tunnel EC (16.6%) is therefore exclusively due to A5 emissions. This can be explained by mobilisation and demobilisation being a fixed diesel cost, and hence the increased number of drives for the preliminary design increases the relative A5 contribution. Despite the increase in length of the more carbon-intensive tunnels, the reduced number of shafts led to an overall EC reduction. The elimination of the second launch shaft makes the most significant contribution, accounting for 70.5% of the reduction in the EC of the shafts. The

overall reduction of 52 tCO_2e highlights the significant environmental benefits of minimising the number of tunnel drives and shafts.

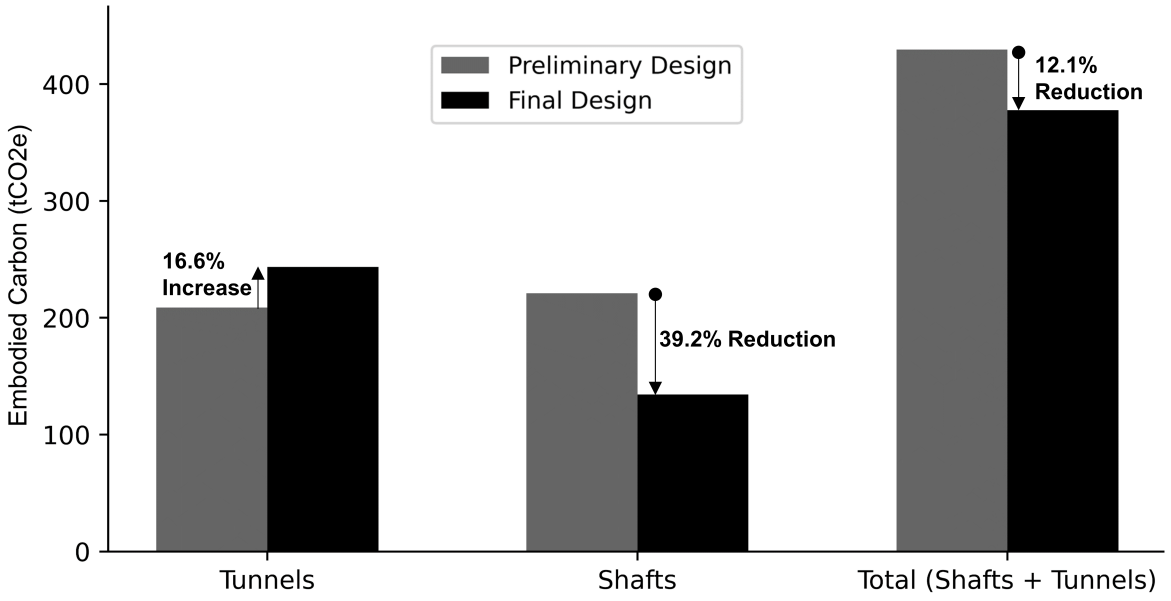


Figure 7.12: A comparison of the EC from modules A1-A5 for tunnels and shafts in CS1 for the preliminary and final designs.

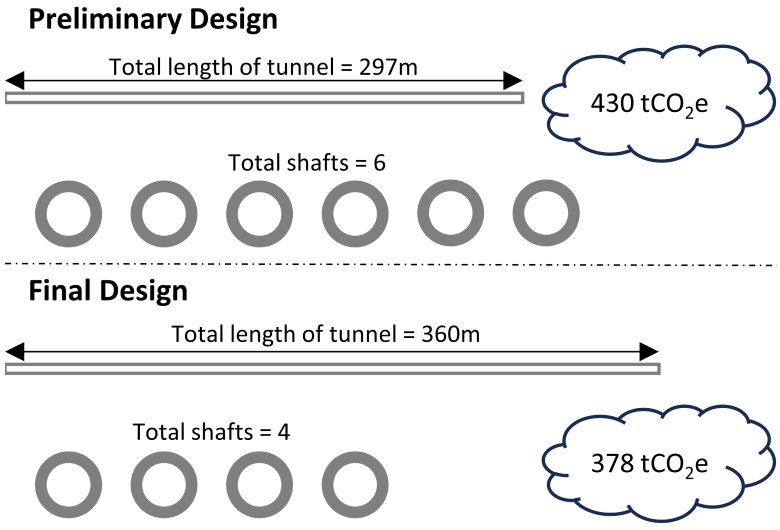


Figure 7.13: A schematic visualisation of the change in tunnel length and the EC savings enabled by the reduction in the number of shafts in CS1.

7.7.3 Construction Materials

Concrete

In Chapter 3, production of materials and components (Modules A1-A3) was shown to account for 68.5% of the EC across the three case studies, with the majority of these emissions

arising from concrete production. Different concrete mixes can vary significantly in EC, primarily due to differences in cement content, the most carbon-intensive component of concrete. The primary method for reducing the EC of concrete at present is the use of secondary cementitious materials (SCMs), such as ground granulated blast-furnace slag (GGBS) and fly ash. These materials can replace a portion of the cement in the mix and typically have a significantly lower ECF (see Table 3.3). Concrete mix design must account for structural, durability, and constructability requirements, as well as material availability. The latter poses a significant challenge, as nearly all locally available low-EC SCMs are already utilised in the UK and EU. Consequently, specifying a low-carbon concrete mix design for one project may simply shift carbon emissions onto another project, rather than achieving an overall reduction. All available low-carbon SCMs should be utilised; however, given their limited availability, their use should be prioritised for the most suitable projects (ICE, 2022). Given these constraints and the complexity of concrete specification, the exploration of alternative concrete mix designs falls beyond the scope of this thesis. For further information on low-carbon concrete design, refer to ICE (2022).

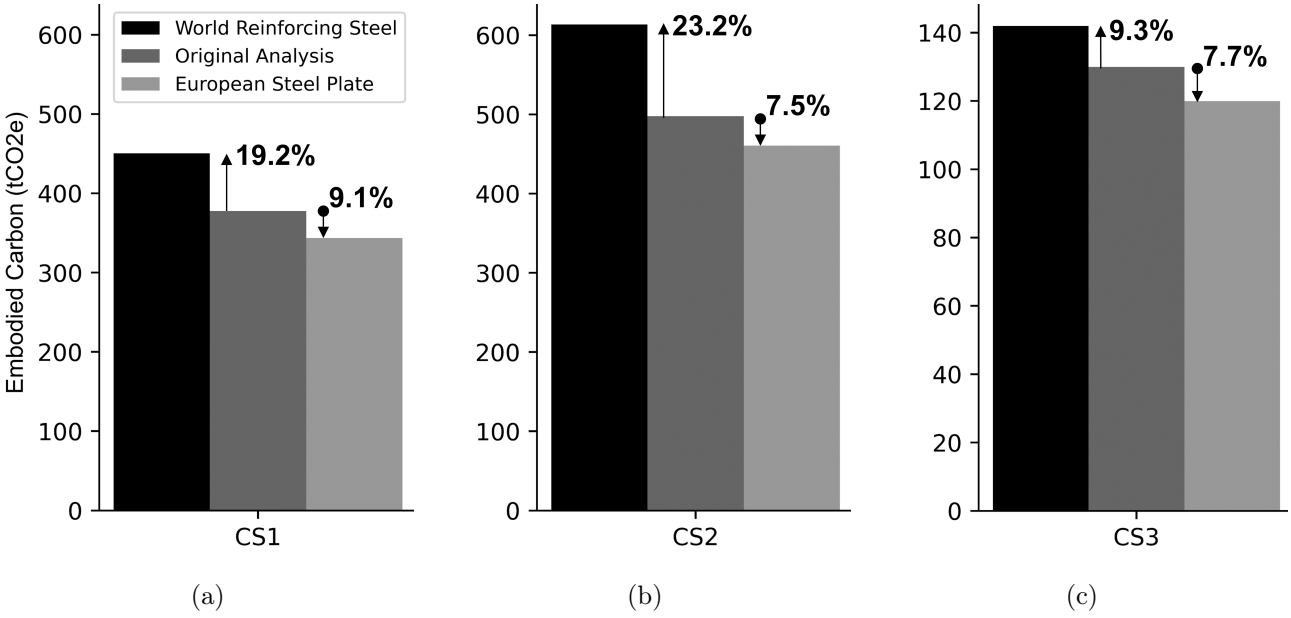
Steel

Steel also made a significant contribution to the A1-A3 EC of the MT case studies in Chapter 3. The EC contribution of the reinforcing steel (13.7% for CS1, 15.9% for CS2, and 5.76% for CS3) was lower than that of the fabricated steel (24.7% for CS1, 19.6% for CS2, and 18.5% for CS3). This is despite typically higher quantities of reinforcement (see Tables 3.6, 3.7, and 3.9). The difference in contributions is therefore solely explained by the difference in ECFs in Table 3.3 (0.655 $kgCO_2e/kg$ for the electric arc furnace produced reinforcement compared to 2.46 $kgCO_2e/kg$ for the basic oxygen furnace produced steel plate).

To explore the impact of the manufacturing process and the source of steel products, a sensitivity analysis was carried out exploring two alternative scenarios: (1) a worst-case scenario, where the world average reinforcing steel ECF is adopted; and (2) a best-case scenario, where a European produced steel plate ECF is adopted (see Table 7.8). Figure 7.14 presents the results of the sensitivity analysis for each case study in terms of A1-A5 emissions. The worst- and best-case scenarios led to an increase of 200.2 tCO_2e (19.9%) and decrease of 81.4 tCO_2e (8.1%) in total across the three case studies (respectively).

Table 7.8: Embodied Carbon Factors (ECFs) used to carry out sensitivity analysis.

Material/ Process	**ECF**	**Unit**	**Source**
Reinforcing Steel	1.99	$kgCO_2e/kg$	Average for world steel - ICE Database (Jones & Hammond, 2019)
Steel plate fabrication	1.13	$kgCO_2e/kg$	European steel plate - IStructE (2020). Value shown increased by 10% in analysis to account for fabrication (Gervasio & Dimova, 2018)



(a) (b) (c)

Figure 7.14: Sensitivity analysis comparing the EC results of the original study in Chapter 3 ('Original Analysis') with the equivalent results using: (1) the ECF representative of the world average for reinforcing steel; and (2) the ECF representative of European produced steel plate. Results presented represent modules A1–A5 for (a) CS1; (b) CS2; and (c) CS3. (c) is plotted on a different scale for clarity.

The world average ECF captures more basic oxygen furnace steel, whilst the European ECF encapsulates more electric arc furnace steel. Electric arc furnace steel production relies predominantly on recycled steel as feedstock. However, production using this method cannot meet total global steel demand (Watari et al., 2023). Whilst electric arc furnace steel production should be maximised and the steel it produces fully utilised, simply opting for 'lower-carbon' steel on one project may merely shift the EC burden to another project, without reducing overall emissions. The results of this analysis therefore do not necessarily advocate for selecting different types of steel on a project-by-project basis. Instead, they highlight the need to globally reduce reliance on basic oxygen furnace steel production to achieve meaningful emission reductions.

The Path to Net Zero

SCMs in concrete and electric arc furnace steel will both contribute to reduced carbon emissions in the short to medium term, but cannot provide a pathway to net zero on their own. With sustained demand for the materials and a lack of viable, scalable alternatives at present, global reliance on traditional cement production and basic oxygen furnace steel production appear set to continue for the foreseeable future. Both processes produce significant emissions due to: (1) their reliance on fossil fuel energy; and (2) the inherent production of CO_2 through chemical reactions. Addressing (1) will require full electrification of the processes and decarbonisation of the electricity grid, or the adoption of renewable biofuels. Tackling (2) will necessitate innovations in the chemistry of material production. Whilst progress is being made in these areas, the required technologies remain decades away from full maturity. Given the significant challenges involved, material efficiency will be critical in facilitating the path to net zero (ICE, 2022; Gates, 2022; Conway, 2023). To this end, this thesis enables substantial material savings and therefore significant EC reductions in MT and caisson construction.

7.7.4 Caisson Material Savings

To explore the potential material savings enabled by the methods proposed in this thesis, a realistic caisson case study is examined. The case study considers a caisson with an OD of 20 m (e.g. Abdrabbo & Gaaver, 2012) embedded to a depth of $H = 12$ m in Soil 1 from Chapter 6 (Table 6.1), assuming dense conditions ($I_{d0} = 90\%$). To quantify the potential uplift resistance provided by under-reaming, an anchor with $b = 1$ m is considered, based on the results from Section 6.6.3. Following the guidance in Section 6.6.3, a low anchor taper angle ($\beta = 15°$) is selected to maximise N_g and minimise the influence of α. Such an anchor is estimated to provide 28.8 MN of uplift resistance. The potential contribution of friction to uplift resistance is evaluated using the recommendations outlined in Section 7.5.1. Using the soil parameters $\phi_c = 31.5°$ and $\gamma' = \gamma_d = 20\text{kN/m}^3$, plus assuming a value of $K_0 = 0.5$ (conservative) and $\alpha = 0.48$ (Section 7.5.1), Equations 6.1 and 7.7 can be applied to calculate potential total uplift friction as 13.3 MN.

Combined, the proposed anchor and calculated friction could provide a total uplift resistance of 42.1 MN, sufficient to counteract the maximum possible uplift force of 37.0 MN (assuming

the phreatic surface is at ground level). Caisson design in the permanent state is often driven by the need for sufficient weight to resist uplift. The present analysis suggests that the caisson weight could instead be determined by sinking and structural requirements alone, potentially resulting in substantial material and EC savings.

7.8 Summary

This chapter explored the application of the results presented in this thesis, developing new design methods and providing recommendations for improved construction practices. A theoretical model was developed to predict the stability of grout injection, and hence the likelihood of uniform grout spread. The model was validated using the results from Chapter 5, demonstrating its ability to effectively capture observed behaviour. Comparisons were then made between the grout injection behaviour observed in Chapter 4 and Chapter 5. This was followed by a discussion of potential remedial measures to improve grout injection on-site.

Friction measurements from the uplift experiments (Chapter 4) were used to derive an interface roughness factor for design use. Comparisons to literature on bored pile construction suggest that the application of this friction factor should be limited to coarse sands. More broadly, those comparisons suggest the use of bored pile literature in caisson uplift design may be appropriate, provided that comparable soil conditions are ensured and the constraints outlined in Section 7.5.3 are considered.

Using the numerical results from Chapter 6, a design chart was developed to streamline preliminary design of under-reamed caissons. The EC findings from Chapter 3 were compared with relevant literature, suggesting that MT projects have lower EC than comparable OCI projects. An analysis of one case study's design history showed how minimising the number of intermediate shafts through effective high-level design decisions can significantly reduce EC in MT. A discussion on the EC of construction materials underscored the urgent need for material efficiency and innovation in material production methods. Finally, a realistic caisson case study verified that the uplift friction results (Chapter 4) and the under-reaming results (Chapter 6) have the potential to reduce carbon emissions by reducing reliance on caisson self-weight.

8 Conclusions

8.1 Introduction

This thesis has presented a body of research aimed at reducing carbon emissions associated with underground construction, with a specific focus on MT and the construction of open caisson shafts. The work began with an EC analysis of three UK MT projects, providing detailed insights into the primary contributors to emissions. The remainder of the thesis focused on the uplift behaviour of caissons constructed in sands. Novel experimental testing offered valuable insights on the injection of grout into a bentonite-filled annulus and the frictional resistance of caissons subjected to uplift. Numerical modelling provided an enhanced basis for the design of under-reamed caissons. The results of all four results chapters were subsequently utilised to develop practical design methods and recommendations for improved construction practices. Finally, potential reductions in EC enabled by the results were highlighted. This chapter summarises the key contributions of this research and proposes directions for future work.

8.2 Key Contributions

In this section, the contributions of this thesis are outlined in the context of the four research problems described in the *Problem Statement* in the Section 1.3.

8.2.1 Problem 1: Limited Literature on the EC of MT

a) A methodology to analyse the EC of MT was developed. The proposed methodology was applied to three exemplar UK case histories to explore the influence of construction stages/processes and high-level design decisions. Total emissions across all three projects totalled 1,005 tCO_2e. The contributions of both tunnels and shafts to the overall emissions were substantial. Production of materials and components (Modules A1-A3) was shown to account for 68.5% of EC across the three projects, with the majority of these emissions coming from concrete production. Steel reinforcement and fabricated steel components made up a smaller, but still significant contribution to A1-A3 EC (Chapter 3).

b) Sensitivity analysis demonstrated that the EC of the present case studies was significantly reduced by using reinforcing steel produced in an electric arc furnace (in comparison to a hypothetical scenario where basic oxygen furnace produced steel was used instead). In contrast, the steel plate components of the present case studies were produced using basic oxygen furnace steel. Using lower-EC steel plate could have reduced EC by a further 8.1%. The results of this analysis underline the importance of shifting reliance away from basic oxygen furnace steel production globally. Given the dominance of A1-A3 emissions, particularly from concrete, the importance of reduced material usage was highlighted. This can be achieved through improved design methods for jacking pipes and tunnelling shafts. In the longer term, innovative material production methods will be essential if the construction industry is to achieve net-zero (Section 7.7.3).

c) Site activities (Module A5) accounted for 20.5% of total emissions across the three projects. Ground conditions had a significant influence on A5 EC for the tunnels. Shorter tunnels were shown to have much higher emissions per metre tunnelled, due to the greater influence of the fixed EC cost of mobilising and demobilising tunnelling operations (Section 3.7.3).

d) Normalising the present results by the internal volume of pipeline constructed and comparing them to the literature suggested that MT produces less EC than OCI, the main alternative pipeline construction method (Section 7.7.1).

e) Using the design history of one of the case studies as an exemplar, it was quantified how minimising the number of intermediate shafts through good high-level design decision making can significantly reduce EC (Section 7.7.2).

8.2.2 Problem 2: No Design Methods for Caisson Skin Friction Resisting Uplift

a) Novel experimental testing was conducted using an apparatus designed to simulate: (i) caisson sinking, (ii) grout injection, and (iii) the resulting friction during uplift. Four experimental tests demonstrated that grout injection after sinking effectively re-engages friction (Chapter 4). A key advantage of the testing methodology was the unrestricted self-determination of the shear plane, unlike conventional direct shear apparatus.

b) The first factor considered in testing was the bentonite age's influence on grout injection. Older, more viscous bentonite led to less effective grout spread. Experimental observations indicated that controlling injection at each port independently can help ensure effective grout spread. Despite variation in grout spread, consistent failure mechanisms and friction suggest high confidence in skin friction development, even without perfect grout coverage (Section 4.5).

c) The second factor investigated was the time between grout injection and uplift onset. This duration had little impact on skin friction, as the same failure mechanism occurred regardless of grout age. This suggests that the caisson base can be poured soon after grouting without concerns about reduced friction, and the grout's strength and therefore cement content can be decreased (Section 4.5).

d) Bentonite lubrication formed an internal and external filter cake, enabling the observed failure mechanism where the caisson wall, grout, remaining lubricant, and filter cake move together, resulting in the shear failure plane occurring in the sand (Section 4.5.4).

e) Friction measurements were used to derive 'lower bound' and 'best estimate' interface roughness factors. The best estimate factor was $\alpha \approx 1$, although this could not be fully verified. The lower bound, $\alpha = 0.48$, provides an operational friction value that can be confidently applied in practice (Section 7.5.1).

f) Comparisons to previous studies on bored pile construction suggested: (i) conventional shear boxes may have forced the shear plane to occur within the external filter cake; (ii) using polymer fluids instead of bentonite could increase friction; and (iii) particle size distribution significantly influences filter cake formation, the resulting failure mechanism, and friction development. Consequently, the application of results in this thesis should be constrained to coarse-grained sands (Section 7.5.2). In particular, it is suspected the same failure mechanism may not occur in finer grained soils, leading to different friction values.

g) The use of bored pile literature in caisson uplift design may be appropriate, provided that comparable soil conditions are ensured and the limitations outlined in Section 7.5.3 are considered.

h) A realistic caisson case study demonstrated that the uplift friction measured in this thesis can provide significant resistance in practice, thereby reducing carbon emissions by decreasing reliance on caisson self-weight (Section 7.7.4).

8.2.3 Problem 3: Uncertainty Surrounding the Grout Injection Process

a) Observations during the uplift testing (Chapter 4) confirmed fears that VF may result in poor grout coverage. Therefore, a novel apparatus was developed to enable the observation of cementitious grout injection into a bentonite-filled annulus during caisson construction. Five tests were undertaken to explore the influence of bentonite viscosity and bentonite thixotropy on the grout injection process and the likelihood of encountering VF issues. The spread of grout was tracked using image processing techniques (Chapter 5).

b) Observations demonstrated a strong correlation between increased bentonite viscosity and reduced grout coverage. Increased bentonite viscosity particularly limited the lateral spread of the grout (Section 5.6.1).

c) The impact of thixotropy was less pronounced, mainly manifesting in localised instabilities and irregular grout profiles. Ellipticity of the grout profile was demonstrated to be an effective metric for quantifying the uniformity of grout spread. These results, combined with the qualitative observations, suggest the influence of thixotropy is transient and only serves to make the grout profile more irregularly shaped, with limited impact on the final grouted area (Section 5.6.2).

d) A theoretical model was developed to predict the stability of grout injection, and hence the likelihood of uniform grout spread. The developed model is a function of grout flow rate, the grout injection port radius, and the annulus width. These input parameters, along with the relative viscosity of the bentonite and grout, are used to calculate a 'stability parameter' S. The experimental results were used to validate the model, demonstrating its ability to effectively capture observed behaviour. A stability criterion ($S < 18$ kN/m^3) is proposed to ensure a 'good' spread of grout in practice (Section 7.2).

e) Comparisons were made between the grout injection behaviour observed in the uplift testing (Chapter 4) and the primary grout injection results (Chapter 5). These comparisons

highlighted the substantial influence of bentonite viscosity and grout injection port radius on injection stability. The risk of bentonite consolidation and filtration causing viscosity increases in practice is a critical concern (Section 7.3).

f) The derived model was used to explore potential on-site remedial measures, including minimising the injection flow rate, increasing grout viscosity, and optimising the injection system (Section 7.4).

8.2.4 Problem 4: No Design Method for Under-Reamed Caissons in Sands

a) The uplift resistance of under-reamed caissons in sand was investigated using FEA in PLAXIS 2D (Chapter 6). A novel workaround was employed to implement fully automated AR using Python and the PLAXIS Remote Scripting Interface (Section 6.3.3). The modelling approach was validated by comparing predictions to conventional plate anchors using an EP model with Mohr-Coulomb failure criterion and associated flow (Section 6.4).

b) The first part of the numerical study assessed the suitability of ULS analyses for use in practice. EP analyses employing non-associated flow revealed that the associated flow assumption may overestimate uplift capacity. To consider the influence of additional soil behaviours, such as realistic stiffnesses and stress-state dependency, large-deformation analyses using a HP material model were conducted. The results suggest that ULS analyses may be reliable in dense sands at shallow depths. However, in loose sands and at greater depths, the predicted displacements at failure were impractically large for design applications. Most realistic depths are sufficient to render ULS analyses ineffective (Section 6.5).

c) The remainder of the study focused on small deformation SLS analyses, using the HP model with a fixed displacement of 10 mm. The SLS study investigated the influence of depth (H/b, where H is depth and b is the anchor width), anchor taper angle (β), anchor roughness (α), and initial soil relative density (I_{d0}) on normalised uplift resistance (N_g) for two sands (Section 6.6).

d) The results demonstrated depth had limited influence on N_g under SLS conditions, indicating that SLS uplift resistance has an approximately linear relationship with depth

(Section 6.6).

e) Increasing β led to significant decreases in N_g for low α, whilst more modest decreases were observed for high α. The results suggest that β should be minimised in design to: (i) maximise N_g; and (ii) minimise the influence of α (Section 6.6.3).

f) The influence of β and α on $N_g/N_{g,\beta=0}$ was shown to be independent of soil type, H/b, and I_{d0}. Using these independencies, a design chart presenting $N_g/N_{g,\beta=0}$ as a function of β and α was developed to expedite preliminary design in practice (Section 7.6).

g) The practical implications of the findings were explored through a realistic design case, demonstrating that under-reaming can significantly enhance uplift resistance, thereby enabling reduced caisson weight and material usage (Section 7.7.4).

8.3 Recommendations for Future Research

8.3.1 Embodied Carbon Analysis

a) Expanding the MT EC database by incorporating additional case studies could facilitate the development of tools for estimating EC based on high-level design information. This expansion would also provide further insights into the influence of factors such as ground conditions and high-level design decisions.

b) Conducting comprehensive EC analysis of further open-cut pipeline installations would enhance the comparisons made in Section 7.7.1.

c) Undertaking a detailed EC analysis of large-diameter open caisson projects would enhance the contextualisation of the emission reductions achieved through the improved caisson design and construction methods presented in this thesis. Such an analysis could also identify additional opportunities for improvement.

d) Data acquisition and curation for the EC analysis in this thesis were conducted manually. Employing more advanced techniques, such as automated data 'scraping' and intelligent handling of fragmented records, could enable the efficient collection and processing of large datasets.

8.3.2 Structural Design

a) Whilst this thesis made substantial contributions to geotechnical understanding and high-level design decisions, structural design aspects received limited attention. For instance, the RC pipes used in the MT projects exhibited high EC due to their high cement content and the significant quantities of reinforcing steel (Section 3.4). These structural design decisions are often driven by on-site risks, such as pipe collisions with boulders or hard strata, which can lead to pipe failure. Addressing these risks through collaboration with MT contractors and focused research could enable the adoption of lower-EC RC pipes or alternative materials, such as polymer-based pipes.

b) Excess concrete use in caisson sinking is primarily driven by geotechnical requirements, particularly the need for sufficient weight during both sinking and uplift. Exploring alternative approaches to achieve this weight using materials with lower EC could result in significant overall EC reductions. For example, employing varying grades of concrete strength within the same structure, similar to the approach demonstrated for RC beams by Mak & Lees (2023), may prove beneficial. In the context of caissons, this could involve using high-strength concrete near the cutting shoe, where structural demands are greatest, and lower-strength concrete higher up the walls, where only compressive hoop stresses are present (Royston et al., 2022b). Alternatively, incorporating voids filled with rock ballast within the RC walls could maintain the required weight whilst reducing the overall volume of concrete. The inclusion of voids to minimise material use is already well-established in other areas of RC structural design, such as voided biaxial slabs (e.g. Ismael Adil et al., 2019). Further research may be required to adapt and apply both these methods to caisson construction effectively.

8.3.3 Caisson Uplift Friction

a) The experimental testing on uplift friction (Chapter 4) was performed in densely packed, coarse sand. Comparisons with bored pile literature (Section 7.5.2) suggested that the results and the proposed design method may have limited applicability in other soil conditions. Consequently, investigating a broader range of soil conditions represents a crucial area for future research and could facilitate the development of a more generalised design

approach.

b) The dry conditions employed in testing tacitly modelled the behaviour of caissons constructed with effective dewatering (see Figure 2.2). In practice, scenarios may arise where saturated conditions are encountered. Future experimental investigation could explore such conditions.

c) Whilst the use of low stress levels in testing was carefully considered to ensure applicability of the results in field conditions (Section 4.4), conducting tests at higher stress levels could enhance confidence in the present results.

d) Section 7.5.3 concluded that applying bored pile literature to caisson uplift friction may be appropriate, provided comparable soil conditions are ensured and the constraints discussed are carefully considered. To complement further experimental testing and expedite implementation in practice, a critical review of bored pile literature, with a specific focus on its relevance to caisson uplift friction, would be beneficial.

8.3.4 Grout Injection

a) Section 7.4 discussed potential measures to enhance grout injection on-site, including flow-rate-controlled grout injection, tailoring grout mix design to adjust viscosity, optimising the annulus width, and refining the grout injection system. Each of these measures warrants further investigation to enable confident implementation. Whether grout should be injected simultaneously through all ports (as modelled in this thesis) or independently in sequence also warrants further investigation.

b) A theoretical model was developed in Section 7.2 to predict the stability of grout injection and, consequently, the likelihood of achieving uniform grout spread. Among its required inputs, the model needs viscosity parameters for the bentonite in the annulus. To the authors' knowledge, no suitable methods currently exist for estimating the viscosity of bentonite in the annulus which has undergone consolidation and/or filtration during the sinking phase of caisson construction. This represents a significant barrier to the practical implementation of the model. Consequently, developing a unified model for predicting the

viscosity of bentonite in the annulus as a function of time would be a valuable direction for future research.

c) Non-invasive techniques, such as ground-penetrating radar, could be employed to evaluate grout coverage around the circumference of the caisson on-site. Similar approaches have been successfully applied to assess grout coverage behind tunnel lining segments (e.g. Peng et al., 2021).

8.3.5 Annulus Mechanics

a) Despite recent experimental advancements, considerable uncertainty remains regarding the successful maintenance of the annulus in high-permeability soils. Field measurements by Royston et al. (2022b) showed that the annulus collapsed in sand layers, leading to soil-structure contact. Further investigation is warranted to ensure the annulus is maintained, thereby reducing sinking friction.

b) Maintaining the annulus has significant implications for the applicability of the results presented in this thesis. If the annulus collapses, both the grout injection process and subsequent uplift friction will differ to the present results, which assume the annulus is maintained. Should future research be unable to guarantee successful maintenance of the annulus, additional investigation into grout injection and uplift friction under collapsed annulus conditions is recommended.

c) The grout injection findings in this thesis are analogous to scenarios where fresh bentonite is injected into existing, more viscous bentonite within the annulus mid-sinking. Under such conditions, VF may occur, leading to poor lubrication. This warrants further study.

d) The use of polymer fluids as an alternative to bentonite merits future research based on three factors: (i) they may provide improved annulus support in high-permeability soils; (ii) their distinct viscosity properties could enable enhanced grout injection compared to bentonite; and (iii) polymer fluids may enable increased uplift friction relative to bentonite.

8.3.6 Under-Reamed Caissons

a) The numerical analyses in this thesis provided valuable insights and supported the development of a design chart to aid preliminary design. However, the proposed design approach still requires complementary numerical analyses. Developing a prescriptive, simplified design method that eliminates the need for prior analysis would be a valuable future contribution. Such methods are particularly beneficial for the design of open caisson shafts, where decisions on construction details, such as the inclusion of an under-ream, typically rest with the contractor. A simplified design approach could accelerate industry adoption.

   The results of this thesis underscore the challenges of developing prescriptive design methods for drained conditions. Uplift resistance at acceptable displacements is largely influenced by soil compressibility, which can vary significantly across different soil conditions. Therefore, developing a more prescriptive design approach may require the development of a comprehensive dataset of uplift capacities across a wide range of soils, forming the basis of a data-driven design method. Collecting sufficient data would likely necessitate a less computationally demanding approach than the FEA employed in this thesis.

b) Validating the numerical results from this thesis, alongside those from Sheil et al. (2024) for undrained conditions, through laboratory modelling could enhance confidence in the results and the proposed design methods.

8.4 Concluding Remarks

Achieving net-zero is arguably the most pressing and significant challenge facing the world and its engineers today. The stark reality is that substantial construction is required to support fair and equitable development, yet the construction industry remains one of the largest contributors to global emissions. Research aimed at reducing EC and advancing the transition to net-zero is, therefore, more critical than ever.

This thesis contributes to that effort within the field of underground construction, with a specific focus on MT and open caisson shaft construction. The EC analysis of three MT projects provided valuable insights into the primary contributors to emissions and demonstrated how

design decisions can influence EC outcomes. The rest of the thesis concentrated on the uplift behaviour of caissons. Advancements in understanding grout injection, uplift friction, and under-reaming collectively support reductions in material use, enabling lower EC.

A Tabulated Embodied Carbon Results

Table A1. Case study 1 EC calculation results (tCO_2e).

Module	Input	T1A	T1B	T1C	LS1	RS1A	RS1B	RS1C	Total
A1	Cement	37.87	10.82	32.46	25.37	9.42	9.24	8.53	133.72
A1	Aggregates	1.22	0.35	1.05	1.86	0.69	0.68	0.63	6.47
A1	Admixture	0.63	0.18	0.54	0.54	0.20	0.20	0.18	2.47
A1	Water	0.00	0.00	0.00	0.00	0.00	0.00	0.00	0.02
A2	Transport of Constituents	1.33	0.38	1.14	1.65	0.62	0.61	0.56	6.29
A3	Production Waste	0.44	0.13	0.38	0.30	0.11	0.11	0.10	1.56
A3	Plant Operations	3.10	0.89	2.66	0.24	0.09	0.09	0.08	7.13
A1-A3	Steel Reinforcement	10.35	2.96	8.87	8.11	1.55	1.61	1.49	34.93
A1-A3	Fabricated Steel	17.19	4.91	14.73	8.98	5.83	5.83	5.83	63.30
A4	Transport to Site	16.65	4.76	14.27	1.84	0.68	0.67	0.62	39.47
A5	Site Operations	16.89	11.15	19.43	7.10	4.40	4.40	2.83	66.19
A5	Waste on Site	0.00	0.00	0.00	2.31	0.78	0.77	0.71	4.57
A5	Removal of Excavated Material	2.68	0.77	2.29	2.69	1.15	1.12	1.01	11.71
	A1-A3 Total	72.14	20.61	61.83	47.05	18.50	18.36	17.40	255.89
	A4 Total	16.65	4.76	14.27	1.84	0.68	0.67	0.62	39.47
	A5 Total	19.57	11.92	21.73	12.09	6.33	6.29	4.55	82.48
	Total	108.35	37.28	97.83	60.99	25.51	25.31	22.56	377.83

Table A2. Case study 2 EC calculation results (tCO_2e).

Module	Input	T2A	T2B	LS2	RS2A	RS2B	Total
A1	Cement	43.98	94.00	29.32	8.27	16.09	191.67
A1	Aggregates	1.42	3.03	2.15	0.61	1.18	8.38
A1	Admixture	0.73	1.56	0.63	0.18	0.34	3.44
A1	Water	0.00	0.01	0.00	0.00	0.00	0.02
A2	Transport of Constituents	1.55	3.26	1.90	0.54	1.05	8.31
A3	Production Waste	0.51	1.09	0.34	0.10	0.19	2.23
A3	Plant Operations	3.60	7.67	0.27	0.08	0.15	11.77
A1-A3	Steel Reinforcement	12.02	24.36	15.36	1.62	2.44	55.80
A1-A3	Fabricated Steel	19.96	25.38	10.20	5.83	7.40	68.77
A4	Transport to Site	19.33	40.80	2.18	0.60	1.15	64.06
A5	Site Operations	23.74	26.84	5.02	2.90	4.14	62.64
A5	Waste on Site	0.00	0.00	2.98	0.70	1.32	5.00
A5	Removal of Excavated Material	3.11	6.60	3.26	0.97	1.72	15.65
	A1-A3 Total	83.77	160.37	60.18	17.22	28.85	350.39
	A4 Total	19.33	40.80	2.18	0.60	1.15	64.06
	A5 Total	26.85	33.43	11.26	4.56	7.18	83.29
	Total	129.96	234.60	73.62	22.38	37.18	497.74

Table A3. Case study 3 EC calculation results (tCO_2e).

Module	Input	T3	LS3	RS3	Total
A1	Cement	11.48	19.37	18.49	49.35
A1	Aggregates	0.37	1.46	1.38	3.21
A1	Admixture	0.19	0.42	0.40	1.01
A1	Water	0.00	0.00	0.00	0.01
A2	Transport of Constituents	0.40	1.28	1.22	2.91
A3	Production Waste	0.13	0.23	0.22	0.58
A3	Plant Operations	0.94	0.18	0.17	1.29
A1-A3	Steel Reinforcement	2.96	1.40	1.40	5.77
A1-A3	Fabricated Steel	3.69	7.40	7.40	18.50
A4	Transport to Site	4.26	1.39	1.32	6.97
A5	Site Operations	16.51	6.28	7.85	30.64
A5	Waste on Site	0.00	1.52	1.45	2.97
A5	Removal of Excavated Material	1.00	2.97	2.79	6.76
	A1-A3 Total	20.16	31.75	30.70	82.61
	A4 Total	4.26	1.39	1.32	6.97
	A5 Total	17.51	10.77	12.09	40.37
	Total	41.94	43.91	44.10	129.95

References

Abadie, C. N., Byrne, B. W., and Houlsby, G. T. (2019). "Rigid pile response to cyclic lateral loading: laboratory tests." Géotechnique, 69(10), 863–876. https://doi.org/10.1680/jgeot.16.P.325.

Abdrabbo, F., and Gaaver, K. (2012). "Challenges and Uncertainties Relating to Open Caissons." DFI Journal, 6(1), 21–32. https://doi.org/10.1179/dfi.2012.002.

Akbarnezhad, A., and Xiao, J. (2017). "Estimation and Minimization of Embodied Carbon of Buildings: A Review." Buildings (Basel), 7(5), 1–24. https://doi.org/10.3390/buildings7010005.

Allenby, D., Waley, G., and Kilburn, D. (2009). "Examples of open caisson sinking in Scotland." Proceedings of the Institution of Civil Engineers. Geotechnical Engineering, 162(1), 59–70. https://doi.org/10.1680/geng.2009.162.1.59.

Alsadi, A. A., and Matthews, J. C. (2020). "Evaluation of Carbon Footprint of Pipeline Materials during Installation, Operation, and Disposal Phases." J. Pipeline Syst. Eng. Pract., 11(2),https://doi.org/10.1061/(asce)ps.1949-1204.0000422.

Ariaratnam, S. T., and Sihabuddin, S. S. (2009). "Comparison of emitted emissions between trenchless pipe replacement and open cut utility construction." Journal of Green Building, 4(2), 126–140. https://doi.org/10.3992/jgb.4.2.126.

Ariaratnam, S. T., Piratla, K., Cohen, A. A., and Olson, M. (2013). "Quantification of Sustainability Index for Underground Utility Infrastructure Projects." J. Constr. Eng. Manage., 139(12), A4013002. https://doi.org/10.1061/(asce)co.1943-7862.0000763.

Azaiez, J., and Singh, B. (2002). "Stability of miscible displacements of shear thinning fluids in a Hele-Shaw cell." Physics of Fluids (1994), 14(5), 1557–1571. https://doi.org/10.1063/1.1462030.

Barbary, K. (2016). "SEP: Source Extractor as a library." JOSS, 1(6), https://doi.org/10.21105/joss.00058.

Bathe, K. J. (1982). "Finite element analysis in engineering analysis." Prentice-Hall, New Jersey.

Bensimon, D., Kadanoff, L. P., Liang, S., Shraiman, B. I., and Tang, C. (1986). "Viscous flows in two dimensions." Reviews of Modern Physics, 58(4), 977–1002. https://doi.org/10.1103/RevModPhys.58.977.

Bentley Systems. (2024a). "PLAXIS Material Models Manual 2D." Software manual. Accessed 29/4/2025.https://bentleysystems.service-now.com/community?id=kb_article&sysparm_article=KB0108423

Bentley Systems. (2024b). "PLAXIS Reference Manual 2D." Software manual. Accessed 29/4/2025.https://bentleysystems.service-now.com/community?id=kb_article&sysparm_article=KB0108423

Beren, M., Çobanoglu, I., Çelik, S. B., and Ündül, Ö. 2020. "Shear Rate Effect on Strength Characteristics of Sandy Soils." Soil Mech found Eng, 57(4), 281-287. https://doi.org/10.1007/s11204-020-09667-y.

Bertin, E., and Arnouts, S. (1996). "SExtractor: Software for source extraction." Astronomy and Astrophysics Supplement Series, 117, 393–404. https://doi.org/10.1051/aas:1996164.

Bolton, M. D. (1987). "Discussion: The strength and dilatancy of sands." Géotechnique, 37(2), 219–226. https://doi.org/10.1680/geot.1987.37.2.219.

Bolton, M. D. (1986). "The strength and dilatancy of sands." Géotechnique, 36(1), 65–78. https://doi.org/10.1680/geot.1986.36.1.65.

BSI (British Standards Institute). (2011). "BS EN 15978:2011: Sustainability of construction works. Assessment of environmental performance of buildings. Calculation method." BSI, London.

BSI (British Standards Institution). (2016). "BS ISO 3310-1:2016. Test sieves. Technical requirements and testing - Test sieves of metal wire cloth." BSI, London.

Bueno, G., Hoyos, D., and Capellán-Pérez, I. (2017). "Evaluating the environmental performance of the high speed rail project in the Basque Country, Spain." Research in Transportation Economics 62: 44-56 (2017), 62 44–56. https://doi.org/10.1016/j.retrec.2017.02.004.

Byrne, B. W., and Houlsby, G. T. (2004). "Experimental Investigations of the Response of Suction Caissons to Transient Combined Loading." J.Geotech.Geoenviron.Eng., 130(3), 240–253. https://doi.org/10.1061/(ASCE)1090-0241(2004)130:3(240).

Chandler, J. A., Peraino, J., and Rowe, P. W. (1984). "Jamuna River 230 kV crossing - Bangladesh. III. Construction of foundations." Proceedings of the Institution of Civil Engineers, 76(1), 965–984. https://doi.org/10.1680/iicep.1984.1172.

Chang, B., and Kendall, A. (2011). "Life cycle greenhouse gas assessment of infrastructure construction for California's high-speed rail system." Transportation Research. Part D, Transport and Environment, 16(6), 429–434. https://doi.org/10.1016/j.trd.2011.04.004.

Chavda, J. T., and Dodagoudar, G. R. (2021). "Experimental Evaluation of Failure Zone in Sand Beneath the Ring Footing and Cutting Edge of Open Caisson Using Image Analysis." In Proc., Indian Geotechnical Conference 2019., 273–283. https://doi.org/10.1007/978-981-33-6346-5_24.

Chavda, J. T., and Dodagoudar, G. R. (2022a). "Finite element evaluation of bearing capacity factors for cutting face of open caissons." International Journal of Geotechnical Engineering, 16(8), 951–961. https://doi.org/10.1080/19386362.2022.2080962.

Chavda, J. T., and Dodagoudar, G. R. (2022b). "Experimental studies on a circular open caisson." International Journal of Physical Modelling in Geotechnics, 22(2), 70–87. https://doi.org/10.1680/jphmg.20.00050.

Chavda, J. T., Jitchaijaroen, W., Keawsawasvong, S., and Rattanadecho, P. (2023). "FELA evaluation of undrained bearing capacity of cutting edge of circular open caisson." Ships and Offshore Structures, ahead-of-print, 1–9. https://doi.org/10.1080/17445302.2023.2225952.

Chavda, J. T., Mishra, S., and Dodagoudar, G. R. (2020). "Experimental evaluation of ultimate bearing capacity of the cutting edge of an open caisson." Int J Phys Model Geo, 20(5), 281–294. https://doi.org/10.1680/jphmg.18.00052.

Chilana, L., Bhatt, A. H., Najafi, M., and Sattler, M. (2016). "Comparison of carbon footprints of steel versus concrete pipelines for water transmission." Journal of the Air & Waste Management Association, 66(5), 518–527. https://doi.org/10.1080/10962247.2016.1154487.

Chu, J., and Gan, C. L. (2004). "Effect of void ratio on K0 of loose sand." Géotechnique, 54(4), 285–288. https://doi.org/10.1680/geot.2004.54.4.285.

Chuoke, R., von Meurs, P., and von der Poel, C. (1959). "The Instability of Slow, Immiscible, Viscous Liquid-Liquid Displacements in Permeable Media." Petroleum Transactions, AIME, 216 188–194.

Conway, E. (2023). "Material world: a substantial story of our past and future." W H Allen, London.

Coussot, P. (1999). "Saffman–Taylor instability in yield-stress fluids." J.Fluid Mech., 380 363–376. https://doi.org/10.1017/S002211209800370X.

Cui, Z., Zhang, Z., Yuan, L., Zhan, Z., and Zhang, W. (2020). "Design of underground structures." Springer, Singapore.

Cuttle, C., Morrow, L. C., and Macminn, C. (2023). "Compression-driven viscous fingering in a radial Hele-Shaw cell." Phys. Rev. Fluids, 8(11), 113904. https://doi.org/10.1103/PhysRevFluids.8.113904.

D'Allesio, P., and Taylor, A. (2016). "Overcoming Inclusions within Diaphragm Walls at Cambridge Heath Shaft Whitechapel." Technical Paper - Crossrail Learning Legacy. ICE Publishing, London.

Darcy, H. (1856). "Les fontaines publiques de la ville de Dijon: exposition et application des principes à suivre et des formules à employer dans les questions de distribution d'eau." V. Dalmont, Paris.

De Wolf, C., Pomponi, F., and Moncaster, A. (2017). "Measuring embodied carbon dioxide equivalent of buildings: A review and critique of current industry practice." Energy and Buildings, 140(2017), 68–80. https://doi.org/10.1016/j.enbuild.2017.01.075.

DEFRA (Department for Environment Food & Rural Affairs). (2022). "UK Government GHG Conversion Factors for Company Reporting." Accessed 11/01/2025. https://www.gov.uk/government/publications/greenhouse-gas-reporting-conversion-factors-2022.

DEFRA (Department for Environment Food & Rural Affairs). (2021). "UK Government GHG Conversion Factors for Company Reporting." Accessed 11/01/2025. https://www.gov.uk/government/publications/greenhouse-gas-reporting-conversion-factors-2021.

DEFRA (Department for Environment Food & Rural Affairs). (2023). "Consultation on the Government's Storm Overflows Discharge Reduction Plan." Accessed 11/01/2025. https://www.gov.uk/government/publications/storm-overflows-discharge-reduction-plan.

Dimoula, V., Kehagia, F., and Tsakalidis, A. (2016). "A Holistic Approach for Estimating Carbon Emissions of Road and Rail Transport Systems." Aerosol and Air Quality Research, 16(1), 61–68. https://doi.org/10.4209/aaqr.2015.05.0313.

Faustin, N. E., Elshafie, M. Z. E. B., and Mair, R. J. (2018). "Case studies of circular shaft construction in London." Proceedings of the Institution of Civil Engineers.Geotechnical Engineering, 171(5), 391–404. https://doi.org/10.1680/jgeen.17.00166.

Fischer, G. R., Gerszewski, W. L., Barchok, F. J., and Yavarow, M. K. (2004). "Deep Caisson Sinking in Soft Soils, Grand Forks, North Dakota " In Proc., Fifth International Conference on Case Histories in Geotechnical Engineering., 185–186, New York, NY. https://doi.org/10.2307/2255336.

Gates, B. (2022)."How to avoid a climate disaster: the solutions we have and the breakthroughs we need." Penguin Books, London.

Gervasio, H., and Dimova, S. (2018). "Model for Life Cycle Assessment (LCA) of buildings. EFI Resources: Resource Efficient Construction towards Sustainable Design." Accessed 11/01/2025. https://op.europa.eu/en/publication-detail/-/publication/16cd2d1d-2216-11e8-ac73-01aa75ed71a1/language-en.

Giampa, J. R., Bradshaw, A. S., Gerkus, H., Gilbert, R. B., Gavin, K. G., and Sivakumar, V. (2019). "The effect of shape on the pull-out capacity of shallow plate anchors in sand." Géotechnique, 69(4), 355–363. https://doi.org/10.1680/jgeot.17.P.269.

Griffiths, D. V. (1982). "Computation of bearing capacity factors using finite elements." Géotechnique, 32(3), 195–202. https://doi.org/10.1680/geot.1982.32.3.195.

Hanson, C. S., Noland, R. B., and Porter, C. D. (2016). "Greenhouse gas emissions associated with materials used in commuter rail lines." International Journal of Sustainable Transportation, 10(5), 475–484. https://doi.org/10.1080/15568318.2014.985859.

Harris, D. E., and Madabhushi, G. S. P. (2015). "Uplift capacity of an under-reamed pile foundation." Proceedings of the Institution of Civil Engineers. Geotechnical Engineering, 168(6), 526–538. https://doi.org/10.1680/jgeen.14.00154.

Herle, I., and Gudehus, G. (1999). "Determination of parameters of a hypoplastic constitutive model from properties of grain assemblies." Mechanics of Cohesive-Frictional Materials, 4(5), 461–486. https://doi.org/10.1002/(SICI)1099-1484(199909)4:5.

Hill, S. (1952). "Channelling in packed columns." Chemical Engineering Science, 1(6), 247–253. https://doi.org/10.1016/0009-2509(52)87017-4.

Hojjati, A., Jefferson, I., Metje, N., and Rogers, C. D. F. (2018). "Sustainability assessment for urban underground utility infrastructure projects." Proceedings of the Institution of Civil Engineers. Engineering Sustainability, 171(2), 68–80. https://doi.org/10.1680/jensu.16.00050.

Homsy, G. M. (1987). "Viscous FIngering in Porous Media." Annual Review of Fluid Mechanics, 19 271–311. https://doi.org/10.1146/annurev.fl.19.010187.001415.

HS2 Limited. (2017). "High Speed Two Phase One information paper." Accessed 5/9/2024. https://assets.publishing.service.gov.uk/government/uploads/system/uploads/attachment_data/file/672194/C3_-_Ground_Settlement__v1.pdf.

Huang, L., Bohne, R. A., Bruland, A., Jakobsen, P. D., and Lohne, J. (2014). "Environmental impact of drill and blast tunnelling: life cycle assessment." Journal of Cleaner Production, 86 110–117. https://doi.org/10.1016/j.jclepro.2014.08.083.

Huang, L., Jakobsen, P. D., Bohne, R. A., Liu, Y., Bruland, A., and Manquehual, C. J. (2020). "The environmental impact of rock support for road tunnels: The experience of Norway." The Science of the Total Environment, 712(2020), 1–13. https://doi.org/10.1016/j.scitotenv.2019.136421.

Huang, M. Q., Chen, X. L., Ninić, J., Bai, Y., and Zhang, Q. B. (2023). "A framework for integrating embodied carbon assessment and construction feasibility in prefabricated stations." Tunnel. Underground Space Technol., 132 104920. https://doi.org/10.1016/j.tust.2022.104920.

ICE (Institution of Civil Engineers). (2022). "Low Carbon Concrete Routemap." ICE Publishing, London.

ICE (Institution of Civil Engineers). (2017). "ICE specification for piling and embedded retaining walls." ICE Publishing, London.

International Union of Railways. (2016). "Carbon Footprint of Railway Infrastructure Comparing existing methodologies on typical corridors Recommendations for harmonized approach." International Union of Railways, Paris.

Ismael Adil, A., Hejazi, F., and Rashid, R. S. M. (2019). "Voided Biaxial Slabs - State of Art." IOP Conference Series.Earth and Environmental Science, 357(1), 12004. https://doi.org/10.1088/1755-1315/357/1/012004.

ISO (International Organization for Standardization). (2017)."ISO 14688-1:2017. Geotechnical investigation and testing. Identification and classification of soil. Part 1: Identification and description." ISO, Geneva.

IStructE (The Institution of Structural Engineers). (2020). "How to Calculate Embodied Carbon." Accessed 28/02/2022. https://www.istructe.org/resources/guidance/how-to-calculate-embodied-carbon/.

Jackson, D. J., and Brander, M. (2019). "The risk of burden shifting from embodied carbon calculation tools for the infrastructure sector." Journal of Cleaner Production, 223(2019), 739–746. https://doi.org/10.1016/j.jclepro.2019.03.171.

Jangir, P., Mohan, R., and Chokshi, P. (2022). "Stability Analysis of Miscible Viscous Fingering in Bingham and Carreau Fluids." Transp Porous Med, 141(2), 561. https://doi.org/10.1007/s11242-021-01732-w.

Jones, D. C., and Hammond, P. G. (2019). "ICE (Inventory of Carbon and Energy) Database V3.0." Accessed 28/02/2022. http://www.circularecology.com/embodied-energy-and-carbon-footprint-database.html.

Kardani, M., Nazem, M., Abbo, A. J., Sheng, D., and Sloan, S. W. (2012). "Refined h-adaptive finite element procedure for large deformation geotechnical problems." Comput.Mech., 49(1), 21–33. https://doi.org/10.1007/s00466-011-0624-3.

Kaushal, V., and Najafi, M. (2020). "Comparative Assessment of Environmental Impacts from Open-Cut Pipeline Replacement and Trenchless Cured-in-Place Pipe Renewal Method for Sanitary Sewers." Infrastructures (Basel), 5(48), 1–20. https://doi.org/10.3390/infrastructures5060048.

Kaushal, V., Najafi, M. M., and Serajiantehrani, R. (2020). "Environmental Impacts of Conventional Open-Cut Pipeline Installation and Trenchless Technology Methods: State-of-the-Art Review." J. Pipeline Syst. Eng. Pract., 11(2), 03120001. https://doi.org/10.1061/(asce)ps.1949-1204.0000459.

Kelly, R. B., Houlsby, G. T., and Byrne, B. W. (2006). "A comparison of field and laboratory tests of caisson foundations in sand and clay." Géotechnique, 56(9), 617–626. https://doi.org/10.1680/geot.2006.56.9.617.

Kézdi, Á. (1974). "Handbook of soil mechanics." Elsevier Publishing Company, Amsterdam.

Khan, L. R., and Tee, K. F. (2015). "Quantification and comparison of carbon emissions for flexible underground pipelines." Canadian Journal of Civil Engineering, 42(10), 728–736. https://doi.org/10.1139/cjce-2015-0156.

Khasawneh, Y. A., Al-Omari, A. A., and Sharo, A. A. (2017). "Distress of a Large Diameter Underground Reinforced Concrete Shaft." In Proc., Congress on Technical Advancement ., 184–196, ASCE. https://doi.org/10.1061/9780784481035.017.

Khatri, and Kumar. (2011). "Effect of anchor width on pullout capacity of strip anchors in sand." Can. Geotech. J., 48(3), 511. https://doi.org/10.1139/t10-082.

Kim, M. C., and Choi, C. K. (2011). "Linear analysis on the stability of miscible dispersion of shear-thinning fluids in porous media." J.Non Newtonian Fluid Mech., 166(21), 1211–1220. https://doi.org/10.1016/j.jnnfm.2011.07.008.

Kumar, A., Khatri, V. N., and Gupta, S. K. (2021). "Numerical and analytical study on uplift capacity of under-reamed piles in sand." Mar. Georesour. Geotechnol., 40(1), 104–124. https://doi.org/10.1080/1064119X.2021.1871689.

Kyung, D., Kim, D., Yi, S., Choi, W., and Lee, W. (2017). "Estimation of greenhouse gas emissions from sewer pipeline system." Int J Life Cycle Assess, 22(12), 1901–1911. https://doi.org/10.1007/s11367-017-1288-9.

Lai, F., Liu, S., Li, Y., and Sun, Y. (2022). "A new installation technology of large diameter deeply-buried caissons: Practical application and observed performance." Tunnelling and Underground Space Technology, 125. https://doi.org/10.1016/j.tust.2022.104507.

Lam, C., Jefferis, S. A., and Martin, C. M. (2014). "Effects of polymer and bentonite support fluids on concrete-sand interface shear strength." Geotechnique, 64(1), 28–39. https://doi.org/10.1680/geot.13.P.012.

Lam, C., and Jefferis, S. A. (2017). "Polymer support fluids in civil engineering." ICE Publishing, London.

Lam, C., and Jefferis, S. A. (2016). "Performance of Bored Piles Constructed Using Polymer Fluids: Lessons from European Experience." J.Perform.Constr.Facil., 30(2), https://doi.org/10.1061/(ASCE)CF.1943-5509.0000756.

Lee, C., Zhao, B., Abouatallah, R., Wang, R., and Bazylak, A. (2019). "Compressible-Gas Invasion into Liquid-Saturated Porous Media: Application to Polymer-Electrolyte-Membrane Electrolyzers." Physical Review Applied, 11(5), https://doi.org/10.1103/PhysRevApplied.11.054029.

Lehane, B. M., Liu, Z., Bittar, E., Nadim, F., Lacasse, S., Jardine, R., Carotenuto, P., Rattley, M., Gavin, K., and Westgate, Z. (2020). "A New 'Unified' CPT-Based Axial Pile Capacity Design Method for Driven Piles in Sand." In Proc., Fourth International Symposium on Frontiers in Offshore Geotechnics., 462–477, Austin, Texas.

Li, M., Wu, Q., Song, K., De Hoop, C. F., Lee, S., Qing, Y., and Wu, Y. (2016). "Cellulose Nanocrystals and Polyanionic Cellulose as Additives in Bentonite Water-Based Drilling Fluids: Rheological Modeling and Filtration Mechanisms." Ind. Eng. Chem. Res., 55(1), https://doi.org/10.1021/acs.iecr.5b03510.

Li, Y., He, Q., Luo, X., Zhang, Y., and Dong, L. (2018). "Calculation of life-cycle greenhouse gas emissions of urban rail transit systems: A case study of Shanghai Metro." Resources, Conservation and Recycling, 128 451–457. https://doi.org/10.1016/j.resconrec.2016.03.007.

Lindner, A., Bonn, D., and Meunier, J. (2000). "Viscous fingering in a shear-thinning fluid." Physics of Fluids (1994), 12(2), 256–261. https://doi.org/10.1063/1.870303.

Lindner, A., Bonn, D., Poiré, E. C., Amar, M. B., and Meunier, J. (2002). "Viscous fingering in non-Newtonian fluids." J.Fluid Mech., 469 237–256. https://doi.org/10.1017/S0022112002001714.

Lindquist, E., and Jameson, R. (2011). "Secant Pile Shoring - Developments In Design And Construction." Deep Foundations Institute, New Jersey.

Littlechild, B., and Plumbridge, G. (1998). "Effects of construction technique on the behaviour of plain bored cast in situ piles constructed under drilling slurry." In Proc., Proceedings of the 7th international conference exhibition on piling and deep foundations, Vienna., pp. 1.6.1–1.6.8.

Liu, H., Su, F., and Li, Z. (2014). "The Criterion for Determining the Ultimate Pullout Capacity of Plate Anchors in Clay by Numerical Analysis." American Journal of Engineering and Applied Sciences, 7(4), 374. https://doi.org/10.3844/ajeassp.2014.374.386.

Loukidis, D., and Salgado, R. (2009). "Bearing capacity of strip and circular footings in sand using finite elements." Comput.Geotech., 36(5), 871–879. https://doi.org/10.1016/j.compgeo.2009.01.012.

Lu, H., Matthews, J., and Iseley, T. (2020). "How does trenchless technology make pipeline construction greener? A comprehensive carbon footprint and energy consumption analysis." Journal of Cleaner Production, 261(2020), https://doi.org/10.1016/j.jclepro.2020.121215.

Mak, M. W. T., and Lees, J. M. (2023). "Carbon reduction and strength enhancement in functionally graded reinforced concrete beams." Eng.Struct., 277 115358. https://doi.org/10.1016/j.engstruct.2022.115358.

Martin, C. M. (2011). "The use of adaptive finite-element limit analysis to reveal slip-line fields." Géotechnique Letters, 1(2), 23–29. https://doi.org/10.1680/geolett.11.00018.

Maŝín, D. (2010). "PLAXIS implementation of hypoplasticity." Plaxis bv, Delft.

Matar, M., Osman, H., Georgy, M., Abou-Zeid, A., and Elsaid, M. (2019). "Evaluating the environmental performance of pipeline construction using systems modelling." Construction Management and Economics, 38(8), 689–714. https://doi.org/10.1080/01446193.2019.1605185.

McNamara, A. M., Roberts, T. O. L., Morrison, P. R. J., and Holmes, G. (2008). "Construction of a deep shaft for Crossrail." Proceedings of the Institution of Civil Engineers Geotechnical Engineering, 161(6), 299–309. https://doi.org/10.1680/geng.2008.161.6.299.

McNamara, D., Sheil, B., Jefferis, S., Barker, C., and Nicholson, D. (2024). "An investigation of the behaviour of polymer fluids in the American petroleum institute filter press." Géotechnique, Ahead of print 1–40. https://doi.org/10.1680/jgeot.23.00209.

MEGASA (Metalurgia Galicia). (2019). "Environmental product declaration—Carbon steel reinforcing bar." Accessed 3/3/2023. https://www.megasa.com/data/WebData/Certifications/Certificados/Uk%20%20Irlanda/Seixal/Bre/Se_Bre_Epd/BREGENEPD000141.pdf.

Merifield, R. S., Lyamin, A. V., and Sloan, S. W. (2006). "Three-dimensional lower-bound solutions for the stability of plate anchors in sand." Géotechnique, 56(2), 123–132. https://doi.org10.1680/geot.2006.56.2.123

Merifield, R. S., Lyamin, A. V., and Sloan, S. W. (2005). "Stability of Inclined Strip Anchors in Purely Cohesive Soil." J Geotech Geoenviron, 131(6), 792–799. https://doi.org/10.1061/(ASCE)1090-0241(2005)131:6(792).

Merifield, R. S., Lyamin, A. V., Sloan, S. W., and Yu, H. S. (2003). "Three-Dimensional Lower Bound Solutions for Stability of Plate Anchors in Clay." J Geotech Geoenviron, 129(3), 243–253. https://doi.org/10.1061/(ASCE)1090-0241(2003)129:3(243).

Merifield, R. S., and Sloan, S. W. (2006). "The ultimate pullout capacity of anchors in frictional soils." Canadian Geotechnical Journal, 43 852–868. https://doi.org/10.1139/T06-052.

Merifield, R. S., Sloan, S. W., and Yu, H. S. (2001). "Stability of plate anchors in undrained clay." Géotechnique, 51(2), 141–153. https://doi.org/10.1680/geot.2001.51.2.141.

Milligan, G. (2000). Lubrication and soil conditioning in tunnelling, pipe jacking and microtunnelling: A state of the art review. Technical Report. Geotechnical Consulting Group, London.

Min, F., Zhu, W., and Han, X. (2013). "Filter cake formation for slurry shield tunneling in highly permeable sand." Tunnelling and Underground Space Technology, 38 423–430. https://doi.org/10.1016/j.tust.2013.07.024.

Mistri, B., and Singh, B. (2011). "Pullout behavior of plate anchors in cohesive soils." Electronic J. Geotechn. Eng., 16 1173–1184.

Miyoshi, C., and Givoni, M. (2014). "The Environmental Case for the High-Speed Train in the UK: Examining the London–Manchester Route." International Journal of Sustainable Transportation, 8(2), https://doi.org/10.1080/15568318.2011.645124.

Monfared, M. A. N. (2018). "Comparison of Trenchless Technologies and Open Cut Methods in New Residential Land Development." MSc Thesis. University of Alberta. https://doi.org/10.7939/R3HD7P754.

Morita, Y., Yamasaki, T., Kato, H., and Shibahara, N. (2011). "Life Cycle Assessment Method of Carbon Dioxide Emission from Railway Provision." Nihon LCA Gakkaishi, 7(4), 360–367. https://doi.org/10.3370/lca.7.360.

Mortazavi, M., Santamaria, A. D., Chauhan, V., Benner, J. Z., Heidari, M., and Médici, E. F. (2020). "Effect of PEM fuel cell porous media compression on in-plane transport phenomena." Journal of Power Sources Advances. https://doi.org/10.1016/j.powera.2020.100001.

MPA (Mineral Products Association). (2020). "Sustainable Development Report." Accessed 29/10/2021. https://mineralproducts.org/MPA/media/root/Publications/2021/MPA_SD_Report_2020.pdf.

MPA Precast (Mineral Product Association Precast). (2020). "Sustainability Matters 2020." Accessed 01/11/2021. https://www.britishprecast.org/Sustainability/Sustainability-Report.aspx.

National Rail. (2009). "Comparing environmental impact of conventional and high speed rail." National rail, London.

New, B. M., and Bowers, K. H. (1994). "Ground movement model validation at the Heathrow Express trial tunnel." Tunnelling '94, 301–329. https://doi.org/10.1007/978-1-4615-2646-9_19.

Newman, T. G., and Wong, H. Y. (2011). "Sinking a jacked caisson within the London Basin geological sequence for the Thames water ring main extension." Quarterly Journal of Engineering Geology and Hydrogeology, 44(2), 221–232. https://doi.org/10.1144/1470-9236/09-055.

Ng, C. W. W., and Lei, G. H. (2003). Performance of long rectangular barrettes in granitic saprolites. J Geotech Geoenviron, 129(8), 685–696. https://doi.org/10.1061/(ASCE)1090-0241(2003)129:8(685)

NIC (National Infrastructure Commission). (2017). "Congestion, capacity, carbon: Priorities for national infrastructure. Consultation on a national infrastructure assessment." Accessed 28/02/2022. https://nic.org.uk/studies-reports/national-infrastructure-assessment/national-infrastructure-assessment-1/congestion-capacity-carbon-priorities-for-national-infrastructure.

Nonveiller, E. (1987). "Open Caissons for Deep Foundations." Journal of Geotechnical Engineering, 113(5), 424–439. https://doi.org/10.1061/(asce)0733-9410(1987)113:5(424).

Northcutt, S. and Wijewickreme, D. (2013). Effect of particle fabric on the coefficient of lateral earth pressure observed during one-dimensional compression of sand. Canadian Geotechnical Journal, 50(5), 457–466. https://doi.org/10.1139/cgj-2012-0162.

Olugbenga, O., Kalyviotis, N., and Saxe, S. (2019). "Embodied emissions in rail infrastructure: a critical literature review." ERL, 14(12), https://doi.org/10.1088/1748-9326/ab442f.

Paris, R., and de Silva, M. (2010). "Crossrail Carbon Footprint study — Methodology and Results." London, UK, 1–53.

Pau, G. S. H., Bell, J. B., Pruess, K., Almgren, A. S., Lijewski, M. J., and Zhang, K. (2010). "High-resolution simulation and characterization of density-driven flow in CO2 storage in saline aquifers." Adv.Water Resour., 33(4), 443–455. https://doi.org/10.1016/j.advwatres.2010.01.009.

Peng, M., Wang, D., Liu, L., Shi, Z., Shen, J., and Ma, F. (2021). "Recent Advances in the GPR Detection of Grouting Defects behind Shield Tunnel Segments." Remote Sensing (Basel, Switzerland), 13(22), 4596. https://doi.org/10.3390/rs13224596.

Phillips., B. M. (2023). "Stoppage induced friction variation in pipe jacking." DPhil Thesis. University of Oxford.

Pinilla, A., Asuaje, M., and Ratkovich, N. (2021). "Experimental and computational advances on the study of Viscous Fingering: An umbrella review." Heliyon, 7(7). https://doi.org/10.1016/j.heliyon.2021.e07614.

Piratla, K. R., Ariaratnam, S. T., and Cohen, A. (2012). "Estimation of CO2 Emissions from the Life Cycle of a Potable Water Pipeline Project." J. Manage. Eng., 28(1), 22–30. https://doi.org/10.1061/(asce)me.1943-5479.0000069.

Praetorius, S., and Schößer, B. (2017). "Bentonite Handbook - Lubrication for Pipe Jacking." Ernst and Sohn, Berlin.

Puller, M. (2003). "Deep excavations: a practical manual." 2nd edition. Thomas Telford, London.

Rahman, M. A., and Sengupta, S. (2017). "Uplift Capacity of Inclined Underreamed Piles Subjected to Vertical Load." J.Inst.Eng.India Ser.A, 98(4), 533–544. https://doi.org/10.1007/s40030-017-0240-0.

Rehan R., and Knight, D. M. (2007). "Do Trenchless Pipeline Construction Methods Reduce Greenhouse Gas Emissions. Preliminary Rep." Accessed 29/03/2022. https://www.academia.edu/9233679/PRELIMINARY_REPORT_Do_Trenchless_Pipeline_Construction_Methods_Reduce_Greenhouse_Gas_Emissions.

Ren, J., Deshun, Y., and Zhai, R. (2021). "Rheological behavior of bentonite-water suspension at various temperatures: Effect of solution salinity." Eng.Geol., 295. https://doi.org/10.1016/j.enggeo.2021.106435.

Richards, I. A., Bransby, M. F., Byrne, B. W., Gaudin, C., and Houlsby, G. T. (2021). "Effect of Stress Level on Response of Model Monopile to Cyclic Lateral Loading in Sand." J.Geotech.Geoenviron.Eng., 147(3), https://doi.org/10.1061/(ASCE)GT.1943-5606.0002447.

Rodriguez, R., and Perez, F. (2021). "Carbon foot print evaluation in tunneling construction using conventional methods." Tunnelling and Underground Space Technology, 108. https://doi.org/10.1016/j.tust.2020.103704.

Roy, A., Chow, S. H., O'Loughlin, C. D., and Randolph, M. F. (2021). "Towards a simple and reliable method for calculating uplift capacity of plate anchors in sand." Can Geotech J, 58(9), 1314–1333. https://doi.org/10.1139/cgj-2020-0280.

Roy, A., O'loughlin, C. D., CHOW, S. H., and Randolph, M. F. (2022). "Inclined loading of horizontal plate anchors in sand." Géotechnique, 72(12), 1051–1067. https://doi.org/10.1680/jgeot.20.P.119.

Royston. R. (2018). "Investigation of Soil-Structure Interaction for Large Diameter Caissons." DPhil Thesis. University of Oxford.

Royston, R., Sheil, B. B., and Byrne, B. W. (2022a). "Undrained bearing capacity of the cutting face for an open caisson." Géotechnique, 72(7), 632–641. https://doi.org/10.1680/jgeot.20.P.210.

Royston, R., Sheil, B., and Byrne, B. (2022b). "Monitoring the construction of a large-diameter caisson in sand." Proceedings of the Institution of Civil Engineers. Geotechnical Engineering, 173(3), 323–339. https://doi.org/10.1680/jgeen.19.00266.

Saffman, P. G. (1986). "Viscous fingering in Hele-Shaw cells." J. Fluid Mech., 173 73–94. https://doi.org/10.1017/s0022112086001088.

Saffman, P. G., and Taylor, G. I. (1958). "The penetration of a fluid into a porous medium or Hele-Shaw cell containing a more viscous liquid." Proc.R.Soc.Lond.A, 245(1242), 312–329. https://doi.org/10.1098/rspa.1958.0085.

Safiullah, A. M. M. (2005). "Geotechnical problems of bridge construction in Bangladesh " Japan-Bangladesh Joint Seminar on Advances in Bridge Engineering, 135–146.

Saxe, S., Miller, E., and Guthrie, P. (2017). "The net greenhouse gas impact of the Sheppard Subway Line." Transportation Research. Part D, Transport and Environment, 51 261–275. https://doi.org/10.1016/j.trd.2017.01.007.

Sheil, B. B., Templeman, J. O., Orazalin, Z., Phillips, B. M., and Song, G. (2024). "Undrained uplift resistance of under-reamed open caisson shafts." Géotechnique, 74(10), 959–973. https://doi.org/10.1680/jgeot.21.00090.

Sheil, B., and Templeman, J. (2023). "Bearing capacity of open caissons embedded in sand." Geotechnique, 73(6), 495–505. https://doi.org/10.1680/jgeot.21.00089.

Shewchuk, J. R. (2002). "Delaunay refinement algorithms for triangular mesh generation." Computational Geometry : Theory and Applications, 22(1), 21–74. https://doi.org/10.1016/S0925-7721(01)00047-5.

Shewchuk, J. R. (1996). "Triangle: Engineering a 2D quality mesh generator and Delaunay triangulator." In Proc., First ACM Workshop on Applied Computational Geometry, WACG '96., 203–222, Philadelphia, PA, USA. https://doi.org/10.1007/BFb0014497.

Shokri, H., Kayhani, M. H., and Norouzi, M. (2017). "Nonlinear simulation and linear stability analysis of viscous fingering instability of viscoelastic liquids." Physics of Fluids, 29https://doi.org/10.1063/1.4977443]1070-6631/2017/29.

Sisko, A. W. (1958). "The Flow of Lubricating Greases." Industrial and Engineering Chemistry, 50(12), 1789–1792. https://doi.org/10.1021/ie50588a042.

Song, G., and Sheil, B. B. (2023). "Laboratory Testing of Construction-Induced Ground Displacements for Open Caisson Shafts in Sand." J.Geotech.Geoenviron.Eng., 149(10), https://doi.org/10.1061/JGGEFK.GTENG-11419.

Song, Z., Hu, Y., and Randolph, M. F. (2008). "Numerical Simulation of Vertical Pullout of Plate Anchors in Clay." J.Geotech.Geoenviron.Eng., 134(6), 866–875. https://doi.org/10.1061/(ASCE)1090-0241(2008)134:6(866).

Sterling, R., Admiraal, H., Bobylev, N., Parker, H., Godard, J., Vähäaho, I., Rogers, C. D. F., Shi, X., and Hanamura, T. (2012). "Sustainability issues for underground space in urban areas." Proceedings of the Institution of Civil Engineers. Urban Design and Planning, 165(4), 241–254. https://doi.org/10.1680/udap.10.00020.

Tanveer, S. (2000). "Surprises in viscous fingering." J.Fluid Mech., 409 273–308. https://doi.org/10.1017/S0022112099007788.

Tasan, H. E., and Yilmaz, S. A. (2019). "Effects of installation on the cyclic axial behaviour of suction buckets in sandy soils." Appl.Ocean Res., 91. https://doi.org/10.1016/j.apor.2019.101905.

Templeman, J. O. (2022). "Novel measurement and modelling of soil-structure interaction for open caisson shafts." DPhil Thesis. University of Oxford.

Templeman, J. O., Phillips, B. M., and Sheil, B. B. (2023). "Cutting shoe design for open caissons in sand: influence on vertical bearing capacity." Proceedings of the Institution of Civil Engineers Geotechnical Engineering, 176(1), 58–73. https://doi.org/10.1680/jgeen.20.00218.

Ter-Galustov, S., Ponomarenko, A. I., Opershtein, V. L., and Ivanov, V. D. (1966). "Experience in sinking an open caisson in a thixotropic lining." Soil Mechanics and Foundation Engineering, 3(2), 128–131. https://doi.org/10.1007/BF01703486.

Terzaghi, K., and Peck, R. B. (1967). "Soil mechanics in engineering practice." 2nd Edition. Wiley, New York.

Thasnanipan, N., Baskaran, G., and Anwar, M. A. (1998). "Effect of construction time and bentonite viscosity on shaft capacity of bored piles." In Proc., Deep foundations on bored and auger piles: Proceedings of the 3rd international geotechnical seminar on bored and auger piles, Ghent, Belgium., 171–177, Rotterdam, The Netherlands: Balkema.

Tomlinson, M. J. (2001). "Foundation Design and Construction." 7th edition. Prentice Hall, New York.

United Nations. (2018). "UN World Urbanization Prospects." Accessed 24/02/2022. https://population.un.org/wup/Download/.

Van Langen, H., and Vermeer, P. A. (1991). "Interface elements for singular plasticity points." Int.J.Numer.Anal.Methods Geomech., 15(5), 301–315. https://doi.org/10.1002/nag.1610150502.

Verst, R., Blumenthal, A., Du, J., Konig, D., Pulsfort, M., and Wichtmann, T. (2022). "Systematic laboratory and field study on the shear resistance of the soil-concrete interface of diaphragm walls and bored piles ." In Proc., DFI-EFFC International Conference on Deep Foundations and Ground Improvement: Smart Construction for the Future., 156–167, Berlin.

Von Wolffersdorff, P. (1996). "A hypoplastic relation for granular materials with a predefined limit state surface." Mechanics of Cohesive-Frictional Materials, 1(3), 251–271. https://doi.org/10.1002/(SICI)1099-1484(199607)1:3.

Wang, D., Hu, Y., and Randolph, M. F. (2010). "Three-Dimensional Large Deformation Finite-Element Analysis of Plate Anchors in Uniform Clay." J Geotech Geoenviron, 136(2), 355–365. https://doi.org/10.1061/(ASCE)GT.1943-5606.0000210.

Wang, Y., Zhang, C., Wei, N., Oostrom, M., Wietsma, T. W., Li, X., and Bonneville, A. (2013). "Experimental Study of Crossover from Capillary to Viscous Fingering for Supercritical CO2–Water Displacement in a Homogeneous Pore Network." Environ.Sci.Technol., 47(1), 212–218. https://doi.org/10.1021/es3014503.

Watari, T., Giurco, D., and Cullen, J. (2023). "Scrap endowment and inequalities in global steel decarbonization." J.Clean.Prod., 425. https://doi.org/10.1016/j.jclepro.2023.139041.

Westin, J., and Kågeson, P. (2012). "Can high speed rail offset its embedded emissions?" Transportation Research. Part D, Transport and Environment, 17(1), 1–7. https://doi.org/10.1016/j.trd.2011.09.006.

White, D. J., and Lehane, B. M. (2004). "Friction fatigue on displacement piles in sand." Géotechnique, 54(10), 645–658. https://doi.org/10.1680/geot.2004.54.10.645.

Wichtmann, T., Fuentes, W., and Triantafyllidis, T. (2019). "Inspection of three sophisticated constitutive models based on monotonic and cyclic tests on fine sand: Hypoplasticity vs. Sanisand vs. ISA." Soil Dynamics and Earthquake Engineering, 124, 172–183. https://doi.org/10.1016/j.soildyn.2019.05.001.

Willis, L., Royston, R., and Phillips, D. (2023). "The role of instrumentation in the construction of a large diameter underwater caisson." In Proc., Underground Construction Prague 2023., Prague.

World GBC (Green Building Council). (2019). "Bringing embodied carbon upfront - Coordinated action for the building and construction sector to tackle embodied carbon." Accessed 24/02/2022. https://www.worldgbc.org/sites/default/files/WorldGBC_Bringing_Embodied_Carbon_Upfront.pdf.

Xu, J., Guo, C., Chen, X., Zhang, Z., Yang, L., Wang, M., and Yang, K. (2019). "Emission transition of greenhouse gases with the surrounding rock weakened – A case study of tunnel construction." Journal of Cleaner Production, 209(2019), 169–179. https://doi.org/10.1016/j.jclepro.2018.10.224.

Xu, T., and Bezuijen, A. (2019). "Bentonite slurry infiltration into sand: filter cake formation under various conditions." Géotechnique, 69(12), 1095–1106. https://doi.org/10.1680/jgeot.18.P.094.

Yao, Q., Yang, X., and Li, H. (2014). "Construction Technology of Open Caisson for Oversize Surge Shaft in Drift Gravel Stratum." Electronic Journal of Geotechnical Engineering, 19(2014), 5725–5738.

Yue, Y., Wang, T., Liang, S., Yang, J., Hou, P., Qu, S., Zhou, J., Jia, X., Wang, H., and Xu, M. (2015). "Life cycle assessment of High Speed Rail in China." Transportation Research. Part D, Transport and Environment, 41, 367–376. https://doi.org/10.1016/j.trd.2015.10.005.

Zhangru, S., Xiaoteng, L., Zuhao, H., and Min, Q. (2021). "Study on early warning of rapid sinking of large land caisson in silt layer." E3S Web of Conferences, 283 1036. https://doi.org/10.1051/e3sconf/202128301036.

Zienkiewicz, O. C., Taylor, R. L., and Zhu, J. Z. (2013). "The finite element method: its basis and fundamentals." 7th Edition. Butterworth-Heinemann, Amsterdam.